

# Thermally Evaporated $\text{MoO}_x$ and $\text{TaTm}$ as Hole Transport Layers for Perovskite Solar Cells

Towards fully thermally evaporated  
perovskite solar cells

Master thesis

Jasmine Apawti

# Thermally Evaporated $\text{MoO}_x$ and TaTm as Hole Transport Layers for Perovskite Solar Cells

Towards fully thermally evaporated  
perovskite solar cells

by

Jasmine Apawti

to obtain the degree of Master of Science  
at the Delft University of Technology,  
to be defended publicly on Monday September 9, 2024 at 1:30 PM.

Student number: 5150817  
Project duration: December 1, 2023 – September 9, 2024  
Thesis committee: Dr. Luana Mazzarella TU Delft (PVMD), Supervisor  
Dr. Paul Procel Moya TU Delft (PVMD), daily supervisor  
Ms. Jin Yan TU Delft (PVMD), daily supervisor  
Prof. Dr. Olindo Isabella TU Delft (PVMD)  
Dr. Ferdinand Grozema TU Delft (ChemE)

Cover: Retrieved from <https://www.phoenixsolarpanelsystems.com/solar-education/solar-basics/background-of-solar-panels/>

An electronic version of this thesis is available at <http://repository.tudelft.nl/>.

# Abstract

As global temperatures rise and energy demands increase, the need for clean, renewable energy sources is more critical than ever. Solar energy is one of the key solutions, with the majority of solar panels currently on the market being made from crystalline silicon. However, emerging photovoltaic (PV) technologies such as perovskite solar cells have already demonstrated efficiencies comparable to those of silicon solar cells, making them a promising contender to achieve even higher efficiencies.

Most of the layers in perovskite solar cells are deposited via spincoating, which is a fast and easy process but can only be done on laboratory-scale. However, deposition through thermal evaporation offers significant advantages, enabling fabrication of nanometer-thin films and facilitating large-scale fabrication needed for future industrialization of perovskite solar cell. Therefore, this research aims to develop perovskite solar cells entirely through thermal evaporation.

The reported number of hole transport materials deposited through thermal evaporation is limited. Recently, fully thermally evaporated perovskite solar cells have been created using the hole transport materials  $\text{MoO}_x$  and TaTm, and these hole transport materials will be studied in this thesis.

The  $\text{MoO}_x$  and TaTm were used as single and double hole transport layer to replace the reference layer of spincoated PTAA. It was found that the  $\text{MoO}_x$  in direct contact with the perovskite resulted in a chemical reaction, which negatively affected the energy alignment. The  $\text{MoO}_x$  also showed poor charge carrier selectivity, resulting in high interfacial recombination. Great hole extraction from the perovskite was observed for TaTm, however, a misalignment of the band energy with the electrode hindered the hole collection. Improved hole transfer was found with  $\text{MoO}_x$  and TaTm being used a double hole transport layer. Here, the TaTm functions as a passivation layer between the  $\text{MoO}_x$  and perovskite, while effectively blocking the electrons. In turn, the  $\text{MoO}_x$  improved the energy alignment from the TaTm to the electrode to improve the hole collection.

A thickness optimization of the hole transport layers was also performed. For  $\text{MoO}_x$  as single hole transport layer, it was found that number of oxygen vacancies decreased with thickness, leading to less recombination. No change was observed for TaTm as single hole transport layer when varying the thickness. However, as a double hole transport layer with  $\text{MoO}_x$ , increasing the thickness of TaTm led to an increase in  $V_{oc}$ . Ultimately, a thin layer of 2 nm  $\text{MoO}_x$  with a 5-nm thick TaTm showed the most promising results, demonstrating a final efficiency of 4.73%.

# Contents

<b>Abstract</b>	<b>i</b>
<b>Nomenclature</b>	<b>iv</b>
<b>1 Introduction</b>	<b>1</b>
1.1 Energy transition . . . . .	1
1.2 Solar energy . . . . .	3
1.3 Perovskite . . . . .	4
1.4 Architectures . . . . .	6
1.5 Hole transport layer . . . . .	7
1.6 Motivation . . . . .	8
1.7 Research objectives . . . . .	9
1.8 Report outline . . . . .	10
<b>2 Theoretical background</b>	<b>11</b>
2.1 Semiconductor physics . . . . .	11
2.1.1 Semiconductor junction . . . . .	11
2.1.2 Generation and recombination . . . . .	12
2.1.3 Semiconductor interface phenomena . . . . .	13
2.1.4 J-V curve . . . . .	16
2.2 Perovskite solar cell . . . . .	17
2.2.1 Hole transport materials . . . . .	17
2.2.2 Deposition methods . . . . .	20
2.3 PSCs with high work function HTLs . . . . .	23
2.3.1 TMOs . . . . .	23
2.3.2 Tunneling . . . . .	23
2.3.3 Band diagram . . . . .	24
<b>3 Research Methodology: Fabrication and Characterization Methods</b>	<b>26</b>
3.1 Deposition methods . . . . .	26
3.1.1 Thermal evaporation . . . . .	26
3.1.2 Spin coating . . . . .	30
3.2 Solar cell fabrication . . . . .	32
3.3 Characterization techniques . . . . .	33
3.3.1 Spectral Ellipsometry . . . . .	33
3.3.2 UV-Vis spectroscopy . . . . .	35
3.3.3 X-ray Photoelectron Spectroscopy . . . . .	37
3.3.4 Photoluminescence spectroscopy . . . . .	38
<b>4 Film level testing of MoO<sub>x</sub> and TaTm</b>	<b>41</b>
4.1 Tooling factor determination for MoO <sub>x</sub> and TaTm . . . . .	41
4.2 Thermal stability of optical and electrical properties of MoO <sub>x</sub> and TaTm . . . . .	43
<b>5 Evaluation of charge carrier extraction at the HTL interfaces</b>	<b>48</b>
5.1 Effect of hole transport material on device performance . . . . .	48

---

5.2	Hole extraction at the HTL/PVK interface for different hole transport materials . . .	51
<b>6</b>	<b>Impact of Film Thickness of MoO<sub>x</sub> and TaTm on Device Parameters</b>	<b>55</b>
6.1	Effect of layer thickness on the atomic composition of MoO <sub>x</sub> . . . . .	55
6.2	Effect of single hole transport layer thickness on the device performance . . . .	59
6.3	Effect of double hole transport layer thickness on the device performance . . . .	64
<b>7</b>	<b>Conclusion and Recommendations</b>	<b>70</b>
7.1	Conclusion . . . . .	70
7.2	Recommendations . . . . .	72
	<b>Acknowledgements</b>	<b>74</b>
	<b>References</b>	<b>75</b>
<b>A</b>	<b>Fabricated devices for thickness optimization</b>	<b>88</b>
<b>B</b>	<b>Device fabrication</b>	<b>90</b>
B.1	Z-ratio calculation . . . . .	90
B.2	Data sheet information of ITO and FTO . . . . .	90
B.3	Recipes of thermal evaporated films . . . . .	90
<b>C</b>	<b>Results of thermal stability for optical properties</b>	<b>92</b>
C.1	Absorbance . . . . .	92
C.2	Transmittance . . . . .	96
<b>D</b>	<b>TRPL</b>	<b>98</b>
<b>E</b>	<b>Device parameters for thickness optimization</b>	<b>99</b>
<b>F</b>	<b>Final device</b>	<b>102</b>

# Nomenclature

## Abbreviations

Abbreviation	Definition
CB	Conduction Band
CVD	Chemical Vapor Deposition
ETL	Electron Transport Layer
ETM	Electron Transport Material
FEP	Field-Effect Passivation
GHG	Greenhouse Gas
HI	Hysteresis Index
HOMO	Highest Occupied Molecular Orbital
HTL	Hole Transport Layer
HTM	Hole Transport Material
LUMO	Lowest Unoccupied Molecular Orbital
MoO <sub>x</sub>	Molybdenum oxide
PCE	Power Conversion Efficiency
PSC	Perovskite Solar Cell
PV	Photovoltaics
PVD	Physical Vapor Deposition
PVK	Perovskite
QCM	Quartz Crystal Monitor
SCR	Space Charge Region
SHR	Shockley-Hall-Read (recombination)
TMO	Transition Metal Oxide
VB	Valence Band

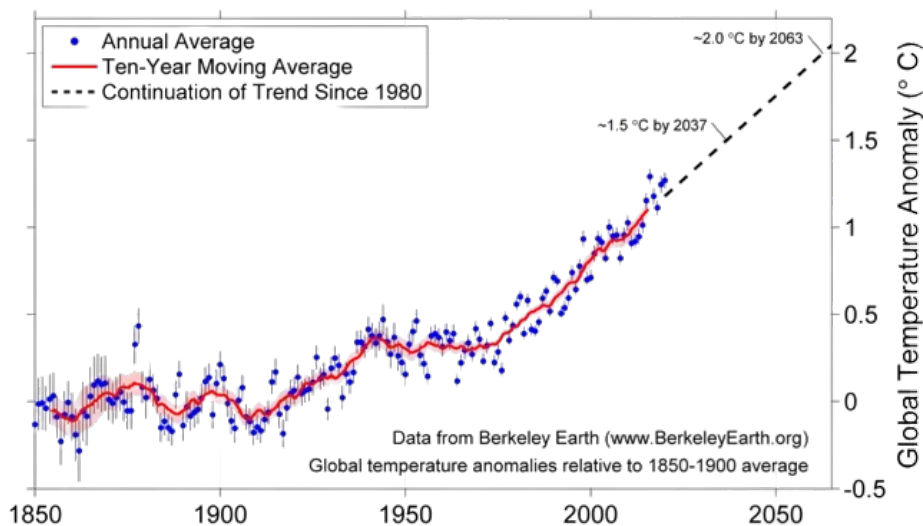
## Symbols

Symbol	Definition	Unit
$E_C$	Conduction Band Energy	[eV]
$E_F$	Fermi Energy	[eV]
$E_V$	Valence Band Energy	[eV]
$FF$	Fill Factor	[-]
$J_{sc}$	Short-circuit Current Density	[A/m <sup>2</sup> ]
$R_s$	Series Resistance	[ $\Omega$ ]
$V_{bi}$	Electrostatic potential difference or built-in potential	[V]
$V_{oc}$	Open-circuit Voltage	[V]
$WF$	Work Function	[eV]

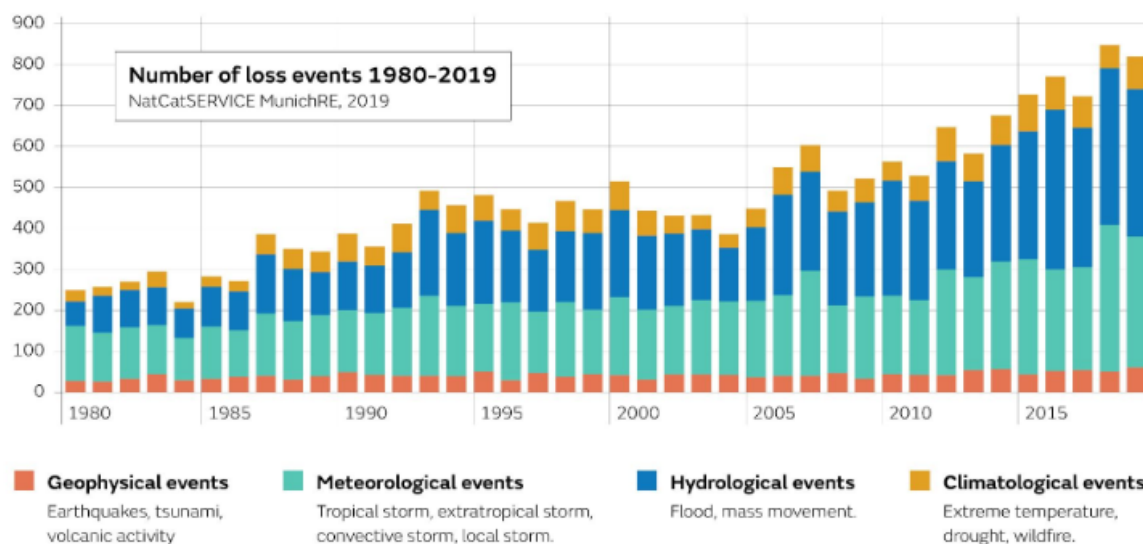
# Introduction

## 1.1. Energy transition

Global warming is defined by NASA as the long-term heating of Earth's surface since the pre-industrial period (which is between 1850 and 1900) [129]. The heating of the Earth is a direct result of the increasing levels of heat-trapping greenhouse gases (GHGs) in the Earth's atmosphere. Human activities, most specifically the burning of fossil fuels, are responsible for the release of GHGs, and have increased the average global temperature on Earth by about 1 degree Celsius since the pre-industrial period. Figure 1.1 shows that this number is predicted to increase every decade by more than 0.2 degrees Celsius with respect to the current trend [153]. Global warming causes long-term change in average weather patterns, and is expressed with certain indicators, such as increasing temperatures of land and ocean, ice loss at the poles and in mountain glaciers, rising sea levels, increasing severity and frequency of extreme weather such as floods, precipitation, hurricanes, heat waves, droughts, and wild fires. In Figure 1.2, it can be seen that the annual number of extreme weather events have more than tripled from 1980 to 2019 [124].



**Figure 1.1:** Temperature trend since the pre-industrial period in 1850 [153].

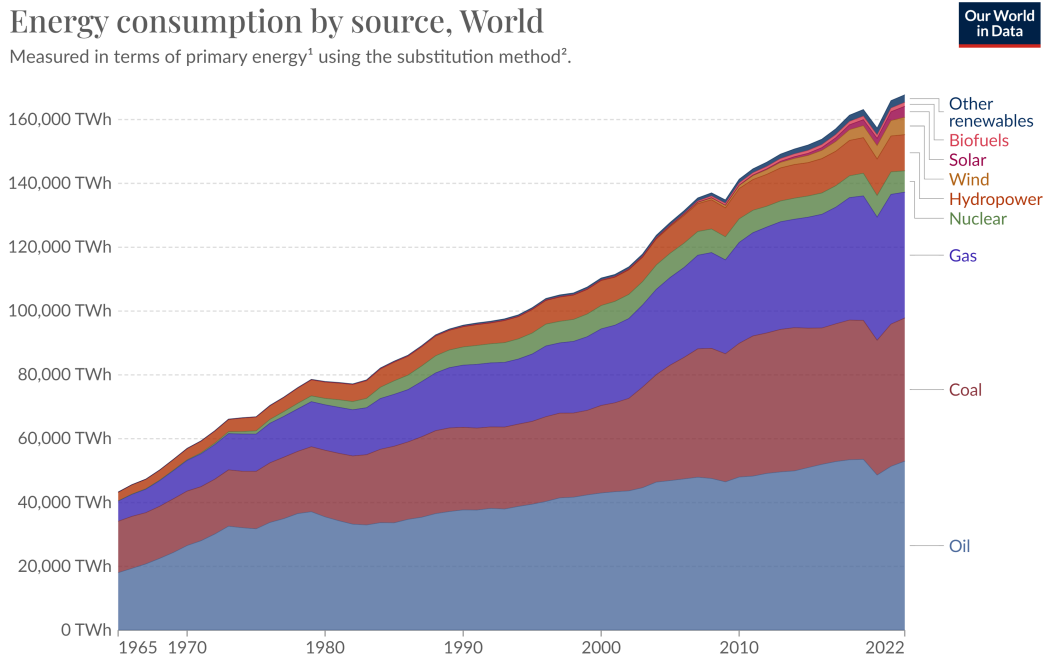


**Figure 1.2:** Annual frequency of extreme weather events from 1980 to 2019 [124].

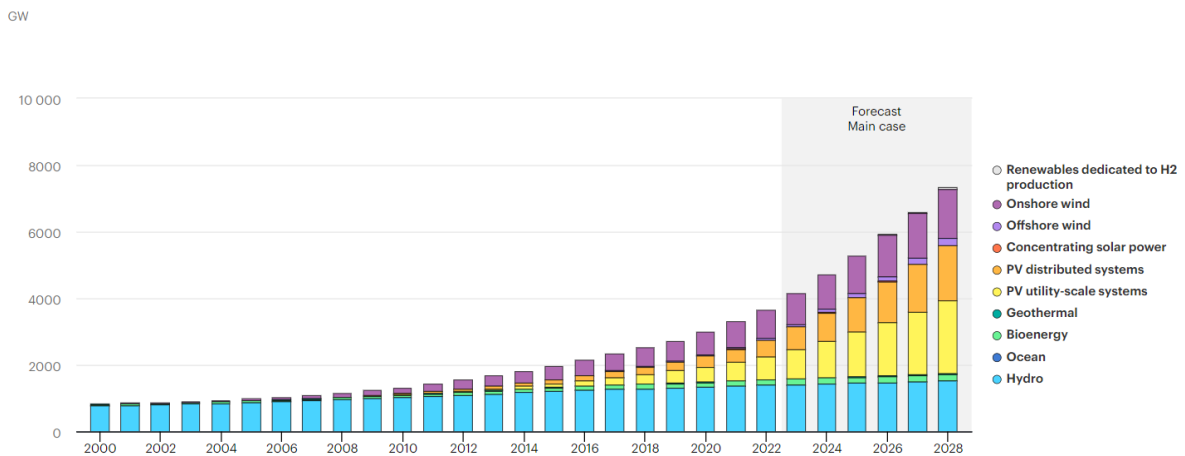
To counter the trend as shown in Figures 1.1 and 1.2, the Paris Agreement was presented in 2015. The Paris Agreement is a legally binding international treaty on climate change with the main goal to keep the increase of average global temperatures below 2 degrees Celsius compared to pre-industrial levels, with the attempt to stay below 1.5 degrees Celsius. All 196 parties that adopted the treaty, also agreed to reach net-zero emissions (carbon neutrality) by 2050 [181].

The most important strategy in reducing carbon emissions is to replace energy generated by burning fossil fuels with energy from renewable sources, such as solar, wind, hydropower and biofuels. Figure 1.3 shows the global energy consumption by source from 1965 to 2022 [137]. It can be seen that oil, coal and gas are still responsible for the vast majority of energy generation. However, energy from solar and wind have increased significantly over the last decade, and based on the forecasted installed capacity in Figure 1.4 [71], it is predicted that the solar and wind energy generation continues to grow exponentially. Currently, solar photovoltaics (PV) is the only renewable energy technology to keep up with the necessary progress to reach the net-zero emissions scenario for 2050 [72]. In this scenario, solar PV will need an installed capacity of 6044 GW and generate 8255 TWh in 2030. With the current generation of 1300 TWh in 2022, the average annual growth of the generation has to be around 26% during the period 2023-2030 [73].





**Figure 1.3:** Global energy consumption by source [137].



**Figure 1.4:** Historical data and forecast of installed capacity of renewable energy technologies [71].

## 1.2. Solar energy

Solar PV is versatile compared to the other renewable energy technologies, as its applications range from small residential roof-top systems to utility-scale power generation installations [73]. Solar PV can be installed in places where other renewable energy technologies cannot, such as densely populated cities and small areas of land, and it can be integrated into buildings, infrastructure, and vehicles. Solar cells can be categorized based on the development period and the main features of the absorber materials.

Crystalline silicon (c-Si) solar cells form the first generation of photovoltaic technology. They can be further divided into monocrystalline and polycrystalline silicon. Monocrystalline silicon has a crystal lattice that is continuous and does not contain any grain boundaries over the entire bulk. On the contrary, polycrystalline silicon is made out of many small randomly-

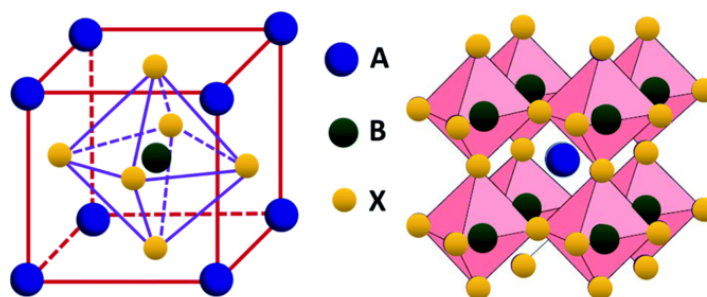
orientated crystalline grains separated by grain boundaries [169][174]. This distinction is a result of different manufacturing processes [94][174]. Crystalline silicon solar cells are the current market leader with a 95% share of global PV production in 2020, of which 84% was monocrystalline silicon [94]. Monocrystalline silicon has a world record efficiency of 26.8% [133].

The second generation consists of thin-film PV made from amorphous silicon, cadmium telluride (CdTe), and copper indium gallium selenide (CIGS) [94][44]. The absorber layers are only a few micrometers thick and therefore much thinner than c-Si solar cells. This allows for the deposition on flexible and lightweight substrates, which then can easily be applied to the innovative concept building-integrated photovoltaics (BIPV) [174][44]. However, a disadvantage of thin-film PV is the slightly lower efficiency compared to c-Si PV [169][94][174].

The third generation are emerging technologies that are still in the research and development stages. The main three groups are organic solar cells, perovskite solar cells (PSC), and dye-sensitized solar cells (DSSC) [94]. Like the second generation, these PV technologies are thin film and can also be used for light weight and flexible PV modules [174][44]. It is predicted that they are going to be more cost-effective due to cheaper manufacturing [94][174]. However, all three technologies struggle with long-term stability, which is an essential aspect for the commercialization of PV [94][174][44]. For now, the rapidly emerging perovskite solar cells, only introduced in 2009 for the first time, are the only one to reach efficiencies that are competitive with market-leading crystalline silicon PV [174]. The technology is built on the 20 years of experience with developing organic and dye-sensitized solar cells [169].

### 1.3. Perovskite

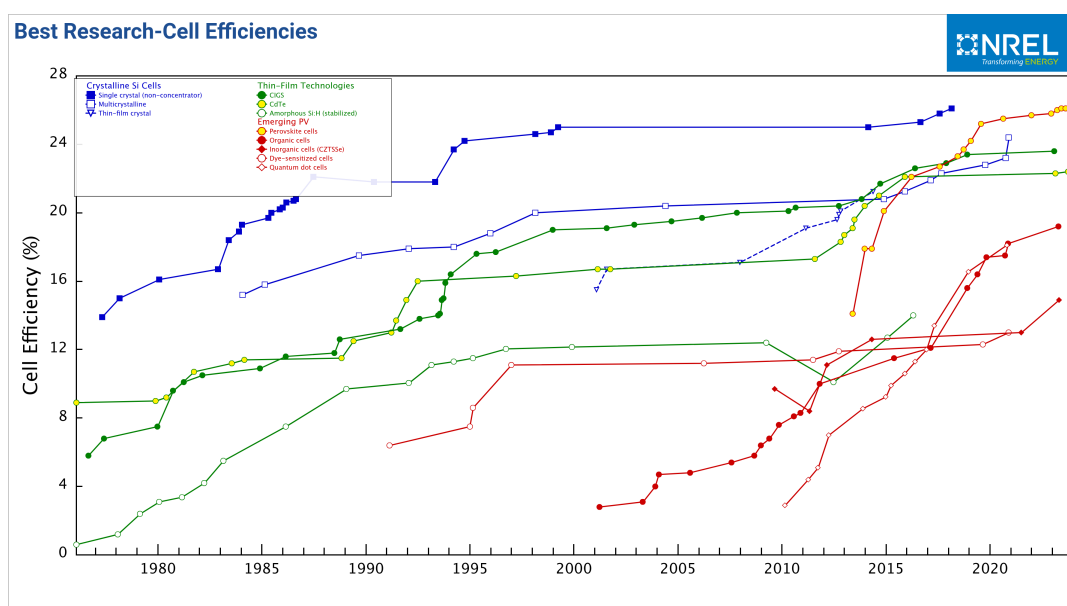
Perovskite initially referred to the oxide mineral calcium titanate ( $\text{CaTiO}_3$ ).  $\text{CaTiO}_3$  was discovered by Gustav Rose in 1839 and was named after Russian mineralogist Lev Perovski. Nowadays, “perovskite” is used for any compound with the same crystal structure of  $\text{CaTiO}_3$  [113][166]. The general formula for the perovskite structure is  $\text{ABX}_3$ , where A and B are cations and X is a halide anion [113][166][156][214][34]. The unit cell and extended network of the  $\text{ABX}_3$  are depicted in Figure 1.5 [199]. Cations A and B are of varying sizes, of which A is larger than B. The 3D structure of  $\text{ABX}_3$  changes to a low-dimensional crystalline when the A-site cation is too large. Even though these low-dimensional perovskite are more versatile because bigger molecules can be used with customized functions, they usually yield low efficiencies and are therefore rarely used in photovoltaics [156]. This is one of the reasons why of the numerous compounds with the  $\text{ABX}_3$  structure, only a limited number are suited to be used as efficient light absorber for solar cells. Suitable compounds meet various requirements such as proper light-harvesting performance, desired bandgap, alignment of energy level with adjacent materials, high mobility and long charge carrier lifetime [214]. The  $\text{ABX}_3$  structure of suitable perovskites is commonly composed as follows: A is for organic methylammonium ( $\text{MA} = \text{CH}_3\text{NH}_3$ ), formamidinium ( $\text{FA} = \text{CH}(\text{NH}_2)_2$ ), or inorganic Cs or Rb. B is most often occupied by Pb, and X is for halides I, Br, or Cl [34][101].



**Figure 1.5:**  $ABX_3$  structure of perovskite as unit cell (left) and extended network (right) [199]

Perovskites have attracted much interest for optoelectronic applications due to their high light absorption coefficient, long diffusion length and tunable bandgap [17][101]. The first perovskite solar cell (PSC) was developed in 2009 by Kojima et al. with a PCE of 3.8% using  $CH_3NH_3PbI_3$  [88]. The structure was based on dye-sensitized solar cells (DSSCs). Another experiment with similar structure by Park et al. increased the PCE to 6.5% [74]. However, the organolead halide perovskite dissolves in a polar solvent and therefore raises stability concerns when used for liquid electrolyte-based sensitized solar cells. The first long-term stable PSC was achieved in 2012 when Lee et al. designed the first solid state (non-sensitized) PSC, which demonstrated a PCE of 10.9% [97]. Since then, several PSCs have been developed and the PCE has rapidly progressed to over 26% in 2023 [133], which is comparable to the market leading mono-crystalline silicon solar cells [174]. The advancement of the PSC throughout the years is projected in figure 1.6. This expeditious increase of PSC performance has been attributed to the optimization of different factors [113][156]:

- The intrinsic materials properties, such as the band gap, the energy levels of the conduction and valence bands (or HOMO and LUMO)
- The charge transport properties
- Parameters such as layer thickness, morphology, homogeneity, surface coverage, crystalline quality, defect density, etc.

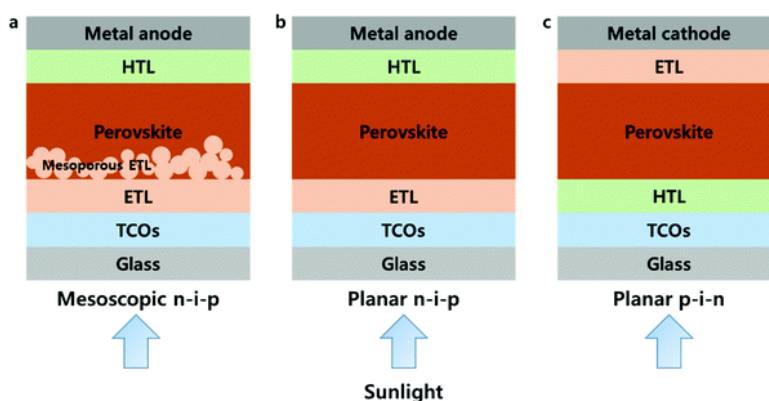


**Figure 1.6:** Power conversion efficiencies of perovskite solar cells compared to other types of solar cells [133]

## 1.4. Architectures

In general, a PSC consists of a perovskite light-absorber material sandwiched in between two electrodes. However, the perovskite/electrode interfaces allow for almost no charge transportation. Charge transportation is improved by the implementation of interfacial buffer layers such as electron transport layer (ETL) and hole transport layer (HTL) between the perovskite layer and the electrodes [156]. The first PSCs were liquid-electrolyte perovskite sensitized solar cells, where the liquid electrolyte containing both the perovskite material and mesoporous  $\text{TiO}_2$  particles functions as the new “dye” molecules [166]. However, due to severe instability these are no longer researched.

The mesoporous structure evolved from the DSSC and is depicted in Figure 1.7a) [163]. The liquid electrolyte was replaced with a solid-state hole transport layer material to avoid degradation [166]. The mesoporous structure is based on thick alumina and titania nanoparticles infiltrating the perovskite material, which allows the perovskite material to bind with the mesoporous metal oxide and increase the light-absorbing area of the active absorber layer [34]. This results in improved device performance [156]. The mesoporous configuration combines both features from thin-film solar cells and DSSCs [166]. Lee et al. were first to design a mesoporous PSC with a PCE of 10.9% in 2012 [97]. The PCE has since then improved to over 23% [156][166].



**Figure 1.7:** Different architectures of perovskite solar cells, where a) mesoporous n-i-p and b) planar n-i-p and c) planar p-i-n configuration [163].

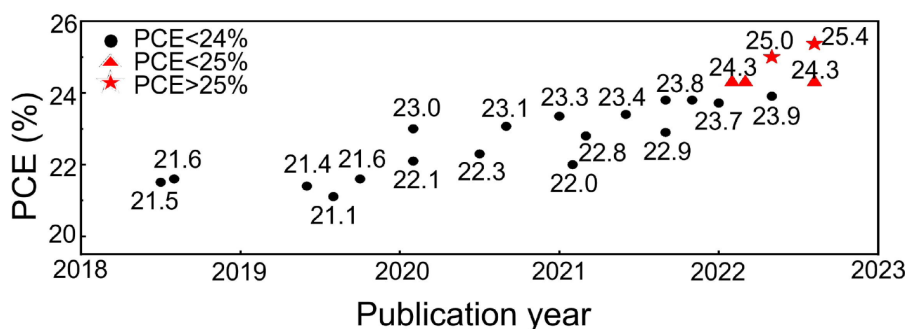
A disadvantage of the mesostructured PSC is the need for high-temperature processing methods. Low-temperature processibility of PSCs was achieved by using the planar configuration [156][166][34]. The planar heterojunction structure refers to the cell structure without mesoporous scaffold, as can be seen in Figure 1.7b and 1.7c [214][163]. The absence of the scaffold allows for an array of materials to be used as charge transport layers to go along with the perovskite. This creates significant flexibility in the preparation methods of the PSCs [156]. In the planar configuration, the perovskite layer contains the photo-generated excitons and free carriers, which are transported along this layer due to the ambipolar charge transport properties of the perovskite [113][9]. The electrons are injected to the ETL and the holes are injected to the HTL. These are the primary charge separation steps, after which the free holes and electrons are transported to their selective contacts [113][98]. Depending on the order of the functional layers in the cell, a planar PSC can be either n-i-p (Figure 1.7b) or p-i-n (Figure 1.7c). This nomenclature originates from the Si-thin-film research community and has been extended to PSC. Alternatively, those configuration with opposite polarities are called regular (n-i-p) and inverted (p-i-n) within the PVK community:

- Regular configuration (n-i-p):

In the regular planar configuration, a TCO substrate has an n-type ETM deposited on top, followed by the deposition of the perovskite absorber layer, a p-type HTM and top metal electrode [156]. Ball et al. reported the first n-i-p planar PSC in 2013 with a FTO/c-TiO<sub>2</sub>/CH<sub>3</sub>PbI<sub>3-x</sub>Cl<sub>x</sub>/spiro-OMeTAD/Au structure. However, due to difficulties in fabricating pin-hole free perovskite, a low efficiency of 1.8% was obtained [18]. The same group the optimized processing conditions and morphology of perovskite films to achieve a PCE of 11.4% a year later [45]. Currently, efficiencies above 25% are recorded for n-i-p PSCs [116].

- Inverted configuration (p-i-n): The inverted configuration has the charge transport layers deposited inverted compared to the regular configuration. The HTM is deposited on the TCO substrate, followed by perovskite absorber layer, ETM, and the top metal electrode [156][34].

The inverted structure has advantages over the regular structure due to simple device preparation, high PCE, low hysteresis, and of preceding the need of dopants in the HTL [214][9]. The challenge in fabricating inverted planar cells is to create smooth and pinhole-free perovskite films [214]. The first inverted cell is reported to have reached a PCE of 2.6% by Kumar et al. in 2013 [93]. In the same year, Liu and Kelly created an inverted PSC with a PCE of 10.2% [108]. The highest reported efficiency is currently 25% [80]. The improvement of inverted PSCs over the last few years is projected in figure 1.8 [98].



**Figure 1.8:** Power conversion efficiencies of inverted perovskite solar cells over the last few years [98].

## 1.5. Hole transport layer

The hole transport layer (HTL) and electron transport layer (ETL) are the charge transport layers in a PSC. The perovskite layer is sandwiched between the HTL and ETL (see Figure 1.7) to improve the separation and extraction of electron and holes and ultimately increase the PCE. The transportation of the electrons and holes is depicted in Figure 1.9:

Under illumination, holes in the valence band (VB) are created due to the electrons exciting to the conduction band (CB) (1). The holes diffuse to the perovskite/HTL interface (3) while the electrons diffuse to the perovskite/ETL interface (2). Then, the charge carriers move through their corresponding charge transport layer and are finally collected at the electrode [79].

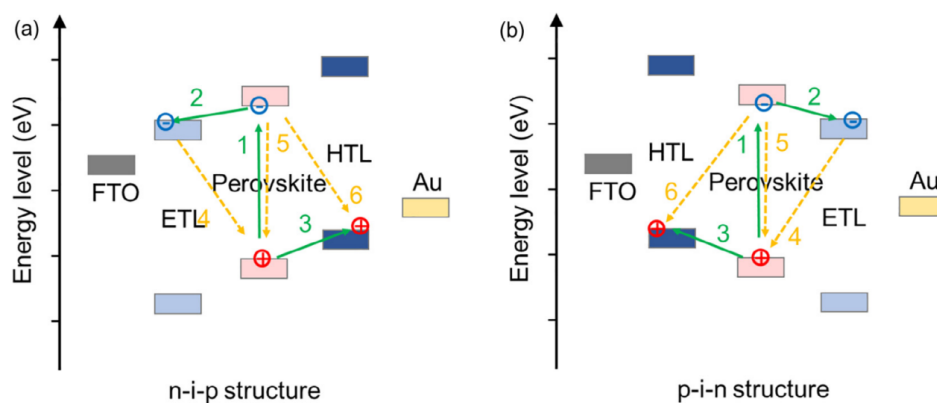
Figure 1.9 also shows the undesired recombination processes indicated by the dashed yellow arrows. This happens whenever an electron moves from the VB to a hole in the CB of the same layer or a layer it is supposed to move away from [32].

Proper selection of the charge transport layers is crucial for the performance of the PSC. An ideal charge transport material (CTM) possesses the following characteristics:

1. The highest occupied molecular orbital (HOMO) or the VB of the HTM must be slightly

higher than the HOMO of the perovskite. This helps to transport the holes at the HTL/perovskite interface into the HTL and then move quickly to the ITO (in inverted PSCs) [9][184][13][79]. Also, the electrons are effectively blocked from the ITO when there is a higher band gap between the LUMO of the HTM and the perovskite [9][79][144].

2. Proper band energy alignment to promote charge carrier transport and selectivity.
3. High charge mobility of the CTM, which provides high chances of the charge carriers created by the perovskite to reach the electrode quickly [184][32][79].
4. Good hydrophobicity and thermal stability to improve the stability of the PSC [184][32][79][144].
5. Absorption spectrum of CTM at the front and the perovskite should avoid overlap. This broadens the device's absorption spectrum range as the CTM absorbs light at different wavelength ranges from the perovskite. Consequently, the performance of the PSC improves [79].
6. Simple synthesis and easy manufacturing methods [32]
7. Transparent window in visible region for CTMs used in tandem PSCs and on the front side of PSCs to allow for high light absorption by the device [184][32].



**Figure 1.9:** The charge carrier process of n-i-p structured PSC (left) and p-i-n structured PSC (right) [32]

## 1.6. Motivation

There are various methods to prepare perovskite cells, with spin coating being one of the most popular deposition techniques. Spin coating is favored for its simplicity and speed, making it ideal for producing uniform layers at the laboratory scale. However, this method has certain drawbacks, such as difficulty in controlling film thickness, which typically is between 600-700 nm minimum [83]. Additionally, the use of hazardous solvents in spin coating can adversely affect the film surface quality [16].

In this research, thermal evaporation was employed as the deposition technique. This vacuum-based method involves the evaporation of source material to produce highly uniform films, with a controllable thickness that can be reduced to just a few nanometers. An added advantage of thermal evaporation is its suitability for both small and large areas, making it one of the highly promising deposition techniques for the future industrialization of perovskite solar cells [106].

Over recent months, the perovskite research team at TU Delft has focused on developing thermally evaporated solar cells. To date, the working devices have utilized PTAA as the hole transport layer, which is applied through spin coating. The goal of this research, however, is to create fully thermally evaporated devices.

To achieve this, the spin-coated PTAA must be replaced with a different hole transport layer.

The new layer must meet several criteria: it must be compatible with thermal evaporation deposition, have favorable band energy alignment with perovskite to facilitate hole transport while blocking electrons, and must remain stable during crystallization and perovskite formation, as it is deposited first.

Currently, there are a limited number of hole transport materials (HTMs) that have been successfully used with thermal evaporation, such as Spiro-OMeTAD [48], NPB [48], TCTA [48][177], Me-4PACz [47], Spiro-TTB [168], and NiO<sub>x</sub> [87]. One of the chosen HTMs for this research is molybdenum oxide (MoO<sub>x</sub>), an inorganic material known for its excellent thermal stability. MoO<sub>x</sub> features a large bandgap and high work function, and the PVMD group has prior experience using MoO<sub>x</sub> in crystalline silicon solar cells. In perovskite solar cells, MoO<sub>x</sub> has a low electron injection barrier, and is therefore used as an interlayer with a more selective contact. In this study, MoO<sub>x</sub> will be combined with TaTm.

TaTm, an organic material, has demonstrated suitable band energy alignment with perovskite. Although TaTm is relatively new and the studies utilizing it are limited, a research group in Valencia has successfully used the combination of MoO<sub>x</sub> and TaTm to produce high-performing cells. In this research, the same stack used by the Valencia group is adopted, with the exception of the perovskite layer. The perovskite material, Cs<sub>0.15</sub>FA<sub>0.85</sub>PbI<sub>2.85</sub>Br<sub>0.15</sub>, is developed by the perovskite group at TU Delft.

## 1.7. Research objectives

This study is based on three research objectives.

The first objective is:

- Prepare the integration of thermally evaporated MoO<sub>x</sub> and TaTm into the PSC.

To integrate the MoO<sub>x</sub> and TaTm into the PSC, the film thickness of each HTL must be controlled. In order to do so, their tooling factor must be determined. Also, MoO<sub>x</sub> and TaTm need to be able to withstand the temperatures that they will be exposed to during the annealing of the perovskite. Therefore, the thermal stability of optoelectrical properties is evaluated.

After integration of MoO<sub>x</sub> and TaTm in the PSC, the research focuses on their ability to extract charge carriers from the perovskite. The second objective is:

- Assess the charge carrier extraction of MoO<sub>x</sub> and TaTm.

The charge carrier extraction can be assessed by comparing the influence of MoO<sub>x</sub> and TaTm on the device parameters, both as single and double HTL. Furthermore, the charge carrier extraction from solely the perovskite to the HTL is investigated. In both cases, MoO<sub>x</sub> and TaTm will also be compared to reference HTL PTAA.

Lastly, a thickness optimization of the HTLs is performed. The third objective is:

- Determine the influence of the thickness of MoO<sub>x</sub> and TaTm on the device parameters.

The stoichiometry, atomic composition, and valence band energy of MoO<sub>x</sub> are evaluated for varying film thickness. Moreover, the thicknesses of the MoO<sub>x</sub> and TaTm films are varied at device level to gain an understanding of the influence of the film thickness on trends found for device parameters. The thickness optimization is performed for both single and double HTL, to investigate how presence of the additional HTL changes the trends for device parameters.

## 1.8. Report outline

This report is divided into the following chapters:

**Chapter 1** discusses the energy transition and the need for renewable energy. This is followed by the development of solar energy and an introduction to perovskite solar cells. The chapter ends by detailing the thesis project, such as the motivation of this research, as well as the research objectives and questions.

**Chapter 2** provides theoretical background on the fundamental concepts of solar cells. Here, it goes over band diagram of heterojunctions, generation and recombination mechanisms, interface phenomena, and the current-voltage curve. Moreover, a general overview of most used hole transport materials and deposition techniques for perovskite solar cells is given. The last section focuses on the electronic structure of high-work-function hole transport material in a perovskite solar cell.

**Chapter 3** describes the deposition methods and fabrication of the films used in the perovskite solar cell. Furthermore, the working principles and the settings of the characterization techniques used in this research are discussed.

**Chapter 4** illustrates the process for determining the tooling factor of  $\text{MoO}_x$  and TaTm. It also discusses the change in optical properties and estimated bandgap of  $\text{MoO}_x$  and TaTm after annealing for different annealing times and temperatures.

**Chapter 5** elaborates on the device parameters for perovskite solar cells with different hole transport layers and supports these results with the obtained charge carrier extraction of several HTL/PVK configurations.

**Chapter 6** examines the effect of thickness on the stoichiometry, atomic composition, and valence band energy of  $\text{MoO}_x$ . Also, the trends found in device parameters for varying thickness of  $\text{MoO}_x$  and TaTm are evaluated.

**Chapter 7** concludes the findings of the research and answers the research questions described in Chapter 1. The potential of using thermally evaporated  $\text{MoO}_x$  and TaTm as opposed to the spincoated PTAA is discussed. Finally, recommendations on future research related to using  $\text{MoO}_x$  and TaTm to create fully thermal evaporated PSCs are given.



# 2

## Theoretical background

The aim of this chapter is to provide theoretical background on the fundamental concepts for solar cells and the perovskite solar cell used in this study. Section 2.1 discusses the working principle of semiconductors. An overview of different hole transport materials and deposition techniques for perovskite solar cells is provided in Section 2.2. Lastly, Section 2.3 explains high-work function hole transport layers and the associated charge carrier transfer in perovskite solar cells using such a hole transport layer.

### 2.1. Semiconductor physics

#### 2.1.1. Semiconductor junction

The energy diagram shows the allowed electron energy states as a function of position. The Fermi level represents the average energy of electrons. Therefore, its position in the bandgap is influenced by doping. In materials with a high concentration of electrons (also referred to as n-type in c-Si), the Fermi level is closer to the conduction band, whereas the Fermi level is closer to the valence band in materials with a high concentration of holes (also referred to as p-type in c-Si). When p-type and n-type materials are brought together, a so-called space-charge region (SCR) is created. The SCR only contains ionized donor and acceptor atoms, as the mobile charge carriers are depleted due to the diffusion of holes from the p-type to the n-type region. An internal electric field results from the SCR. This forces the charge carriers to move in opposite direction of the concentration gradient, and is also called drift. The SCR is represented in the energy diagram by the grey region in figure 2.2. When a heterojunction is formed, the Fermi level of the two material must align, as the average energy of electrons (also described as the Fermi energy) is constant across the junction. The vacuum energy and the band-edge energies must be continuous and therefore a bending occurs in the bands. The bending indicates an electric field, which causes a difference in electrostatic potential difference  $V_{bi}$  across the SCR [169].

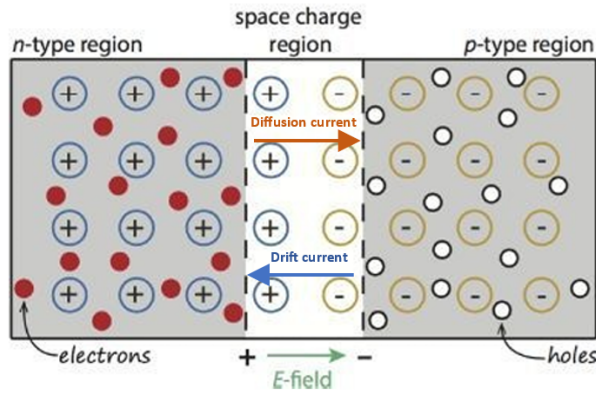


Figure 2.1: Space charge region in a heterojunction [169]

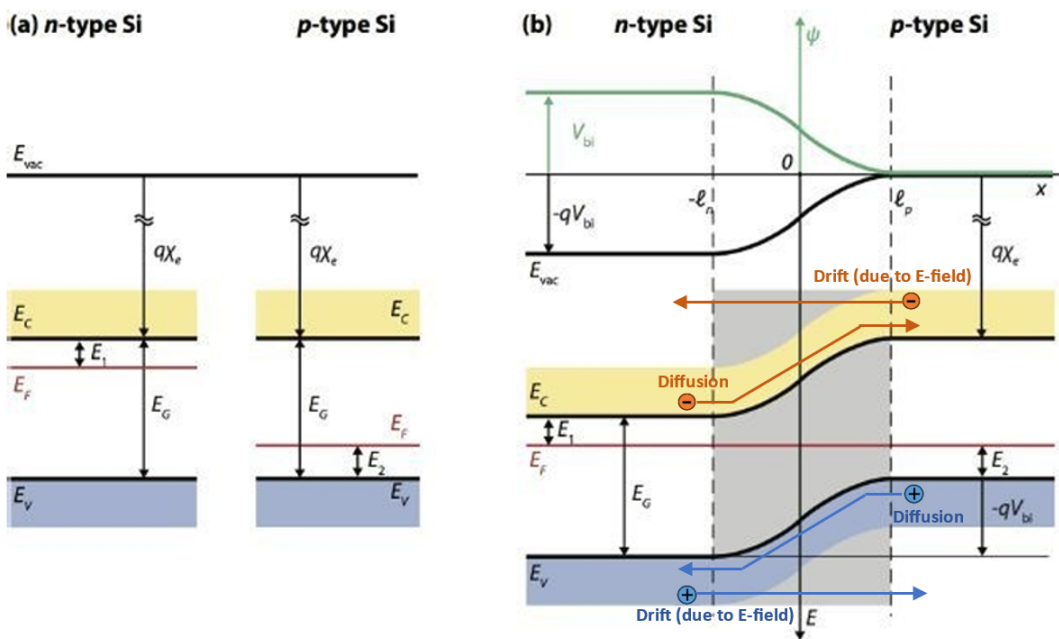


Figure 2.2: Energy diagram of a heterojunction [169]

### 2.1.2. Generation and recombination

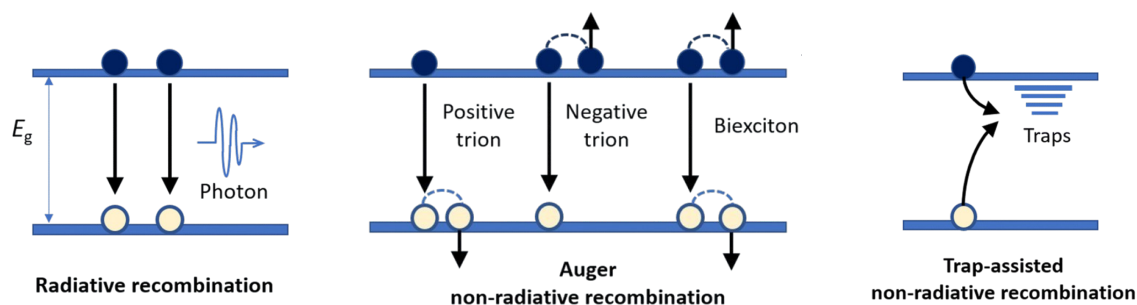
Generation is the formation of free charge carriers in a semiconductor through absorption of photons [66]. Photons are absorbed when light penetrates the material. If the photon energy is larger than the semiconductor's bandgap energy, there is adequate energy to excite an electron from the valence band to the conduction band. This leaves a hole in the valence band, and thus free charge carriers are formed [169].

Recombination is the process in which an excited electron in the conduction band loses its energy and falls back to the valence band and occupies a hole. Depending on the type of recombination process, the energy lost as a result of recombination is in the form of heat or light. There are three types of recombination processes, which are depicted in Figure 2.3:

- Radiative recombination: Radiative recombination is also known as band-to-band or direct recombination, and is the inverse of light absorption [164]. An electron in the conduction band loses energy and transitions back to the valence band where it recombines

with an hole [169]. The electron emits a photon (light describes as a wave and particle) that has the same energy as the band gap [24].

- Auger recombination: This is a three-particle process where the energy of a recombining charge carrier is transferred to another charge carrier [169][164]. If the receiving charge carrier is an electron, it will excite to higher levels in the CB. If the receiving charge carrier is a hole, it will excite to deeper levels in the VB [169]. In both cases, the charge carrier will relax back to their band edge and releases the energy and momentum to phonons (lattice vibration describes as a wave and particle) [164]. No light is emitted, so Auger recombination is a non-radiative process. Auger recombination strongly depends on the charge carrier density since it is a three-particle process [169].
- Shockley-Hall-Read (SHR) recombination: This recombination occurs at defects that are present in the crystal lattice. The defects have energy levels that lie in the energy bandgap. Here, a charge carrier can be trapped and recombination will occur when the opposite charge carrier is trapped in the same defect [169][164]. If the defects are close to one of band edges, recombination is less probable. Therefore, this recombination is most effective for states close to the mid-gap [24]. SHR recombination is a non-radiative process, where the dissipated energy is in the form of heat.



**Figure 2.3:** Band diagram of Radiative recombination, Auger recombination, and Shockley-Hall-Read (SHR) recombination [31].

### 2.1.3. Semiconductor interface phenomena

#### Surface states

The most discussed phenomenon that occurs near the interface are surface states. The energy gap is based on the infinite periodic structure of a semiconductor. However, near the boundary of a semiconductor, there is a discontinuity of the infinite crystal lattice of the semiconductor due to the start of a material with a different crystal lattice. Figure 2.4a shows the discontinued lattice at the interface of Ge-NC and  $\text{SiO}_2$ . This causes the occurrence of surface states, which are electron states in the bandgap near the interface as depicted in Figure 2.4b [126]. Surface states can lead to more complex phenomena, such as dangling bonds, the adsorption of impurity atoms, change of position and/or chemical configuration of atoms at the interface, irregularities at the interface, etc. [91]. Interface states can have a serious influence on the performance of a solar cell, as they increase Shockley-Hall Read recombination and can trap charge carriers at the interface [169].

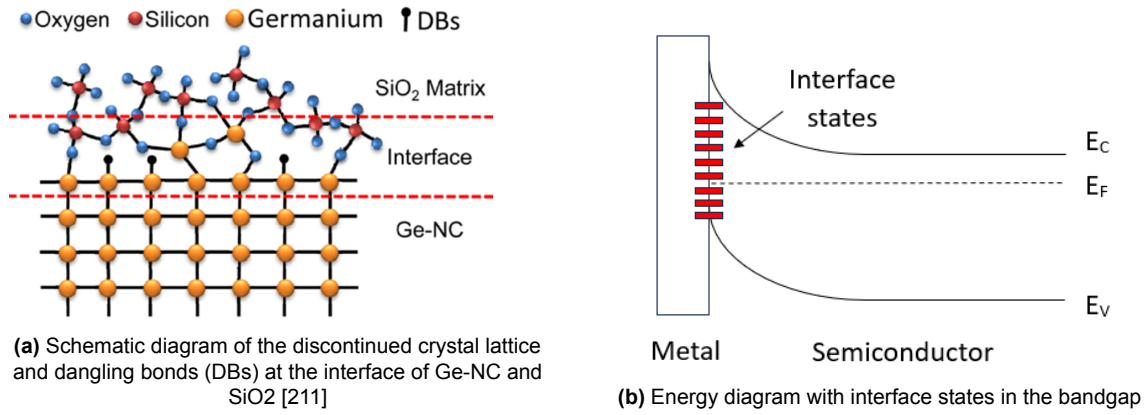


Figure 2.4: Interface states

Dipole

The formation of dipoles is another interface phenomenon. In general, a surface dipole is explained using the “spillout effect”. Here, a surface-located electron wave function has a ‘tail’ spilling out into the vacuum (see figure 2.5). This results in surface having a net positive charge and the region just outside the surface having a net negative charge. This separation of positive and negative charge is defined as a dipole. When electrons reach the surface, they are repelled by the negative charge outside the surface and attracted to the positive charge inside the material, thus creating a field that resists electrons from leaving the material into the vacuum [91].

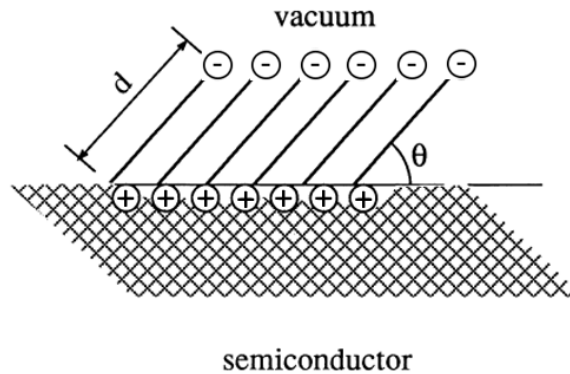


Figure 2.5: Schematic of a surface dipole [91].

Dipoles also arise at semiconductor interfaces. As an dipole induces diffusion of charge carriers, an electric field in opposite direction is set up to counteract the flow. Thus, an interface dipole creates a SCR and causes bending of the bands [91].

The orientation of an interface dipole determines whether it is the transport of holes or electrons that improves. When the positive side of a dipole is pointing towards material 1 (represented by the right energy diagram in figure 2.6), the vacuum level of material 2 will go upward and therefore the work function is increased. For simplicity, this is called a ‘positive’ dipole. The valence band is moved upwards, which improves the hole injection from material 1 into material 2. With a ‘negative’ dipole (the left energy diagram in figure 2.6), the positive side is pointing outwards of material 1. This will move both the vacuum level and conduction band of material 2 downwards, which increases the work function and improves electron injection from material 1 into material 2, respectively [25][57].

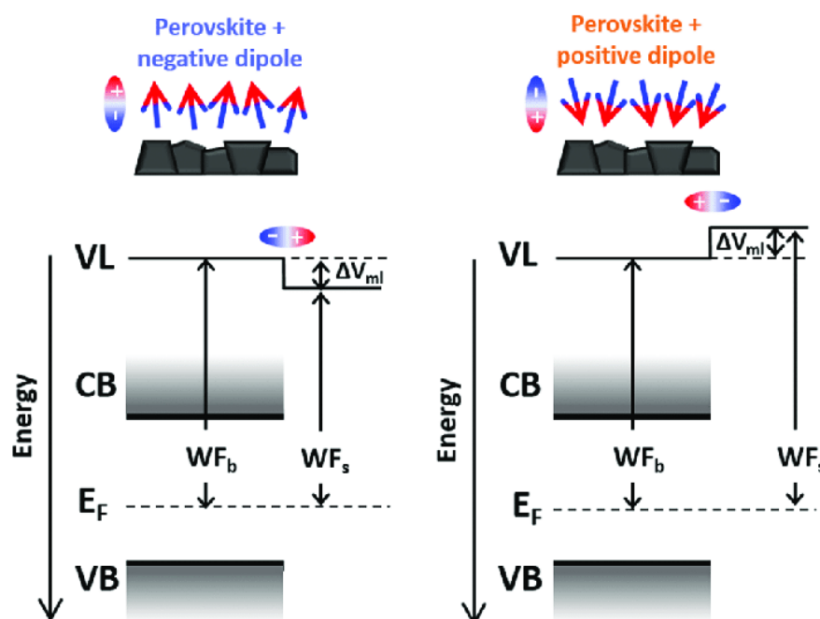
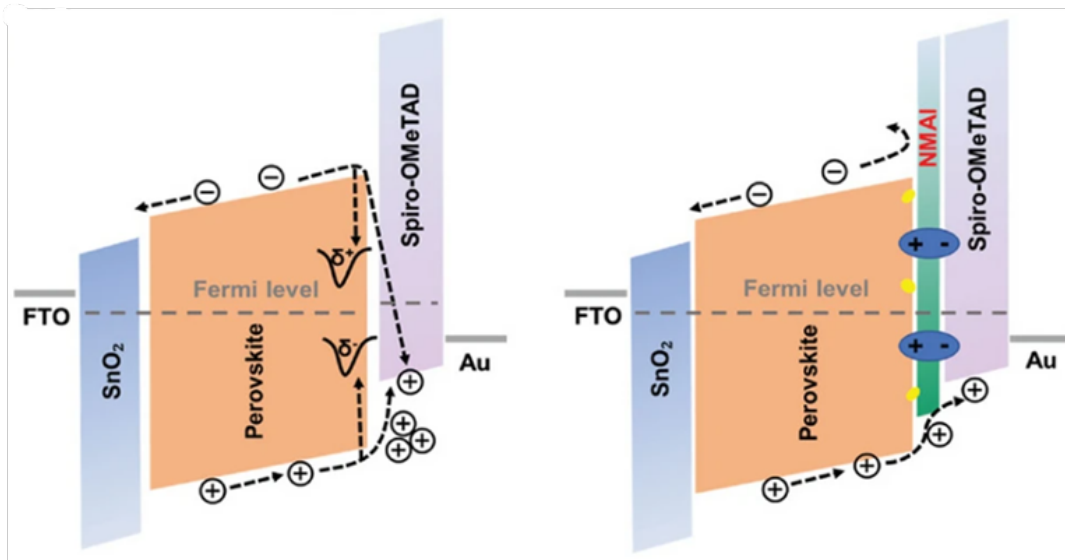


Figure 2.6: Interface dipole [25]

#### Dipoles to passivate surface states

The surface of perovskite suffers from interface states and dangling bonds that act as trap defects. This increases charge accumulation and leads to recombination losses. The density of states (DOS) can be reduced by the generation of dipoles, which function as field-effect passivation (FEP). The interface dipoles from insertion of a dielectric film result in the repulsion and separation of free charges at the interface, therefore, reducing the minority carrier recombination [117]. This is demonstrated in a study by Gao et al. [107]. Chemical passivation was created to reduce the defect-assisted recombination on the interface of the perovskite by using a dielectric ammonium salt. The energy level bending by the salt also reduced charge accumulation and resulted in an FEP that repelled minority carrier recombination. Figure 2.7 shows the dipole induced by the ammonium salt and how this repels electrons and prevents recombination.



**Figure 2.7:** A perovskite solar cell without FEP (left) and with FEP (right). The FEP-induced interface dipole blocks electrons and prevents recombination [107].

#### 2.1.4. J-V curve

The performance of solar cells is characterized with the illuminate J-V curve. The measurement to obtain the J-V curve is performed under standard test conditions (STC). Here, the irradiance on the solar cells ( $P_{in}$ ) is equal to 1 sun, which is  $1000 \text{ W/m}^2$  at AM1.5G [169][49]. The J-V curve consists of several main parameters and are depicted in Figure 2.8:

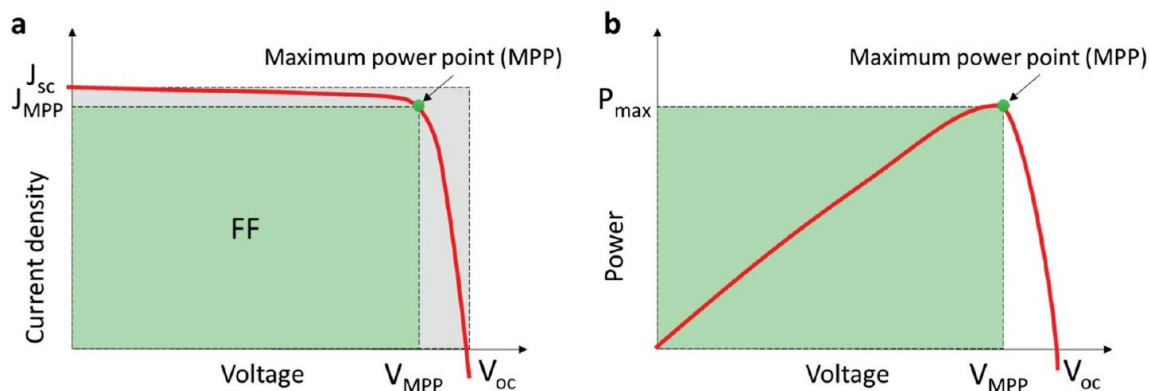
- Short circuit current density ( $J_{sc}$ ): The current when the solar cell's electrodes are short circuited. When the circuit is short circuited, the voltage is equal to zero [169].
- Open-circuit voltage ( $V_{oc}$ ): The maximum voltage of a solar cell. This is reached when no current is flowing through the circuit, meaning the current is equal to zero [169].
- Maximum power ( $P_{max}$ ): The maximum power that can be generated by the solar cell. The corresponding voltage and current are the maximum power point voltage,  $V_{mpp}$ , and the maximum power point current,  $J_{mpp}$ , respectively [49].
- Fill factor (FF): The ratio between the maximum power generated and the product of the  $V_{oc}$  and the  $J_{sc}$  [169][49]:

$$FF = \frac{P_{max}}{V_{oc} \cdot J_{sc}} = \frac{V_{mpp} \cdot J_{mpp}}{V_{oc} \cdot J_{sc}} \quad (2.1)$$

The fill factor is represented by the green square under the J-V curve in Figure 2.8. The fill factor is negatively affected by shunt resistance and series resistance.

- Power conversion efficiency (PCE): With the abovementioned parameters, the percentage of power generated by the solar cell from the incoming illumination can be calculated [169][49]:

$$PCE = \frac{P_{max}}{P_{in}} = \frac{V_{mpp} \cdot J_{mpp}}{P_{in}} = \frac{V_{oc} \cdot J_{sc} \cdot FF}{P_{in}} \quad (2.2)$$



**Figure 2.8:** J-V curve (left) and P-V curve (right) with solar cell parameters  $V_{oc}$ ,  $J_{sc}$ ,  $V_{mpp}$ ,  $J_{mpp}$ ,  $P_{max}$ , and FF [49]

## 2.2. Perovskite solar cell

### 2.2.1. Hole transport materials

There are many different HTMs that have been used in PSCs. They can be categorized in organic and inorganic HTMs. Organic HTMs:

- Spiro-OMeTAD  
2,2',7,7'-tetrakis (N,N-dip-methoxyphenyl-amine)- 9,9'-spirobifluorene (spiro-OMeTAD) is one of the most popular HTMs in PSCs, as it paved the way to achieving high performance PSCs in a very short period [184]. Spiro-OMeTAD was initially used in dye-sensitized solar cells where it achieved a PCE of only 0.74% [113][79]. This is because Spiro-OMeTAD has low hole mobility and conductivity due to its unique and pristine structure [113][184]. Additives 4-tert-butylpyridine (t-BP) and Li[CF<sub>3</sub>SO<sub>2</sub>]<sub>2</sub>N have been used to increase the aforementioned PCE to 2.56% [92]. The spiro-OMeTAD can be structurally changed to adjust its HOMO energy level [32][79]. Jeon et al. changed the position of the methoxy (-OCH<sub>3</sub>) group to create three different alterations: pp-Spiro-OMeTAD, po-Spiro-OMeTAD, pm-Spiro-OMeTAD. The HOMO energy level went from -5.22 to -5.31 eV and the devices with the altered Spiro-OMeTAD reached PCEs of 14.9%, 16.7% and 13.9%, respectively [78]. Hu et al. took another approach by using nitrogen and sulfur substituents to adjust energy levels, of which the spiro-OMeTAD with the sulfur substituents reached the highest PCE of 15.9% [69]. Despite being able to increase the conductivity of Spiro-OMeTAD with doping and alterations, the synthesis is complex and high-cost and limits the large-scale application in the future [113][184][32][79].
- P3HT  
Poly(3-hexylthiophene) (P3HT) has been shown to be a comparable HTM with spiro-OMeTAD due to its cost-effectiveness, easy processing and high mobility [184][79]. Bi et al. were the first to create PSCs using P3HT as HTM, resulting in a PCE of only 4.5%, despite P3HT's great optoelectrical properties [23]. The great potential of P3HT was shown by Giacomo et al. when they used it as HTM in PSCs reaching a PCE of 9.3% [51]. Sequential vapor deposition of the perovskite and adjusting the thickness of the P3HT layer resulted in a PCE of 13.7% for Abbas et al. [1].  
Despite the great properties of P3HT, it also has flaws such as strong electronic coupling and poor physical contact between the P3HT and the perovskite, which results in a lower performance [32]. Nia et al. were able to overcome these flaws by using a crystal-engineering approach to deposit the perovskite. The contact between P3HT and the

perovskite improved substantially, resulting in a PCE of 16.8% [132]. Lastly, surface contact was improved and interface recombination between the P3HT and the perovskite layer was reduced by Jung et al. They introduced a thin layer of halide perovskite with a wide bandgap in between the P3HT and the perovskite film, which obtained an PCE of 22.7% [81].

- PEDOT:PSS

Poly (3,4-ethylenedioxythiophene): polystyrene sulfonate (PEDOT:PSS) is another extensively used HTM due to its high transmissivity and low manufacturing cost [79]. Devices with PEDOT:PSS as HTM often use an organic ETM such as [6,6]-phenyl C61-butyric acid methyl ester (PCBM) or indene-C60 bisadduct (ICBA) [113][184]. You et al. achieved a PCE of 11.5% with such structure, which was raised to 12.0% by Chen et al. after optimizing the perovskite layer thickness [201][30]. Higher PCEs of 14.1% and 20.1% were reported, increasing interest using PEDOT:PSS in combination with the ETM PCBM [161][77]. Despite the high performances using PEDOT:PSS as HTM, its acidic and hygroscopic characteristics seriously limit the long-term stability [32]. Different dopants have been proposed to improve its properties. Dopamine was used to modify PEDOT:PSS (DA-PEDOT:PSS) by Huang et al, to reduce its acidity and therefore improving the stability of the device [70]. As DA-PEDOT:PSS has a higher work function than PEDOT:PSS, a PCE of 16.4% was achieved. Another doping method was used by Liu et al., who used F4-TCNQ as an additive in PEDOT:PSS, increasing the PCE from 13.3% to 17.2% [109]. F4-TCNQ improves carrier transport from the perovskite layer to the HTL by altering the electrical properties of PEDOT:PSS and therefore lowering the HOMO level.

- PTAA

Poly[bis(4-phenyl) (2,4,6-trimethylphenyl)amine] (PTAA) is used in high performing PCEs due to its decent hole mobility and its proper HOMO level with respect to the perovskite layer [184][79][99]. Hao et al. were first to report on PSCs using undoped PTAA as HTM, which obtained a PCE of 12.0% due to greatly improved  $V_{oc}$  and FF [64]. Other undoped PTAA PSCs followed with throughout the years with PCEs of 15.3%, 18.0% and 18.2% [155][85][190].

Unfortunately, PTAA suffers from poor conductivity and doping is needed to improve device performance [79]. Liu et al. used different dopants for PTAA and found the biggest improvement from 14.2% to 18.2% using CuSCN [114]. NPB was later used as dopant by both Pathipati et al. and Liu et al., achieving PCEs of 18.2% and 20.2%, respectively [140][110]. NPB doping moves the VB energy of the PTAA closer to the perovskite layer and achieves a larger grain size of the perovskite.

However, since doping has its own shortcomings, other methods of improving device performance were researched without the use of doping. Surface treatment to modify the PTAA has been shown to be very effective [99]. Zhang et al. treated the PTAA with oxygen plasma to improve conductivity and reach a PCE of 19.0% [206]. The PTAA film was textured by Xu et al. to decrease the internal optical reflection and achieve a PCE of 20.8%. The use of an antireflection coating further improved the PCE to 21.6% [194]. Most recently, other interface modifications has led to PCEs of 23.7% and 25.0% [37][105].

#### Inorganic HTMs:

Inorganic semiconductor materials have desirable properties such as wide bandgap, high hole mobility, simple fabrication and low production cost [32][79]. There are many different inorganic compounds promising to replace organic HTMs:  $NiO_x$ ,  $CuO_x$ ,  $Cu_2O$ ,  $CuS$ ,  $CuI$ ,  $CuPc$ ,  $CuSCN$ ,  $CuCrO_2$ ,  $CuGaO_2$ ,  $CuInS_2$ ,  $Cu_2BaSnS_4$ ,  $CoO_x$ ,  $CoN$ ,  $MoO_x$ ,  $MoS_2$ ,  $VO_x$ ,  $GO_x$ ,  $PbS$



and  $\text{CrO}_x$  [9]. The most frequently used are discussed below

- $\text{Cu}_2\text{O}/\text{CuO}$

Cupric oxide ( $\text{CuO}$ ) and cuprous oxide ( $\text{Cu}_2\text{O}$ ) are suitable HTMs due to their energy levels matching well with perovskite, low cost, high hole mobility, environmental friendliness, and diverse fabrication possibilities [9][79]. Chatterjee and Pal used successive ionic layer adsorption and reaction (SILAR) method to obtain highly crystallized  $\text{Cu}_2\text{O}$  for the HTL [27]. With a structure of  $\text{ITO}/\text{Cu}_2\text{O}/\text{MAPbI}_3/\text{PCBM}/\text{Al}$ , a PCE of 8.23% was achieved. Yu et al. prepared a PSC with the structure  $\text{ITO}/\text{Cu}_2\text{O}/\text{MAPbI}_3/\text{PCBM}/\text{Ag}$  and used a thermal oxidation method for the deposition of  $\text{Cu}_2\text{O}$ . The optical transmission and series resistance were optimized by precise control of the thickness and properties of the  $\text{Cu}_2\text{O}$  layer, resulting in a PCE of 11.03% [202]. Both  $\text{CuO}_x$  and  $\text{Cu}_2\text{O}$  were tested as HTMs by Zuo and Ding using a simple low-temperature method to achieve PCEs of 12.2% and 13.4% respectively [213]. Better efficiencies using  $\text{CuO}$  was achieved by Sun et al. through facile solution-process method. A PCE of 17.1% was obtained for the device with the structure of  $\text{ITO}/\text{CuO}_x/\text{MAPbI}_3/\text{C}_{60}/\text{BCP}/\text{Ag}$  [175]. This PCE was later raised to 19.0% using  $\text{Cl}^-$  doping in  $\text{MAPbI}_3$  to create a hybrid  $\text{MAPbI}_{3-x}\text{Cl}_x$  perovskite as a light absorber [151].

- $\text{CuI}$

Copper iodide ( $\text{CuI}$ ) has relatively high hole mobility, large band gap ( $\sim 3.1$  eV) and facile preparation [9][184]. Christians et al. used  $\text{CuI}$  as HTM to achieve a PCE of 6.0% [33]. Even though this efficiency is rather low,  $\text{CuI}$  shows electrical conductivity five orders of magnitude larger than spiro-OMeTAD and was therefore worth exploring. Nejjand et al. prepared a device with the structure  $\text{FTO}/\text{CuI}/\text{MAPbI}_3/\text{PCBM}/\text{Al}$  using thermal deposition method for the  $\text{CuI}$  films, to obtain a PCE of 7.7% [130]. A similar PCE of 7.4% was achieved by Gharibzadeh et al. using a gas-solid reaction method for the deposition of the  $\text{CuI}$  [50]. This deposition method provided a uniform and compact  $\text{CuI}$  layer with large grains. The same deposition method was used by Wang et al. for PSC with the structure of  $\text{FTO}/\text{CuI}/\text{MAPbI}_3/\text{PCBM}/\text{PEI}/\text{Ag}$  [188]. Optimized conditions resulted in a remarkable PCE of 14.7%. Li et al. prepared the  $\text{CuI}$  film with a spray deposition method and used Na-treated  $\text{TiO}_2$ , which resulted in a PCE of 17.6% [103].

- $\text{CuSCN}$

Copper thiocyanate ( $\text{CuSCN}$ ) is a favorable HTM because of its high mobility, wide band gap ( $\sim 3.6$  eV), stable chemical properties and good transparency in visible and infrared region that facilitates high light absorption and high photocurrent generation [9][79].  $\text{CuSCN}$  is often used to replace the organic PEDOS:PSS, due to its better matching energy band levels with  $\text{MAPbI}_3$  [9].  $\text{CuSCN}$  was used as HTM with  $\text{CH}_3\text{NH}_3\text{PbI}_3$  as absorber layer to achieve a PCE of 4.9% by Ito et al. [76]. The same PSC was prepared by Chavhan et al. with  $\text{CH}_3\text{NH}_3\text{PbI}_{3-x}\text{Cl}_x$  as absorber layer to increase the PSC to 6.4% [28]. Zhao et al. used solution method at low temperature to achieve thin and smooth  $\text{CuSCN}$  films, which resulted in a PCE of 10.8% [212]. Ye et al. was able to minimize both surface roughness and interface contact resistance between perovskite layer and selective contacts using one-step fast deposition crystallization (FDC) as opposed to conventional two-step sequential deposition when creating the  $\text{MAPbI}_3$  films onto  $\text{CuSCN}$  layer [198]. This led to a PCE of 16.6%. As research on PSCs using  $\text{CuSCN}$  as HTM continued, numerous groups were able to create devices with PCEs between 16.0% and 19.0% [186][86][119][189][82][197][120][191]. A PSC with  $\text{CuSCN}$  as HTL has been reported to exceed 20% by Arora et al., who was able to create compact and highly conformal  $\text{CuSCN}$  layers using a fast solvent removal method [8]. This promoted rapid carrier extraction and collection.

- $\text{NiO}_x$

$\text{NiO}_x$  has attracted interest due to its high transmittance, high thermal/light stability, wide band gap of 3.5-3.9 eV, and a suitable work function that matches with the VB of  $\text{MAPbI}_3$  perovskite [9][79][99]. Besides these properties,  $\text{NiO}_x$  has the advantage of being low-cost, abundantly available, and synthesized with ease using cost effective techniques [9]. The first to report on the use of  $\text{NiO}_x$  as HTL in PSCs are Docampo et al., who obtained a PCE of <0.1% with the device structure of FTO/ $\text{NiO}_x$ / $\text{MAPbI}_{3-x}\text{Cl}_x$ /PCBM/Al [38]. Poor surface coverage of the perovskite and direct contact between the HTL  $\text{NiO}_x$  and the ETL PCBM were responsible for the low PCE. Hu et al. produced  $\text{MAPbI}_3$  instead of  $\text{MAPbI}_{3-x}\text{Cl}_x$  films, and used two-step sequential dipping method to improve the quality of the perovskite. Improved surface coverage and crack-free crystalline nature were observed, which yielded a PCE of 7.6% [68]. Later, the  $\text{NiO}_x$  films were prepared in different ways. A PCE of 9.83% was achieved by Cui et al. when preparing the  $\text{NiO}$  layer with magnetron sputtering [35]. Atomic layer deposition was used by Seo et al., which produced ultra-thin  $\text{NiO}$  films that resulted in a PCE of 16.4% [162]. Park et al. created  $\text{NiO}_x$  layers with pulsed laser deposition method to achieve a PCE of 17.3% [138].

Doping and surface treatment are often employed to improve conductivity and thus optimize the performance of the PSCs [99].  $\text{NiO}_x$  is frequently single-doped with copper ( $\text{Cu}^{2+}$ ), lithium ( $\text{Li}^+$ ), cobalt ( $\text{Co}^{2+}$ ), cesium ( $\text{Cs}^+$ ), silver ( $\text{Ag}^+$ ), magnesium ( $\text{Mg}^{2+}$ ), zinc ( $\text{Zn}^{2+}$ ), and iron (Fe). Double-doping is also used to mitigate the loss of light transmission that occurs with single-doping [9]. Xia et al. prepared Li/Ag codoped  $\text{NiO}_x$  films as HTL to achieve a PCE of 19.24% [193].

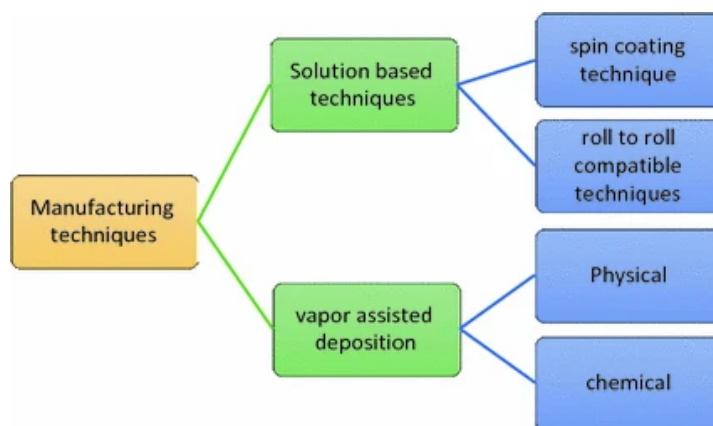
- $\text{MoO}_x$

Molybdenum oxide ( $\text{MoO}_x$ ) has been widely adopted due to its high work function (~6.9 eV), wide band gap (3.0-3.3 eV), high transparency in the visible region, ambient stability, low cost, abundant availability and nontoxicity [58][9][177][128]. It also creates optimal contact with ITO and has low parasitic absorption [142]. Despite its advantages,  $\text{MoO}_x$  suffers from low selectivity and exhibits poor surface coverage of perovskite films on  $\text{MoO}_x$  [9][142].  $\text{MoO}_x$  is therefore often used in combination with more selective contacts that will also improve a more uniform surface coverage. Increased hole transportation and more uniform coverage occur when  $\text{MoO}_x$  is used as an interlayer between ITO and PEDOT:PSS. The device with structure ITO/ $\text{MoO}_3$ /PEDOT:PSS/ $\text{MAPbI}_3$ /C<sub>60</sub>/Bphen/Ag achieved a PCE of 12.8%, as well as increased stability due to the ambient stability of  $\text{MoO}_3$  [67].  $\text{MoO}_x$  has recently also been used as an interlayer in combination with the newer organic HTM N4,N4,N4',N4'-tetra([1,1'-biphenyl]-4-yl)-[1,1':4',1'-terphenyl]-4,4'-diamine (TaTm). The research group by Bolink has investigated PSCs with  $\text{MoO}_x$ /TaTm as HTL and has repeatedly shown PCEs of over 18.0% for devices with different HTL thicknesses, annealing conditions, perovskite materials, ETMs and deposition methods [13][142][36][143][170][14][171][15][204].

### 2.2.2. Deposition methods

There are many deposition methods to manufacture perovskite solar cells. This applies not only for the PVK absorber layer, but also for the other layers required to fabricate PSCs such as the charge transport layers and the electrodes depicted in Figure 1.7 [163]. It is critical to select the proper deposition method to obtain smooth, pinhole-free films with well-controlled crystal shape and optoelectrical material properties. Figure 2.9 shows the categorization of the manufacturing techniques [83]. The main two methods to fabricate laboratory-scale PSCs are solution process and vapor deposition process. The most widely used deposition method is a solution process called spin-coating. Its popularity is due to ease of perovskite synthesis and

low cost [16]. The film thickness and quality is optimized by the spin-coating parameters: controlling spin speed, spin time and spin acceleration [83]. The solvent used in the spin-coating method also impacts the film surface quality, as it affects the crystallization rate [16]. On small areas, spin coating can be used to create sufficiently uniform films. However, uniform films cannot be produced on larger areas, due to varying thickness across the area and the large number of pinholes that arise [83][16][4]. Other limitations of large scale manufacturing using spin-coating is the high material wastage and the large number of variables that affect the film quality [83][16].



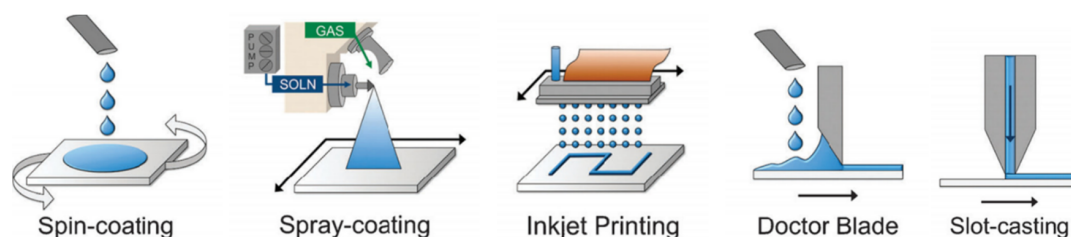
**Figure 2.9:** Manufacturing techniques for perovskite solar cells [83]

Solution processing technique that are suitable for large scale manufacturing is roll-to-roll printing. The highly reproducible technique uses rotating rolls to move the substrate while depositing a thin film on it [83]. Figure 2.10 illustrates the different coating methods for the deposition of the thin-film [179]. They can be described as follows:

- **Spray coating:** It is a contactless, printing-friendly technique that uses a nozzle to disperse atomized liquid droplets on substrates [106][111][139]. The size of the droplet and the deposition location of the droplet are random in the spraying process. For full coverage, local overlap of several droplets is needed [106]. This method can be classified based on the type of dispersion: Pneumatic spraying (by fast gas flow), ultrasonic spraying (by ultrasonic vibration) and electrospraying (by electrostatic repulsive force) [178][106][154]. Compared to spin coating, spray-coated films have better charge transfer capability and higher minority carrier lifetime, which results in better optoelectronic properties and higher thermal stability [83].
- **Ink-jet printing:** This is another non-contact droplet-based technique that uses a nozzle to disperse the precursor ink with precise control of the droplet size and deposition path [106][111]. The external bias application causes the liquid-filled nozzle to contract and eject a liquid droplet [83]. Although piezoelectricity is the most-used method to cause the pressure change, other methods including thermal sources and structural sources exist as well [178]. The advantage of ink-jet printing is that it does not require the substrate to be of certain material or shape and the need for laser scribing is eliminated due to the direct patterning of the printer layers [178][154].
- **(Doctor) Blade coating:** A blade is used to spread precursor solution on substrate to form a liquid thin films [178][106]. The film thickness and quality is controlled by speed of the blade moving over the substrate, the precursor ink concentration, and the gap between the blade and the substrate [106][111][154][139]. The advantages of this method is that

it is simple, vacuum free and low cost [154][83]. However, its simplicity also has its downfall. There is no precise control of ink used and the ink chemistry may change over time as the ink does not sit in a fully enclosed reservoir [178][83].

- Slot-die coating: Slot-die casting is similar to blade coating, applying ink over the substrate using an ink reservoir with a thin slit [106][154]. The film thickness depends on the geometry of the blade, web speeds, and ink feeding rate [178][139]. Slot-die casting has the advantage of less material wastage and better control of the ink flow [106][83]. However, filling the ink reservoir and the supply pipe requires large quantities of ink and this method therefore remains at early stages of development [106][111][154]. It must be noted that slot-die coating does have large potential of being used in large-scale roll-to-roll fabrication of PSCs in the near future [106][111].



**Figure 2.10:** Solution processing techniques for fabrication of perovskite solar cells [179]

Vapor deposition, also known as vacuum-based deposition, is an alternative to solution-based deposition of perovskites where the precursor materials are deposited in vapor phase at pressures below atmosphere [178]. Whereas solution-based can produce micrometer thick films, vacuum-based deposition has high control of the material thickness down to in nanometers [83]. With respect to solution-based techniques, these films are highly crystalline and more uniform on large areas [83][4]. Vacuum-based deposition has been successfully applied in large scale fabrication of PSC [106]. The only downside to this deposition method is the requirement of high vacuum ( $10^{-7}$  -  $10^{-3}$  mbar) to increase the mean free path of the evaporated materials, which is necessary to produce the highly uniform and highly pure thin films [178][83]. Vapor deposition can be divided into physical vapor deposition (PVD) and chemical vapor deposition (CVD). CVD are processes that initiate chemical reactions through pressure, temperature, or plasma conditions, all in presence of specific chemicals that support the reaction. Tubular flow reactors use inert transport gas inlet and a vacuum outlet to guide the chemicals to the substrate [178].

PVD are processes that form a perovskite thin film by directly sublimating perovskite or their precursors [106]. The most common PVD is the thermal evaporation method, where either a perovskite precursor is directly synthesized and evaporated in a high-temperature tungsten boat (dual source evaporation), or a perovskite is evaporated after being prepared separately in a tungsten boat (single source evaporation) [16]. As PVD is solvent-free, traps and defect sites that are formed by the solvent for precursor synthesis are avoided, resulting in uniform films without pinholes [139]. The deposition becomes more uniform the longer the path length between the evaporation source and the substrate. However, a longer path length does result in reduced material yield due to parasitic condensation on the chamber walls [178]. There are three different ways in which perovskites can be evaporated: co-evaporation of different material components (simultaneous multi source evaporation), sequentially evaporating of different material components (sequential multi source evaporation), and flash evaporation of a perovskite bulk material (single source evaporation) [178][16].

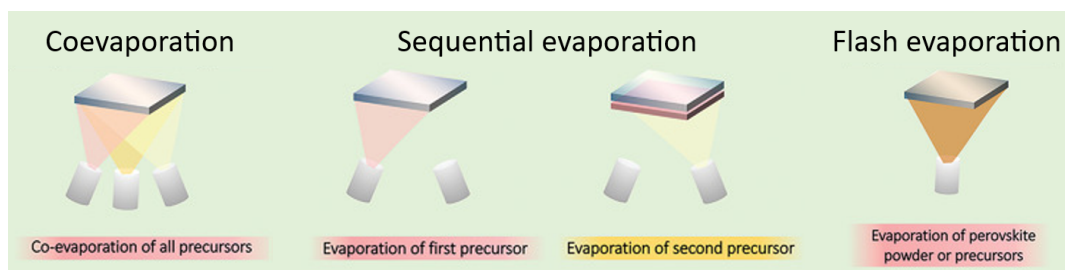


Figure 2.11: Thermal evaporation techniques [185]

## 2.3. PSCs with high work function HTLs

### 2.3.1. TMOs

The transition metal oxides (TMOs) can vary in a large range of work functions. Controlling the work function can be quite the challenge, as it is affected by the electron chemical potential and surface dipole [58][52]. Both are influenced by several factors: the chemical potential is determined by the material's chemical identity, its stoichiometry and the presence of any impurities, whereas the dipole depends on radiation exposure, adsorbate coverage and surface roughness [52]. Especially the stoichiometry is of large influence on metal oxides, as it changes across a wide range. This is due to several different defects, such as vacancies and interstitials of both cation and oxygen. In general, the increase of oxygen increases the work function [53][207][58][56][52]. This is because a lower stoichiometry means more oxygen vacancies, which results in cations with reduced oxidation states. An increase in reduced cation concentration leads to the decrease of an oxide's group electronegativity and as a consequence also the decrease of its work function [52][55]. This relation between oxygen, cation concentration and work function has been proven for the metal oxide  $\text{MoO}_x$ . The oxidization of  $\text{MoO}_x$  increases the O/Mo ratio, and the results have shown the increase in work function and the conversion of  $\text{Mo}^{4+}$  to  $\text{Mo}^{5+}$  and  $\text{Mo}^{6+}$  [20][56].

However, not every TMO behaves the same, as each TMO is more prone to a certain defect. Depending on the defect, a metal oxide is acting like a n-type or p-type material. For example, metal oxides like  $\text{NiO}_x$  are 'intrinsic' p-type semiconductors due to its native O interstitials [52]. Many other TMOs like  $\text{MoO}_x$ ,  $\text{WO}_3$  and  $\text{TiO}_2$  are 'intrinsic' n-type semiconductors due to the native O vacancies. Therefore, the oxygen vacancies can be considered n-type dopants, which raise the Fermi level and decrease the work function [53][207][52].

### 2.3.2. Tunneling

In the classic physics, an electron would need to have enough energy to get past a potential barrier. However, in the quantum physics there is a phenomenon called quantum tunnelling. Here, a particle is able to tunnel through the potential barrier. Particles that according to the classic physics do not have enough energy to get past a potential barrier, are now able to get to the other side of the barrier. This process is represented in figure 2.12. In quantum physics, a particle is presented as a wave function. The probability function of a particle is represented in figure 2.13, and its amplitude is lower than the height of the potential barrier. When tunnelling through the barrier, the amplitude decreases exponentially, meaning the probability of finding the particle inside the barrier reduces. If the barrier is not too wide, the probability function will be non-zero on the other side on the barrier, meaning the particle was able to move through the barrier. Its amplitude is lower than before tunnelling though the barrier, thus it is less probable to find the particle past the barrier than before the barrier. The energy of the particle remains the same [46].

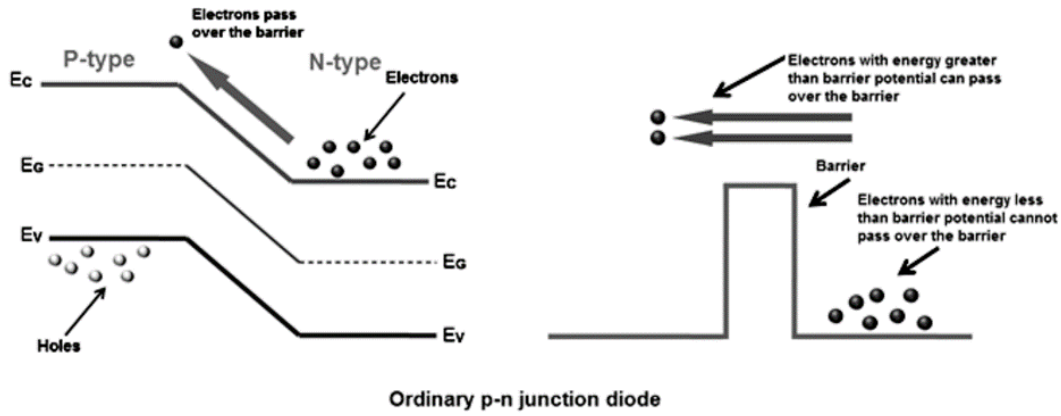


Figure 2.12: Ordinary heterojunction diode [146]

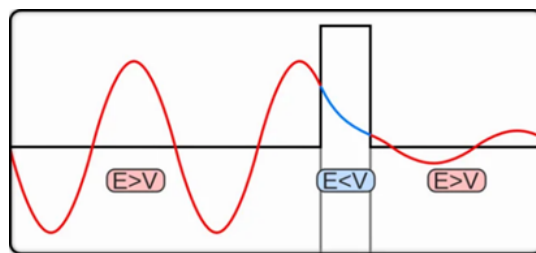


Figure 2.13: Quantum tunnelling projected as a wave function [46]

Quantum tunnelling can also occur through the band gap. Figure 2.14 depicts a tunnel diode, where both sides of the heterojunction are highly doped, resulting in a very narrow depletion region. The high electric field across the depletion region causes the Fermi level of the p-region to go below the valence band and the Fermi level of the n-region to go above the conduction layer. Electrons in the n-region’s conduction band are able to tunnel through the narrow depletion region to the valence band of the p-region, and vice versa [149][22].

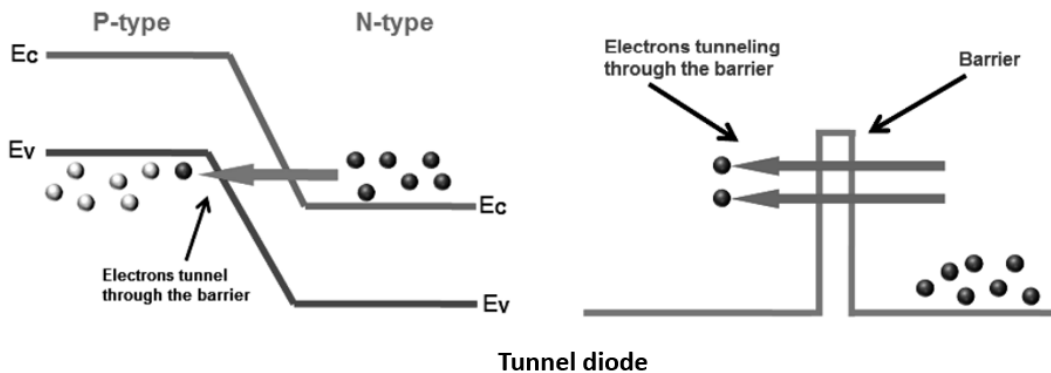


Figure 2.14: Tunnel diode [146]

### 2.3.3. Band diagram

The transfer of holes from the PVK to the electrode typically happens through the valence band. However, when using high-work-function HTLs such as  $\text{MoO}_x$ , other transfer occurs. The band diagram of  $\text{ITO}/\text{MoO}_x/\text{TaTm}/\text{PVK}$  is shown in figure 2.15. Holes in the VB of the PVK move through the VB of the TaTm to the  $\text{MoO}_x/\text{TaTm}$  interface. The electrons in the CB of the PVK

are blocked at the TaTm/PVK interface. On the other side, the electrons in the CB of the ITO are moving towards the MoO<sub>x</sub>/TaTm interface, attracted by to the accumulation of holes in the TaTm VB near the interface. On this path, the electrons tunnel through the small "spike-like" barrier at the ITO/MoO<sub>x</sub> interface. At the MoO<sub>x</sub>/TaTm interface, the electrons tunnel to the VB of the TaTm and recombine with the holes. The electrons recombining with the holes promotes continuous extraction of electrons from the ITO to the MoO<sub>x</sub>/TaTm interface. The electrons moving from the ITO to the MoO<sub>x</sub>/TaTm is equivalent to holes moving from the MoO<sub>x</sub>/TaTm interface to the ITO.

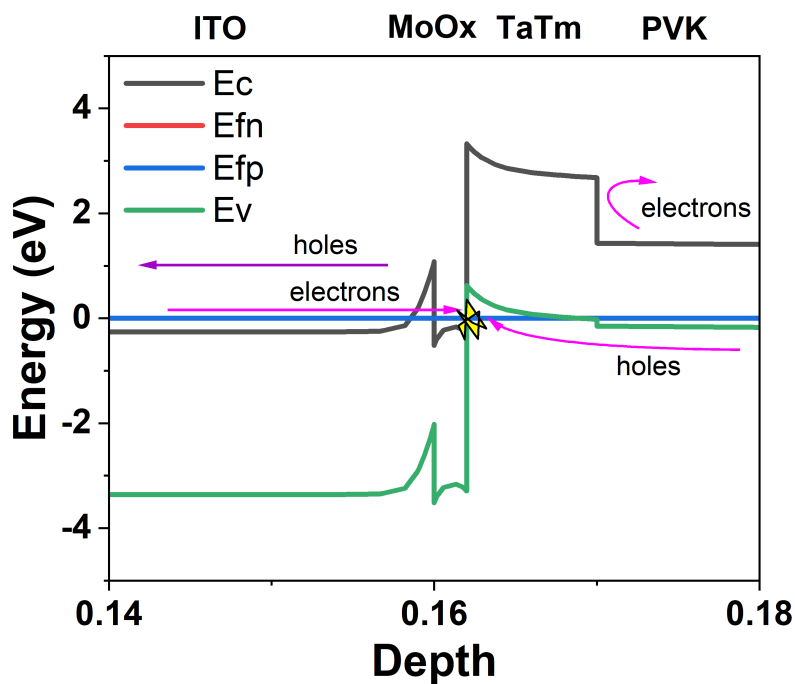


Figure 2.15: Band diagram of the front side of the PSC (ITO/MoO<sub>x</sub>/TaTm/PVK)

# Research Methodology: Fabrication and Characterization Methods

This chapter pertains to the methodologies for the fabrication characterization of the solar cells. Section 3.1 discusses the used deposition methods for the film layers. The fabrication of the solar cells is described step-by-step in Section 3.2. The working principles and the parameter settings of the characterization methods used in this study are explained in 3.3.

## 3.1. Deposition methods

### 3.1.1. Thermal evaporation

Thermal evaporation is a physical vapor deposition technique for thin-films where the precursor materials are deposited in vapor phase in high vacuum atmosphere. Figure 3.1 shows the thermal evaporation of the perovskite  $\text{Cs}_{0.15}\text{FA}_{0.85}\text{PbI}_{2.85}\text{Br}_{0.15}$ . Vacuum increases the mean free path of the evaporated materials, which results highly uniform and highly crystalline thin films. The deposited film becomes more uniform the longer the path length between the evaporation source and the substrate. However, a longer path length does result in reduced material yield due to parasitic condensation on the chamber walls [178][83].

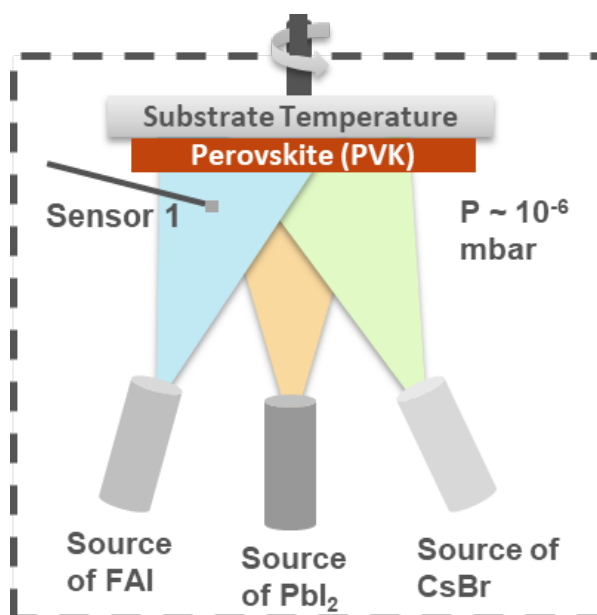
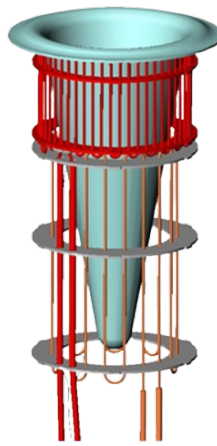


Figure 3.1: Thermal evaporation of  $\text{Cs}_{0.15}\text{FA}_{0.85}\text{PbI}_{2.85}\text{Br}_{0.15}$  [195].



In order for the material to travel from the source to the substrate, the material must sublimate. This is done by heating it up to the point where the vapor pressure of the material exceeds that of the vacuum environment [147]. Thermal evaporation most often uses resistive heating, where heat is produced by passing current through a non-conductive material such as a highly resistance wire. The wire is wound around the quartz crucible, which holds the powered source material [19], as depicted in Figure 3.2. The amount of current needed for heating the source material depends on the desired deposition rate of the evaporated material. In general, the higher the current, the higher the temperature and the higher the deposition rate of the evaporated material [40]. Therefore, thermal evaporation starts by increasing the current through the resistance winding to increase the temperature. When the desired deposition rate is reached, a shutter covering the substrate moves to allow the vapor stream to reach the substrate and start growing the film. The substrates are rotated to improve the uniformity of the deposited films [60].



**Figure 3.2:** Crucible with resistive winding to heat the source material [39].

Quartz crystal microbalance (QCM) sensors monitor the deposition rate (in Å/s) and the deposited thickness (in Å) and are therefore of great importance to an accurate deposition. The QCM is a piezoelectric material, which will produce an internal mechanical stress when exposed to an external electrical potential. When this is an oscillating electric field, an acoustic wave is induced that propagates through the crystal and the QCM starts to mechanically oscillate at a certain frequency [134]. The changes of the oscillation frequency are related to the accumulated mass on the surface of the QCM [203]. Therefore, the deposited thickness and the deposition rate can be determined by monitoring the frequency changes. Additional information about the deposited material is needed:

- Material density
- Tooling factor: The tooling factor (TF) is the correction between the deposited thickness on the QCM and the deposited thickness on the substrate [26]. The tooling factor depends on the evaporated material, the sensor position, the substrate position, the source position, and the geometry of the chamber [7]. The TF is calculated as follows:

$$TF = \frac{t_{actual}}{t_{sensor}} \quad (3.1)$$

where  $t_{actual}$  is the deposited thickness on the substrate and  $t_{sensor}$  is the deposited thickness on the sensor.

Each material has a unique tooling factor that only needs to be determined once, provided that the position of the QCM, the source and the substrate holder does not change.

- Z ratio: The Z-ratio is used to match the acoustic properties of the deposited material to the acoustic properties of the quartz material of the sensor, in order to correct the frequency changes that are monitored for the deposition rate and thickness determination [26]. The Z-ratio is calculated as follows [203]:

$$Z - ratio = \frac{Z_{quartz}}{Z_{material}} \quad (3.2)$$

where  $Z_{quartz}$  is the acoustic impedance of quartz and  $Z_{material}$  is the acoustic impedance of the deposited material.

The Z-factor is not known for many materials. The Z-factor can be determined empirically, according to the steps shown in Appendix B. Alternatively, accurate depositions can be done without knowing the Z-factor by changing the QCMs frequently. For QCMs with a life above 85%, the error between the programmed and the actual Z-factor is negligible.

The machines used to fabricate the thermal evaporated films are the OPTIvap and PER-Ovap by the company MBRAUN<sup>®</sup> (see Figure 3.3). Both machines are integrated in a glovebox to operate in a nitrogen environment. This minimizes the exposure of oxygen and water to the materials, while simultaneously protecting the operator from potentially harmful materials used in the process.

The MoO<sub>x</sub>, TaTm, C60, BCP and silver are deposited with the OPTIvap. The vacuum chamber contains six sources with four QCMs. Above the sources the substrate holder is placed, which rotates up to 30 rpm during deposition. The substrate holder holds a mask in which 25 substrate of the size 25x25 mm can be placed. The flux of evaporated material going from the sources to the substrates can be blocked by controlling dedicated shutters for each source and the substrate shutter.

The perovskite is deposited with the PEROVap. This vacuum chamber contains four sources that each has its own QCM to enable a precise control of each precursor source. This system allows for a simultaneously deposition up to 4 sources, making the system suitable for co-evaporation or sequential evaporation. The sources are placed within an inner enclosure to allow the temperature to go as low as -40°C. The substrate holder and the shutters are the same as with the OPTIvap.

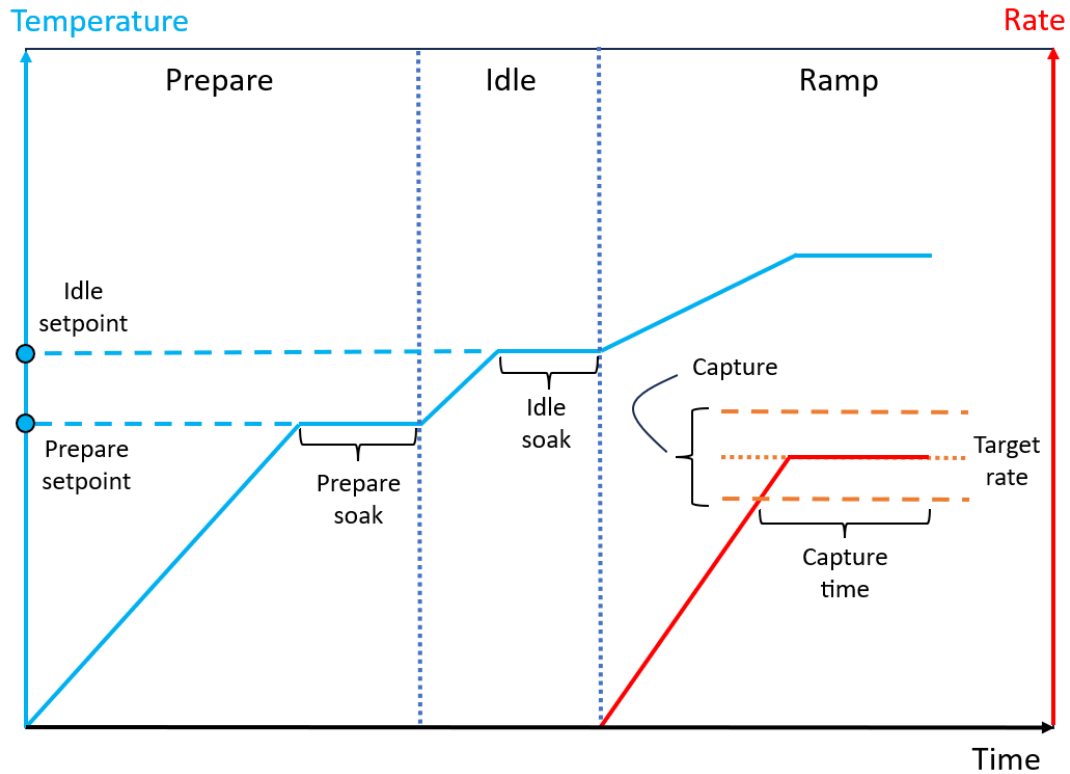


**Figure 3.3:** Deposition machines: OPTIvap2 (for HTL and ETL deposition), PEROVap (for PVK deposition) and OPTIvap1 (for Ag deposition).

The deposition sequence for the OPTIvap and PEROVap:

1. Loading: Samples are placed in the mask and loaded in the substrate holder. The crucibles in the sources are filled with precursor powder.
2. Evacuation: the vacuum chamber is evacuated to reach a pressure of  $6 \times 10^{-6}$  mbar.
3. Prepare phase: the temperature of the source is increased until the prepare setpoint temperature is reached. Then it will soak, meaning the temperature stays at the setpoint for a certain time.
4. Idle phase: the temperature goes up again to the idle setpoint and do another soak.
5. Ramping phase: The source shutter of the heated source opens to monitor the rate. The temperature slowly increases to ramp up the rate. This continues until the rate is within the allowed margin of the target rate (defined as the capture) uninterruptedly for the duration of a certain time (defined as the capture time).
6. Deposition: The substrate shutter opens to expose the substrates and the deposition begins. The temperature is tweaked during the deposition to keep the deposition rate constant.
7. Turn off: When the target thickness is reached, the substrate shutter closes and the deposition is completed. The temperature of the source decreases. When it is below  $70^{\circ}\text{C}$ , the chamber can be vented and samples can be unloaded.

Operation parameters such as prepare setpoint and soak, idle setpoint and soak, capture and capture time, target rate and target thickness are all registered in the recipe for each source. Figure 3.4 displays the operational parameters within the thermal evaporation process.



**Figure 3.4:** A sketch of the prepare phase, idle phase, and ramping phase for thermal evaporation deposition.

### 3.1.2. Spin coating

The most widely used deposition method in the PVK field is a solution process called spin coating. Its popularity is due to ease of perovskite synthesis and low cost [83]. The film thickness and quality is optimized by controlling spin speed, spin time and spin acceleration [16], which differs for each material due to properties such as density, viscosity and surface tension.

To prepare for the spin-coating process, the precursor solution is prepared. This is done by weighing the solid precursor powder and add the amount of solvent needed for the desired concentration. The solution is placed in a vortex mixer to fully dissolve the precursor in the solvent. The spin-coating process, depicted in Figure 3.5, can be divided into four stages:

1. Deposition onto the substrate:

The precursor solution is deposited onto the substrate by pouring it out using a nozzle or spraying it on. Certain solutions require dispersion through a filter to remove any particles that could contaminate the film [6]. An excess amount of solution is applied on the substrate compared to the amount that is needed for the final film thickness to ensure the entire surface is wet. Otherwise, this could lead to the substrate not being fully coated by the end of the spin-coating [63].

2. Spin-up:

During this stage, the substrate is accelerating up to the desired rotation speed. While the substrate continues to moving faster, the top of the fluid layer exerts an inertia which causes spiral vortices. Ultimately, the fluid is thin enough and starts to co-rotate with the substrate [6].

3. Spin off:

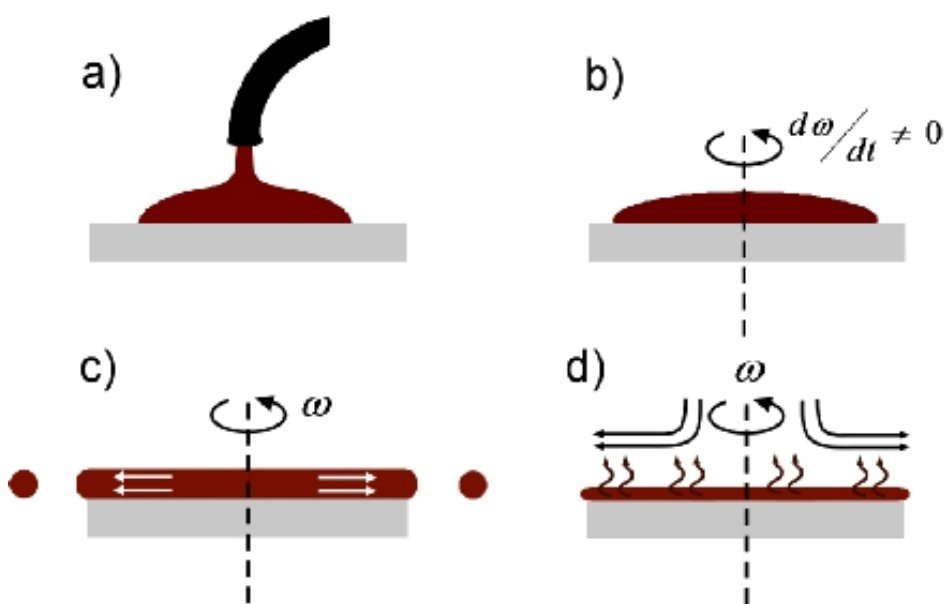
When the desired rotating speed is reached, the substrate rotates at a constant speed.

This results in gradual thinning of the fluid [200]. The edge of fluid starts to uniformly flow outward. Droplets formed at the edge are hurling off, which can cause difference in thickness at the outline of the substrate. However, this depends on properties and parameters such as surface tension, viscosity and rotational speed [6].

4. Evaporation:


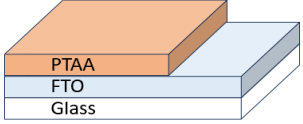
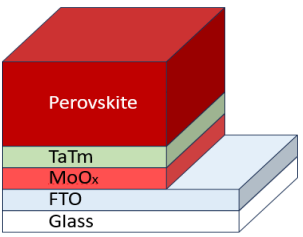
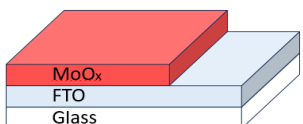
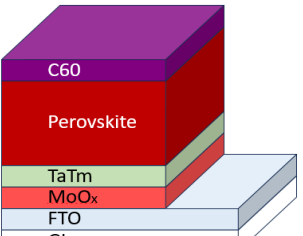
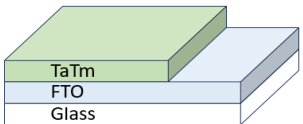
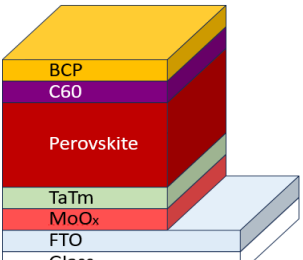
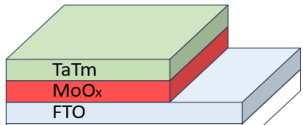
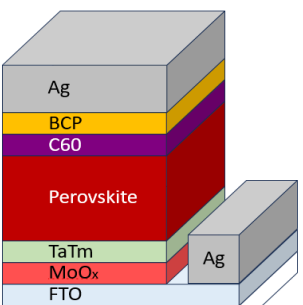
As the spin-off advances, the dominating behaviour shifts from gradual fluid thinning to solvent evaporation. This shift occurs when the fluid reaches a thickness where the viscosity effects results in only minor fluid flow. The evaporation of the solvent increases the viscosity of the remaining solution, which leads to the film to “gel” and stay in place [6][63].

The remainder of the solvent is evaporated during the post-annealing process [200].



**Figure 3.5:** The four stages of the spin-coating process with a) deposition stage b) spin-on stage c) spin-off stage d) evaporation stage [63].

## 3.2. Solar cell fabrication

Step 1			
	<p style="text-align: center;"><b>Cleaning:</b></p> <p>The solar cells were fabricated on 25x25 mm FTO covered corning glass. The substrates are cleaned for five minutes in acetone, followed by five minutes in isopropyl alcohol. After drying the substrates with a nitrogen gun, the substrates are ready for deposition.</p>		
Step 2a		Step 3	
	<p><b>PTAA:</b> 50 <math>\mu</math>L of 1.5 mg/ml PTAA (Sigma-Aldrich) in Chlorobenzene (Sigma-Aldrich, 99.8%) spincoated for 30 sec at 6000 rpm with an acceleration of 2000 rpm, then annealed at 100°C for 10 min.</p>		<p><b>Cs<sub>0.15</sub>FA<sub>0.85</sub>PbI<sub>2.85</sub>Br<sub>0.15</sub>:</b> Three rounds of single-cycle deposition of PbI<sub>2</sub>, FAI, CsBr &amp; PbCl<sub>2</sub> (Sigma-Aldrich, 99.9%), then annealed at 150°C for 20 min. (See Appx. B.3)</p>
Step 2b		Step 4	
	<p><b>MoO<sub>x</sub>:</b> The thermal evaporation of MoO<sub>3</sub> powder (Sigma-Aldrich, 99.97%) at 0.1 Å/s for a thickness of 2, 5, or 10 nm.</p>		<p><b>C60:</b> Thermal evaporation of C60 powder (Sigma-Aldrich, 98%) at 0.2 Å/s for a thickness of 25 nm.</p>
Step 2c		Step 5	
	<p><b>TaTm:</b> Thermal evaporation of TaTm powder (TCI, &gt;98%) at 0.1 Å/s for a thickness of 2, 5, or 10 nm.</p>		<p><b>BCP:</b> Thermal evaporation of BCP powder (Sigma-Aldrich, 96%) at 0.1 Å/s for a thickness of 8 nm.</p>
Step 2d		Step 6	
	<p><b>MoO<sub>x</sub> &amp; TaTm:</b> See Step 2b followed by Step 2c.</p>		<p><b>Silver:</b> Ag granulates (Umicore, 99.99%) are thermally evaporated at 0.3 Å/s for a thickness of 300 nm.</p>

### 3.3. Characterization techniques

#### 3.3.1. Spectral Ellipsometry

Spectral ellipsometry (SE) is an optical measurement technique that is used to determine the optical properties, thickness, and composition of films. Light is an electromagnetic wave that can be described by the vector of its electric-field intensity. The direction of the electric field of the wave can randomly fluctuate in time, which is defined as unpolarized light. Light is polarized when the direction of the light's electric field is well-defined [43]. The electric field of linearly polarized light is confined to a single plane along the direction of propagation, and can be divided in the parallel (p-) and perpendicular (s-) component. When the polarized light incides at an angle on a planar-layered sample, it experiences several interferences in the sample, which changes the amplitude and phase of the s- and p-components of the light. Spectral ellipsometry measure these changes in amplitude and phase. The ellipsometric parameters  $\psi$  and  $\Delta$  represent the change in amplitude and phase between the s- and p- component of the reflected light, respectively [100]. These parameters are indicated in Figure 3.6. Together, these are used to express complex reflection coefficients. The complex reflectance ratio forms the basis for the analysis of ellipsometry measurements [183]:

$$\rho = \frac{R_p}{R_s} = \tan(\psi) \cdot \exp(i \cdot \Delta) \quad (3.3)$$

The complex reflection coefficients can be expressed using the Fresnel coefficients for s- and p-polarized light at the interfaces ambient-film (0-1) and film-substrate (1-2) as indicated in Figure 3.7 [100][183]:

$$R_p = \frac{r_{01,p} + r_{12,p} \cdot \exp(-i \cdot 2 \cdot \theta)}{1 + r_{01,p} \cdot r_{12,p} \cdot \exp(-i \cdot 2 \cdot \theta)} \quad (3.4)$$

$$R_s = \frac{r_{01,s} + r_{12,s} \cdot \exp(-i \cdot 2 \cdot \theta)}{1 + r_{01,s} \cdot r_{12,s} \cdot \exp(-i \cdot 2 \cdot \theta)} \quad (3.5)$$

The following expressions for the Fresnel coefficients as a function of the complex optical constants of the ambient ( $N_0$ ), film ( $N_1$ ), and substrate ( $N_2$ ), illustrated in Figure 3.7, are derived from Snell's law [100]:

$$r_{01,p} = \frac{N_1 \cdot \cos(\varphi_0) - N_0 \cdot \cos(\varphi_1)}{N_1 \cdot \cos(\varphi_0) + N_0 \cdot \cos(\varphi_1)} \quad (3.6)$$

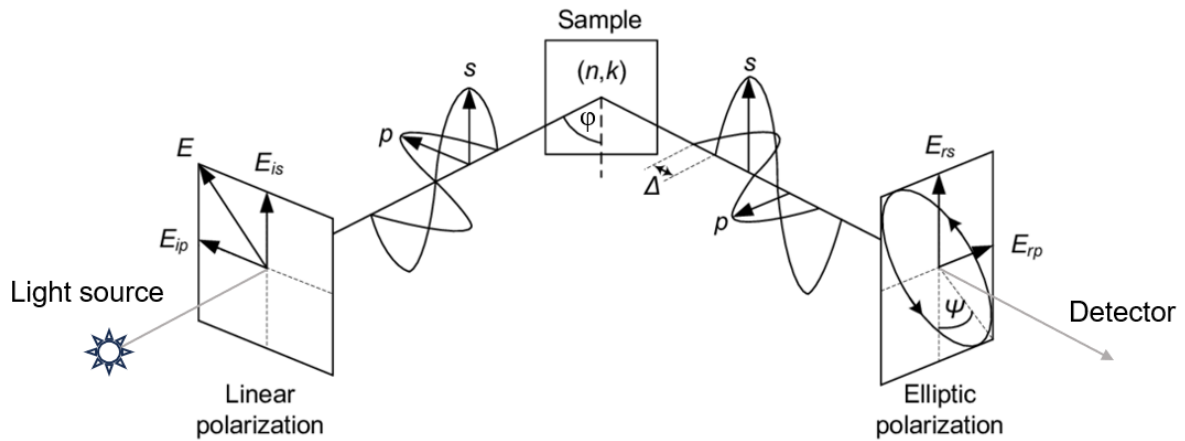
$$r_{01,s} = \frac{N_0 \cdot \cos(\varphi_0) - N_1 \cdot \cos(\varphi_1)}{N_0 \cdot \cos(\varphi_0) + N_1 \cdot \cos(\varphi_1)} \quad (3.7)$$

$$r_{12,p} = \frac{N_2 \cdot \cos(\varphi_1) - N_1 \cdot \cos(\varphi_2)}{N_2 \cdot \cos(\varphi_1) + N_1 \cdot \cos(\varphi_2)} \quad (3.8)$$

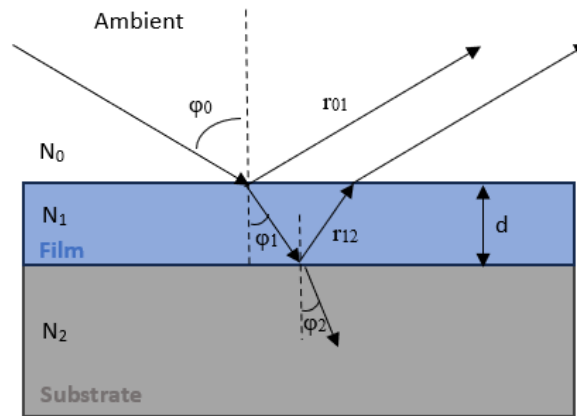
$$r_{12,s} = \frac{N_1 \cdot \cos(\varphi_1) - N_2 \cdot \cos(\varphi_2)}{N_1 \cdot \cos(\varphi_1) + N_2 \cdot \cos(\varphi_2)} \quad (3.9)$$

The phase difference between the boundaries of the film is expressed by the phase angle  $\theta$  [100][183]:

$$\theta = \frac{2 \cdot \pi \cdot d}{\lambda} \cdot N_1 \cdot \cos(\varphi_1) = \frac{2 \cdot \pi \cdot d}{\lambda} \cdot (N_1^2 - N_0^2 \cdot \sin^2(\varphi_0))^{1/2} \quad (3.10)$$

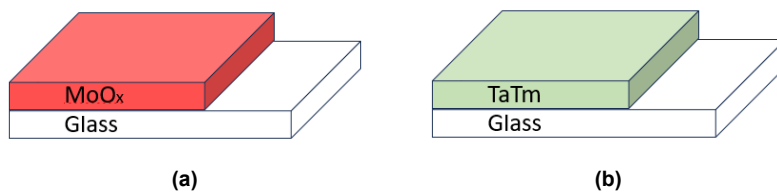


**Figure 3.6:** Schematic of the incoming and reflected light from a sample measured by the spectral ellipsometer [135].



**Figure 3.7:** Side profile of the reflection and transmission of light in the film.

The spectral ellipsometry measurements were carried out on the M – 2000 J. A. Woollam Co. inc. Spectroscopic Ellipsometer. It uses a tungsten halogen lamp as a light source. Before measurement, the lamp and the detector are aligned by following a calibration procedure. Then, different light angles of 55-60-65-70° were used for samples with a glass substrates and 60-65-70-75° for wafer samples, with an 10 second acquisition time for each angle. Samples with a glass substrate have magic tape on the backside to prevent back reflection. The samples fabricated for the spectral ellipsometry measurement are depicted in Figure 3.8.



**Figure 3.8:** Fabricated samples for spectral ellipsometry measurement



### 3.3.2. UV-Vis spectroscopy

UV-Vis spectroscopy is a non-destructive analytical technique that uses light in the ultraviolet and visible spectrum to measure the absorbance and transmittance of a sample at each wavelength. In photovoltaic devices, it is often used to determine the optical properties of materials.

In order for an electron in a material to excite to a higher energy state, it will need to absorb a certain amount of energy. The reduced intensity of the transmitted light through a material compared to the incoming light represent the absorbed energy, and is equal to the energy difference of the two energy levels that the electron moved between. The absorption of light varies for each wavelength, and is different for each material.

UV-Vis spectroscopy measures the transmittance by detecting the difference between the incident light ( $I_o$ ) on the sample and the transmitted light [167][180]:

$$T = I/I_o \quad (3.11)$$

Then the absorbance is defined as:

$$A = -\log(T) \quad (3.12)$$

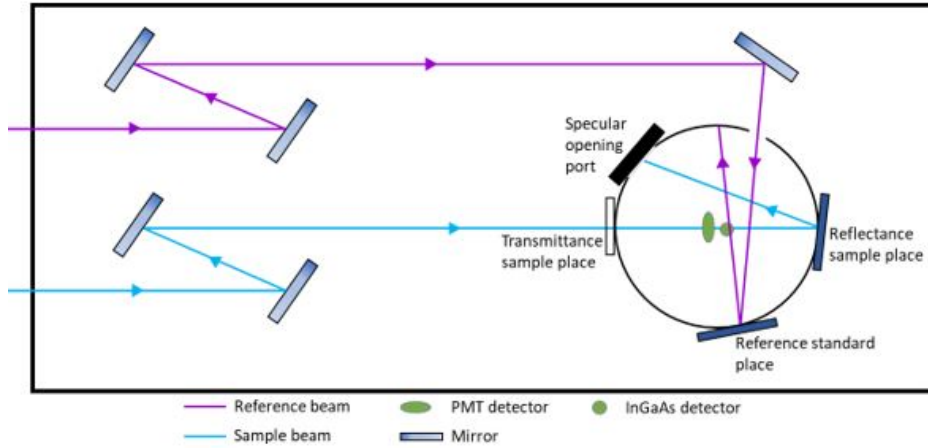
The PerkinElmer LAMBDA 1050 UV/Vis spectrophotometer has been used to measure the transmittance and absorbance spectrum. It consists of a number of components needed to measure these spectra:

- Light source: Two lamps are used for the UV and visible light source. The deuterium lamp provides for the UV light range and a tungsten lamp for the visible light range. The spectrometer has to switch light source during the measurement, which often happens between 300 and 350 nm. The light emission of both light sources is practically the same at this wavelength, allowing for a smoother transition [167][182][180].
- Monochromator: This component separates the light into a narrow band of wavelength, which is needed to probe the sample at each wavelength. The monochromator rotates its diffraction gratings to choose only a specific wavelength to leave the monochromator and incide on the sample [182][180].
- Detector: A photomultiplier tube (PMT) is used as the detector of the light in the UV and visible range. It converts the light from the sample beam into a readable signal and is compared to the reference beam in order to determine the spectrum [182][180].

The spectrophotometer has a 150-mm diameter integrating sphere at which the sample beam is targeted. Figure 3.9 shows that placing the sample in front of the integrating sphere measures the fraction of transmitted light ( $F_T$ ), while placing the sample at the back of the integrating sphere measures the fraction of reflected light ( $F_R$ ). Since light can only be transmitted ( $I_T$ ), reflected ( $I_R$ ), or absorbed ( $I_A$ ), the fraction of absorbed light ( $F_A$ ) can be calculated by measuring both the transmitted and reflected light and subtracting this from 1:

$$F_A + F_R + F_T = \frac{I_A + I_R + I_T}{I_o} = 1 \quad (3.13)$$

The absorbed light can also be measured by placing the sample inside the integrating sphere. The geometry and the Lambertian reflectance on the inside of the sphere captures the diffuse components of the reflectance.



**Figure 3.9:** Schematic of the UV-Vis spectrophotometer [42].

The measured absorbance can be used to determine the bandgap of semiconductors. This is done through Tauc's method. First, the measured absorbance ( $F_A$ ) as well as the film thickness ( $t$ ) is used to calculate the absorption coefficient ( $\alpha$ ) with the formula::

$$\alpha = \frac{2.302 \times A}{t} \quad (3.14)$$

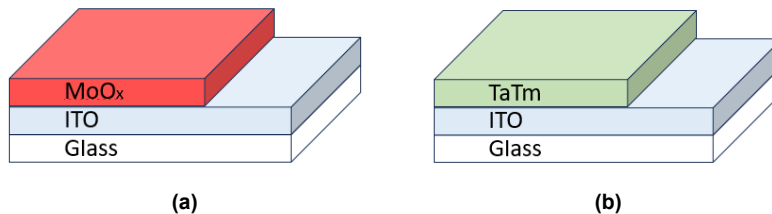
Then, the optical bandgap is estimated using the Tauc's relation:

$$\alpha h\nu = B(h\nu - E_g)^n \quad (3.15)$$

where  $\alpha$  is the absorption coefficient,  $h\nu$  is the photon energy,  $B$  is a constant,  $E_g$  is the optical bandgap and  $n$  is a parameter of the value 1/2, 2, 3/2, 3 for direct bandgap, indirect bandgap, direct forbidden bandgap and indirect forbidden bandgap, respectively. The photon energy  $h\nu$  is converted from the wavelength ( $\lambda$ ):

$$h\nu = \frac{1240}{\lambda} \quad (3.16)$$

The samples fabricated for the UV-Vis spectroscopy measurement are depicted in Figure 3.10. The samples consist of ITO coated glass substrates with 5-nm thick  $\text{MoO}_x$  or with 7-nm thick TaTm deposited on top. Data sheet information on the ITO can be found in Appendix B.2. All the samples with the  $\text{MoO}_x$  were deposited in one batch to have the samples as similar as possible. The same is applied for the TaTm deposition. After deposition, all the samples were annealed on a hotplate at different temperatures for different times.



**Figure 3.10:** Fabricated samples for UV-Vis spectroscopy measurement.

### 3.3.3. X-ray Photoelectron Spectroscopy

X-ray Photoelectron Spectroscopy (XPS) is a non-destructive surface-sensitive method that provides information on the atomic composition and chemical state of the elements in the material [125]. XPS can measure the number of electrons released at any value of binding energy. The binding energy is defined as the energy that it takes for a core electron to be emitted and is unique to each element. All elements except for hydrogen and helium can be detected, therefore being suitable for almost every material [173].

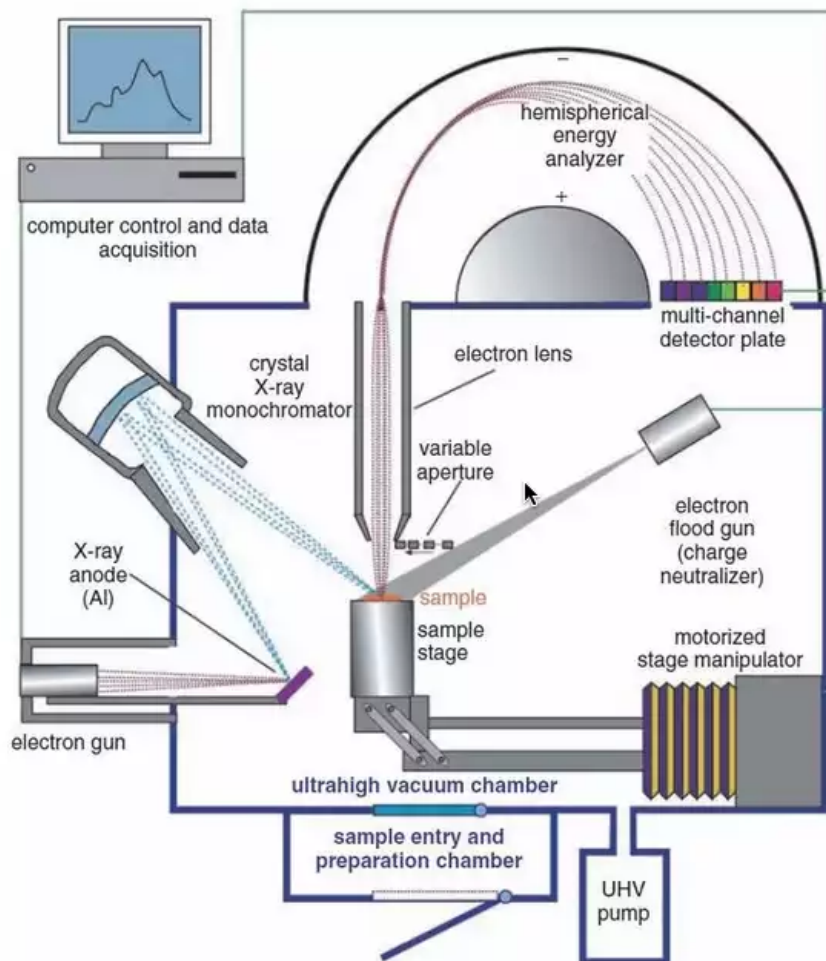
During XPS, the samples are exposed to an X-ray beam. The monochromatic photons excite the electrons in the samples and the emitted kinetic energy of the electrons returning to the ground state can be analyzed. The atoms present in the sample are determined with the equation [173][29][165][125]:

$$E_{binding} = E_{photon} - E_{kin} \quad (3.17)$$

Where  $E_{binding}$  is the binding energy,  $E_{photon}$  is the energy of the x-ray photons, and  $E_{kin}$  is the kinetic energy emitted by the electron. The photon energy and the work function of the spectrometer are known, while the kinetic energy of the electron is recorded by the detector. Therefore, the binding energy can be determined by solving Equation 3.17. By recording the number of electrons emitted for each binding energy, the composition of the sample is determined [29].

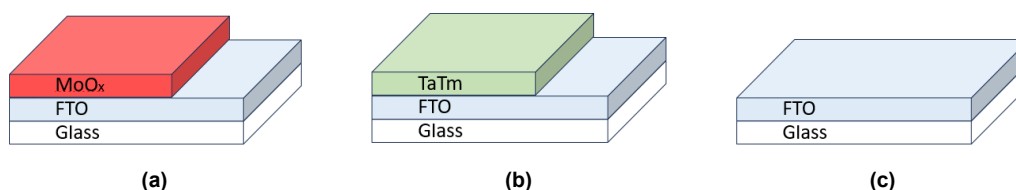
The spectrometer is housed within an ultra-high vacuum (UHV) environment. This is to prevent the emitted electrons from scattering off air molecules while moving from the sample to the analyzer. The vacuum also reduces surface contamination on the sample which could greatly affect the results [173][165]. The most important spectrometer components are shown in Figure 3.11 and described below:

- X-ray source: An heated tungsten filament is used to create a stream of electrons that are accelerated towards the high voltage x-ray anode. The energy of the x-ray source depends on the anode material, and must be strong enough to excite core-level electrons in all elements of the periodic table [165].
- Monochromator: The X-rays are directed towards the quartz crystal monochromator to diffract and filter out any unwanted x-ray lines, such as lower intensity lines and Bremsstrahlung radiation [173][125].
- Lenses: Extraction lenses are placed in between the sample and the analyzer to define the acceptance angle at which the emitted electrons from the sample are collected. The electron collecting efficiency is improved by using a larger acceptance angle. The extraction lenses are also able to reduce the energy of the electrons travelling to the analyzer in order to improve the energy resolution of the XPS [173][165].
- Analyzer: The concentric hemispherical analyzer consists of two hemispheres, where applied voltage on the outer hemisphere is more negative than on the inner hemisphere. Only electrons with a certain energy will be able to travel through the analyzer. Higher energy electrons will collide with the outer hemisphere and lower energy electrons will collide with the inner hemisphere. The energy of the electrons that are allowed to pass through the analyzer can be adjusted by changing the applied voltage [173]. Also, increasing the radius of the analyzer improves the energy resolution [165].
- Detector: A multichannel display detector is used to simultaneously detect the kinetic energy of the electrons [165].



**Figure 3.11:** Schematic of the XPS spectrometer [125].

The samples depicted in Figure 3.12 were used for the analysis of XPS. The samples are FTO coated glass substrates with different thicknesses of  $\text{MoO}_x$  or TaTm deposited on top. Data sheet information on the FTO can be found in Appendix B.2. As a reference, a bare FTO coated glass substrate was used.



**Figure 3.12:** Fabricated samples for XPS spectroscopy measurement.

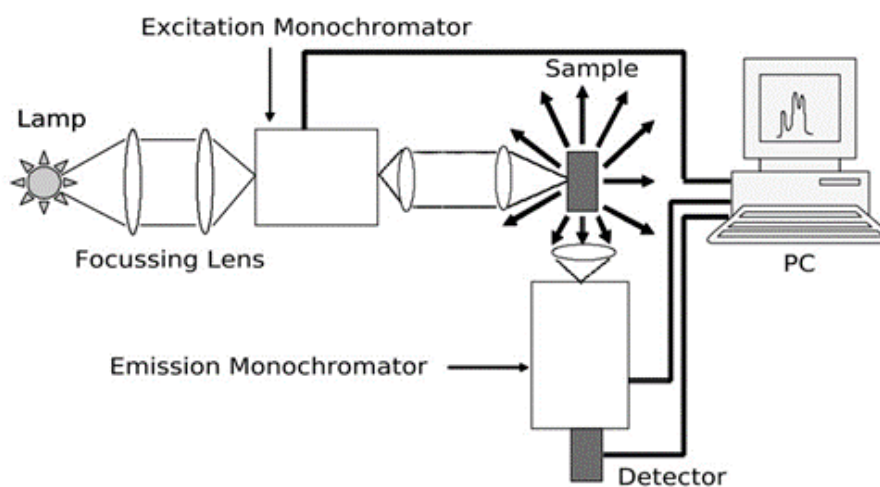
### 3.3.4. Photoluminescence spectroscopy

Photoluminescence (PL) spectroscopy is a non-destructive and contactless method that can help with the analysis the electronic structure and the presence of defects in semiconductor materials. The PL spectrum is obtained by directing light on the sample. This light is absorbed and excites electrons to higher energy states. When the electron relaxes and returns back to the lower energy state, it will release energy [3][172]. The released energy is con-

verted through non-radiative processes into heat or vibration, or through radiative processes into the emission of light [115]. The emission of light or luminescence through this process is photoluminescence (PL) and is detected by photoluminescence spectroscopy [3][65]. In semiconductors, the non-radiative relaxation occurs when an electron goes from an excited state in the CB to the lowest energy state in the CB. When the electron eventually goes from the CB to the VB, the lost energy is converted into a photon which is emitted from the material. Therefore, the peak of the PL signal represents the band gap energy [172].

In addition to the emission spectrum, the dynamics of the emission can be analysed. The radiative decay from the excited states to the ground state make up the emission process [115]. The average time that the electron stays in the excited state is interpreted as the emission lifetime. Different lifetimes and decay behaviour can have several causes, such as recombination from the CB to the VB or due to the presence of trap states [131]. The time-resolved PL can therefore provide additional insight on occurring phenomena.

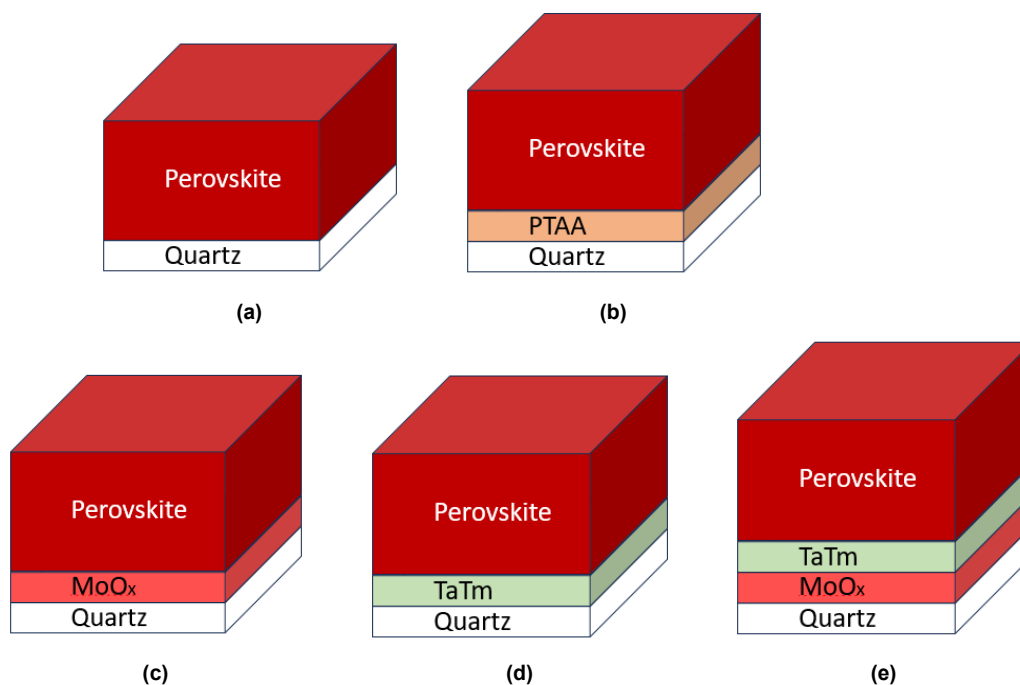
The Edinburgh Instruments FLS980 Photoluminescence spectrometer was used for the steady state PL spectra. Figure 3.13 shows an overview of the PL spectrometer. A 450 W xenon lamp is used to induce the excitation in the sample. The selected excitation wavelength is 405 nm, as this is the fixed excitation wavelength for the recording of the time-resolved PL. As the sample is excited, the emission monochromator selects a range of wavelengths of 600-850 nm to be allowed through to the PMT detector. This wavelength range was chosen as the selected emission wavelength of 780 falls in this range. The PMT detects the light in the UV and visible range and is before measurement cooled to  $-22^{\circ}\text{C}$ . The slit for both the excitation and the emission beam was set to 2.5 mm. A filter of 590 nm was placed between the sample and the monochromator. A step size 1 nm and a dwell time of 0.2 s were used for the recording of the PL spectra.



**Figure 3.13:** Schematic of the PL spectrometer [131].

For the time-resolved PL measurement, the Edinburgh Instruments LifeSpec-ps lifetime spectrometer was used. The excitation is induced by a picosecond pulsed diode laser. The excitation wavelength is fixed at 405 nm and the emission wavelength is set at 780 nm to keep the conditions the same as with the steady-state PL measurement. The width of the slits for both the excitation and emission beam was 2 mm with a filter of 590 nm placed between the sample and the monochromator. The time range was set at 500 ns with 512 channels, which resulted in 0.9766 ns per channel.

The samples fabricated for the PL measurements were quartz substrates with an HTL and perovskite film on top. Different HTLs were deposited to compare the effect. As a reference, a sample without HTL was used. The samples shown in the Figure 3.14 were fabricated by depositing the PVK film in a single run. This expedient reduces the run-to-run variability and allows for a consistent comparison of the HTL used.



**Figure 3.14:** Fabricated samples for PL spectroscopy measurement.

## Film level testing of $\text{MoO}_x$ and TaTm

Before any devices with  $\text{MoO}_x$  and TaTm can be fabricated, the  $\text{MoO}_x$  and TaTm need to be evaluated on certain fabrication aspects. First, the tooling factors have to be determined to be able to control the thickness of the fabricated films. The process of establishing the tooling factors is described in Section 4.1. Then, it is determined in Section 4.2 if  $\text{MoO}_x$  and TaTm are able to withstand annealing temperatures necessary to fabricate high quality perovskite.

### 4.1. Tooling factor determination for $\text{MoO}_x$ and TaTm

As discussed in Section 3.1.1, the film thickness is detected by a QCM positioned in the evaporation chamber. In order to fabricate films of a desired thickness, the tooling factor must be calculated. The tooling factor is the correction between the deposited thickness on the QCM and the deposited thickness on the substrate [26]. By knowing the QCM detected film thickness and measuring the actual film thickness on a substrate, the tooling factor can be determined.

#### $\text{MoO}_x$

To determine the tooling factor for  $\text{MoO}_x$ , 30 nm of  $\text{MoO}_x$  based on the QCM reading was deposited on a glass substrate and the thickness was measured using spectral ellipsometry. However, the spectral ellipsometer was not able to detect a film thickness. There were a variety of causes investigated:

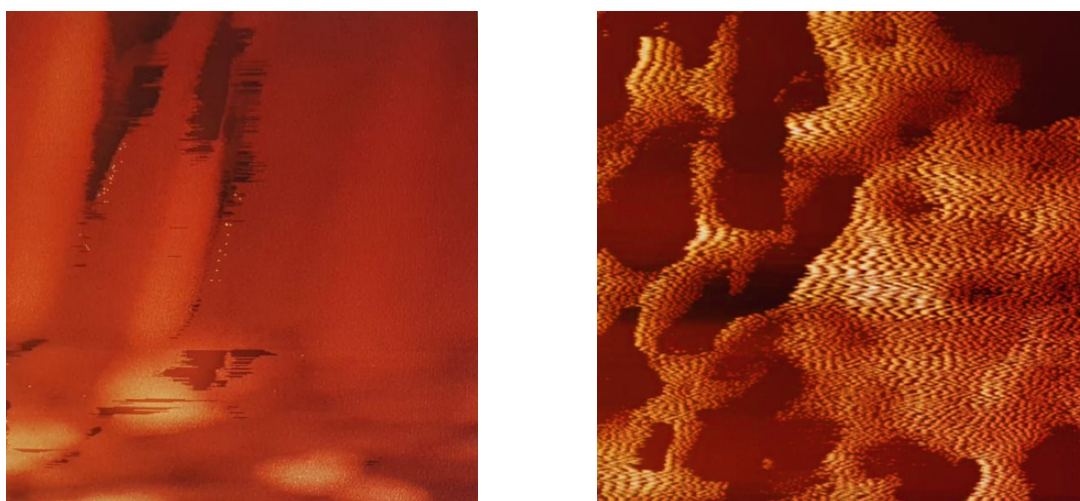
- No deposition was executed: It was suspected that the deposition had been aborted since the spectral ellipsometer measured a film thickness of less than 1 nm. There was also no change in color and reflectance visible of the sample by eye, unlike with the TaTm sample. Another 30-nm  $\text{MoO}_x$  deposition was done and frequently checked to observe the entire deposition took place. However, the measured thickness with the spectral ellipsometer was still less than 1 nm.
- Wrong material density: A 150-nm deposition of  $\text{MoO}_x$  based on the QCM reading was done to see how the thickness measurement would change. After the deposition, there was a grey color on the sample which was another confirmation that there was  $\text{MoO}_x$  deposited. The spectral ellipsometer showed another layer thickness below 1 nm. It was thought that the material density in the recipe could have been wrong, which would have caused the QCM to detect a deposited layer thickness much thicker than the actual deposited thickness. However, the density of  $\text{MoO}_x$  indicated in the product information as well as on different online sources was the same as the material density registered in the recipe.
- Optical properties of  $\text{MoO}_x$  too similar to glass:  $\text{MoO}_x$  has previously been used for silicon solar cells, where spectral ellipsometry was able to measure  $\text{MoO}_x$  film thickness [122]. Just observing by eye, a thin layer of  $\text{MoO}_x$  is visible on a silicon wafer but not on

a glass substrate. It was therefore suggested that the optical properties of the MoO<sub>x</sub> are too similar to the glass for the the spectral ellipsometer to be able to detect a difference in the glass and the MoO<sub>x</sub>.

To determine the tooling factor, 30 nm of MoO<sub>x</sub> based on the QCM reading was deposited on a silicon wafer. A previously used model for MoO<sub>x</sub> was used with the spectral ellipsometer, resulting in an average thickness 7.16 nm from 5 measurements. Thus, the calculated tooling factor for MoO<sub>x</sub> is 4.19.

#### TaTm

To determine the tooling factor for TaTm, 30 nm of TaTm based on the QCM reading was deposited on a glass substrate and the thickness was measured using spectral ellipsometry. TaTm is a relatively new material and a spectral ellipsometer model for TaTm is not available. Therefore, a model for another organic material, Spiro-TTB, was used. The spectral ellipsometer measured thicknesses between 6.98 nm and 16.33 nm, which is too wide of a range to accurately determine the tooling factor. It was suspected that a nonuniform distribution of TaTm led to this wide range of measured thicknesses. To confirm this, a measurement using Atomic Force Microscopy (AFM) was done. Figure 4.1 shows the AFM images of MoO<sub>x</sub> and TaTm on glass substrates. It can clearly be seen that MoO<sub>x</sub> is a rather uniform layer, while the TaTm forms islands on the glass. This, the images confirm that the TaTm layer is nonuniform across the substrates. This irregular morphology might be explained by adhesion forces that are stronger among the TaTm atoms than the adhesion forces between the TaTm and the glass substrate. To get a more uniform layer, TaTm was deposited on a silicon wafer. The thickness measurements with the spectral ellipsometer on this sample were much more precise, and resulted in a tooling factor of 1.83. However, as mentioned earlier, the measurement was done with an spectral ellipsometer model developed for Spiro-TTB. Although this measurement gave an indication of the actual film thickness, another measurement method would be needed to confirm the thickness.



**Figure 4.1:** AFM images of MoO<sub>x</sub> (left) and TaTm (right) on glass substrate.

Other publications creating PSCs with TaTm have used a mechanical profilometer to measure the film thickness of TaTm [11][204][141][12][205]. The profilometer can accurately measure film thicknesses above 50 nm. Therefore, the sample created for this measurement was a 200-nm deposition of TaTm (based on the QCM reading) on a silicon wafer. Unfortunately, the profilometer at our disposal was not able to use a contact force low enough to measure



the thickness of organic films. Instead of the stylus moving across the surface, the stylus was sliding through the TaTm due to the softness of the TaTm.

Another method to measure the film thickness is Scanning Electron Microscopy (SEM). A scratch was created on the same sample, causing the edges of the film along the scratch to curl upwards. This exposes the cross section of the film, which is measured to determine the film thickness. Figure 4.2 shows the SEM image of the scratch and of an up-curling edge in the scratch. The average thickness measured was 111.11 nm from 12 measurements, resulting in a tooling factor of 1.80. This tooling factor is very similar to the tooling factor of 1.83 determined with the spectral ellipsometer.

It is important to note that determining the thickness in this way is not the most accurate, since it is hard to say if the face of the edge is truly perpendicular to the microscope. If the edge is measured under an angle, the measured film thickness is smaller than the actual film thickness. Furthermore, it is also debatable whether the edge of the film truly curls upward, or if the edge is accumulated material caused by the scratch.

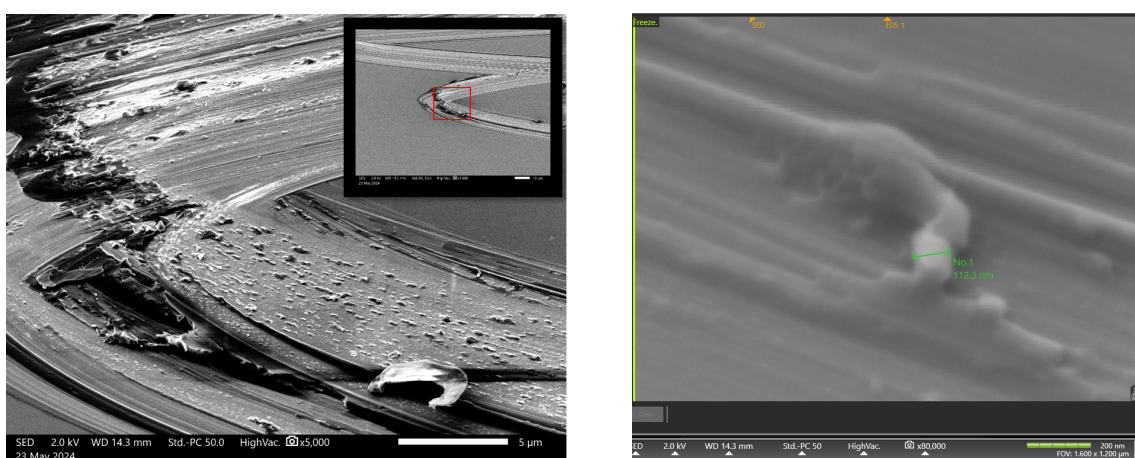


Figure 4.2: SEM images of the scratch in the TaTm film on wafer.

### Summary

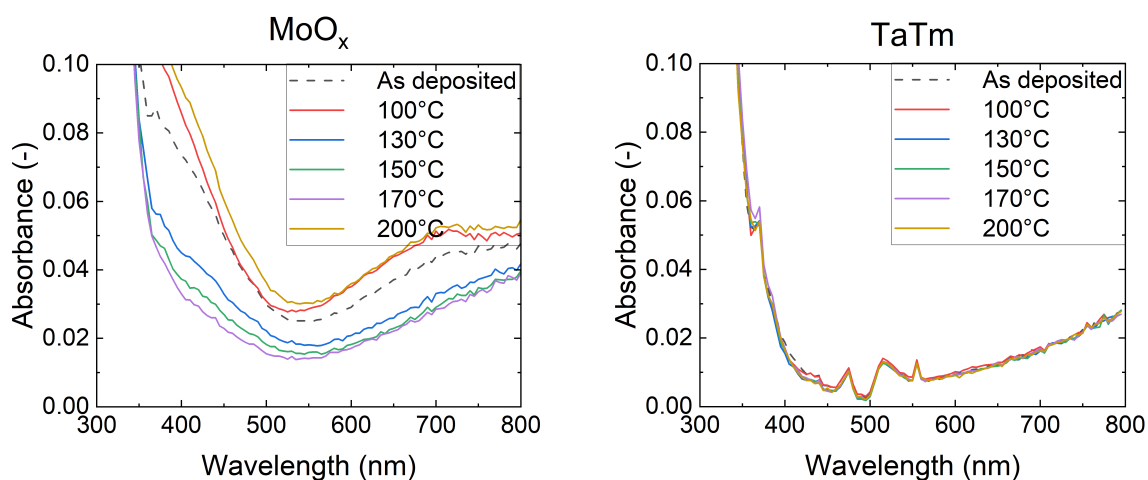
- The film thickness of MoO<sub>x</sub> on a glass substrate cannot be measured using spectral ellipsometry as the optical properties of MoO<sub>x</sub> is too similar to glass.
- The tooling factor for MoO<sub>x</sub> was determined to be 4.19.
- TaTm forms islands when deposited on glass and ITO coated glass, leading to nonuniform films.
- The tooling factor for TaTm was determined to be 1.80.

## 4.2. Thermal stability of optical and electrical properties of MoO<sub>x</sub> and TaTm

In order to know if MoO<sub>x</sub> and TaTm are able to withstand annealing temperatures necessary to fabricate high quality perovskite, the optical properties are measured for different annealing conditions. The reference device that uses PTAA has an optimal annealing temperature of 150°C for 20 minutes. To test effect of conditions surrounding this value, MoO<sub>x</sub> and TaTm were annealed at temperatures between 100°C-200°C for 10, 20 and 30 minutes.

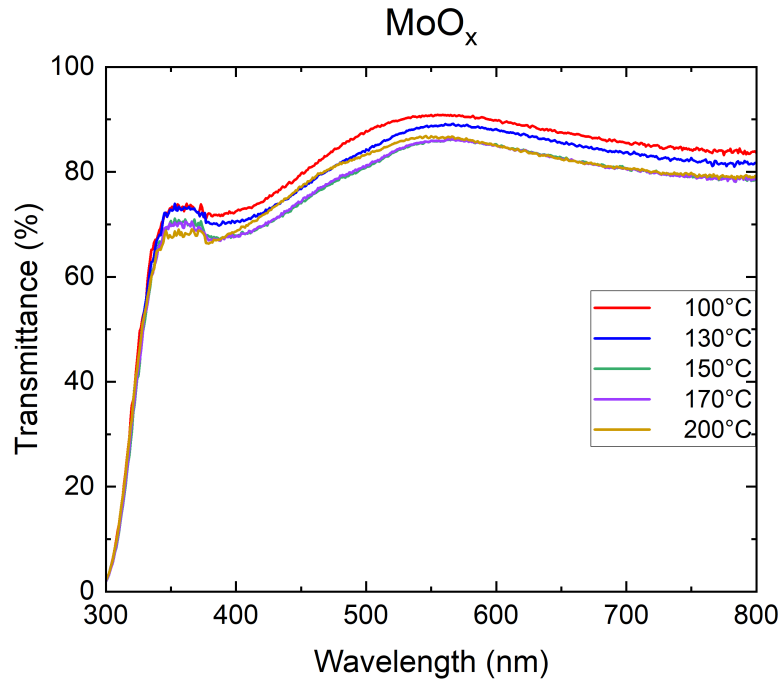
### Optical properties

The absorbance is measured to test if the HTLs degrade at higher temperatures or longer annealing times. It has been shown in multiple studies that thermal degradation changes the absorbance spectrum of the material [122][2]. Figure 4.3 shows the absorbance spectra for MoO<sub>x</sub> and TaTm after annealing for 30 minutes at temperatures between 100°C and 200°C. The absorbance spectra for the other annealing times can be found in Appendix C.1. For the MoO<sub>x</sub>, there is no clear relation between the annealing temperature and absorbance. However, the change in absorbance is very small, which suggests that these changes are negligible. Other studies have shown that the absorbance would increase with annealing temperature due to the increase in oxygen vacancies [121][160][104][95][127]. The absorbance spectra for TaTm clearly remains unchanged for different annealing temperatures (see Figure 4.3 right). It was therefore concluded that both MoO<sub>x</sub> and TaTm are optically stable for the tested annealing conditions.



**Figure 4.3:** Absorbance of MoO<sub>x</sub> and TaTm annealed at temperatures from 100°C to 200°C for 30 minutes

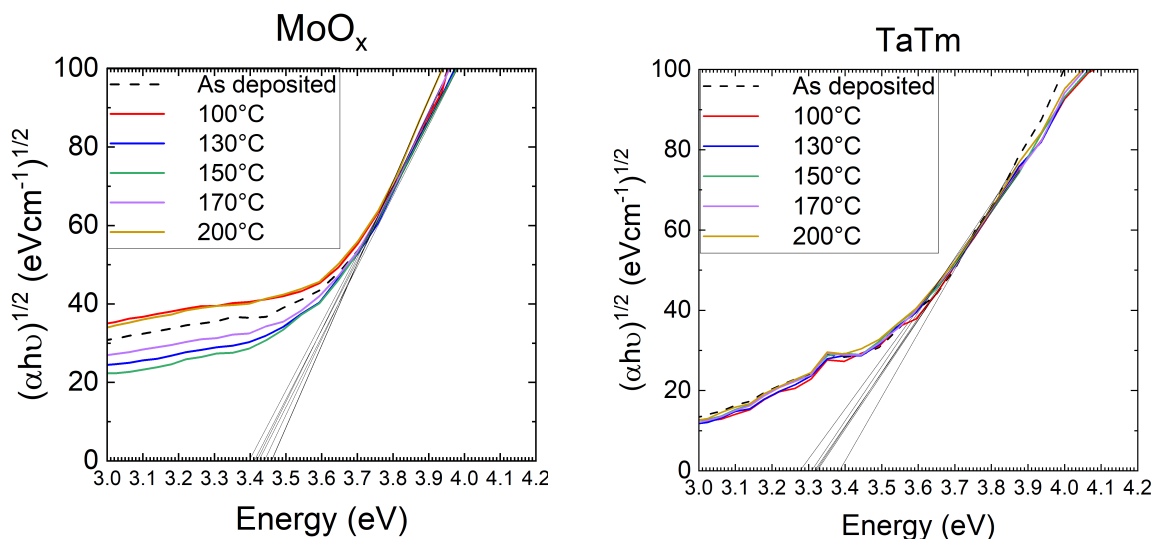
Figure 4.4 shows the transmittance spectrum for MoO<sub>x</sub> after annealing for 20 minutes at temperatures between 100°C and 200°C. The transmittance spectra for the other annealing times can be found in Appendix C.2. The transmittance is above 80% for wavelengths larger than 500 nm. The high transmittance of MoO<sub>x</sub> is beneficial for devices as it allows for light absorption by the perovskite. It can be seen that the transmittance of MoO<sub>x</sub> decreases when annealed from 100°C to 150°C. This is in agreement with literature, which a decrease in transmittance with increasing annealing temperature related to the increase in oxygen vacancies [104][62][58]. Our results show no further decrease in transmittance for the higher annealing temperatures from 150°C to 200°C, which could indicate a stabilization in the number of oxygen vacancies. However, in literature the transmittance of MoO<sub>x</sub> continues to decrease for higher annealing temperatures.



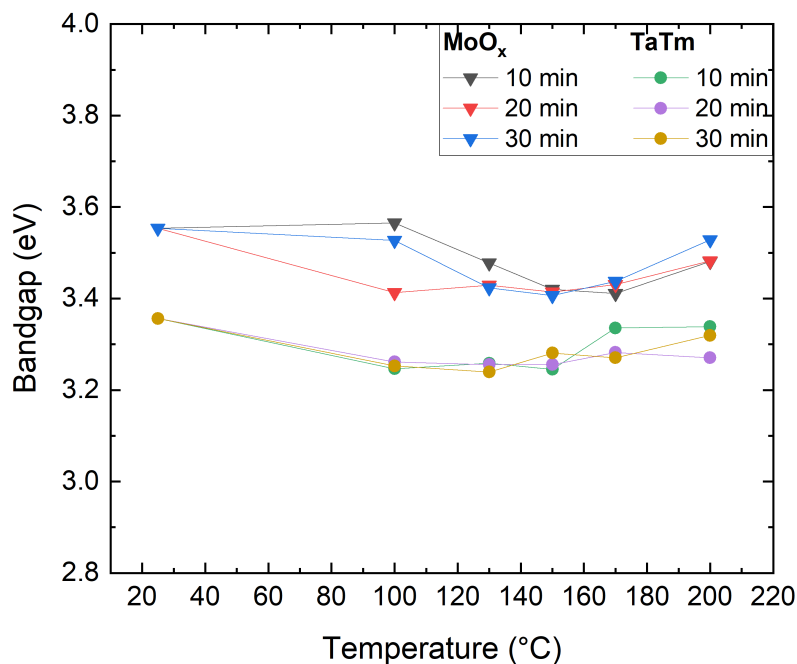
**Figure 4.4:** Transmittance of MoO<sub>x</sub> annealed at temperatures from 100°C to 200°C for 20 minutes

#### Bandgap estimation using the Tauc plot

The bandgap of the MoO<sub>x</sub> and TaTm annealed at different conditions can be estimated using the Tauc plot. The Tauc plot is created by using the absorbance from Figure 4.3 to calculate the absorption coefficient  $\alpha$ . The Tauc plot is obtained by plotting the  $(\alpha h\nu)^{1/2}$  as a function of the photon energy  $h\nu$ . The formulas to calculate the absorption coefficient and the photon energy can be found in Section 3.3.2. The leading edge of the spectra has a linear part in the slope. By extrapolating the linear part to the baseline, the bandgap is estimated [209]. The extrapolation in the Tauc plot is depicted in Figure 4.5 for the samples annealed at temperatures from 100°C to 200°C for 20 minutes. Figure 4.6 summarizes the estimated bandgap of MoO<sub>x</sub> and TaTm after annealing at temperatures between 100° and 200°C for 10, 20, and 30 minutes. The graphs show little change in the bandgap for the different annealing conditions. With the errors from the UV-Vis measurement and the error from the bandgap estimation using the Tauc plot, the change in bandgap is considered insignificant. This is in disagreement with literature, where the bandgap decreases for higher annealing temperature due to the increase in oxygen vacancies [62][58].



**Figure 4.5:** Tauc plot for MoO<sub>x</sub> and TaTm annealed at temperatures from 100°C to 200°C for 20 minutes

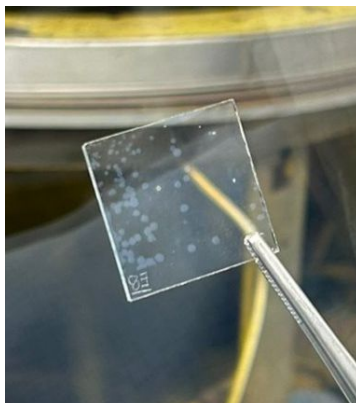


**Figure 4.6:** Estimated bandgap of MoO<sub>x</sub> and TaTm after annealing at temperatures between 100°C and 200°C for 10, 20, and 30 minutes.

#### Degradation of TaTm

For device preparation, substrates with MoO<sub>x</sub> and TaTm deposited on top were annealed for the same abovementioned annealing conditions. After annealing, white opaque spots appeared on certain samples with TaTm, as is shown in Figure 4.7. The samples on which the white spots appeared were for the annealing conditions 170°C for 30 minutes, and 200°C for 10, 20, and 30 minutes. The appearance of the white spots at higher temperatures and longer annealing times suggest that the TaTm has degraded. It remains unclear why the TaTm degraded in the second batch, but not in the first batch. However, annealing of samples at 150°C

for 20 minutes was done for the following batches of device preparation. TaTm showed no degradation at this annealing condition in both the first and second batch, so the results of the devices should not be comprised.



**Figure 4.7:** Degradation showing as white spots in the TaTm film after annealing at 200°C for 20 minutes.

### Summary

- The transmittance of MoO<sub>x</sub> decreased for lower temperatures, indicating an increase in oxygen vacancies. No change in transmittance is detected for temperatures above 150°C, suggesting that the number of oxygen vacancies stabilized.
- The absorbance spectra for MoO<sub>x</sub> showed no significant change with increasing temperature and annealing time, suggesting that no degradation occurred.
- No indication of degradation in the TaTm was initially found based on the samples for absorbance measurement. Other samples (fabricated for device preparation) showed degradation through the appearance of white spots on the TaTm after annealing at 170°C for 30 minutes and at 200°C for 10, 20, and 30 minutes.
- There was no significant change in estimated bandgap of both MoO<sub>x</sub> and TaTm after annealing at various conditions.

# 5

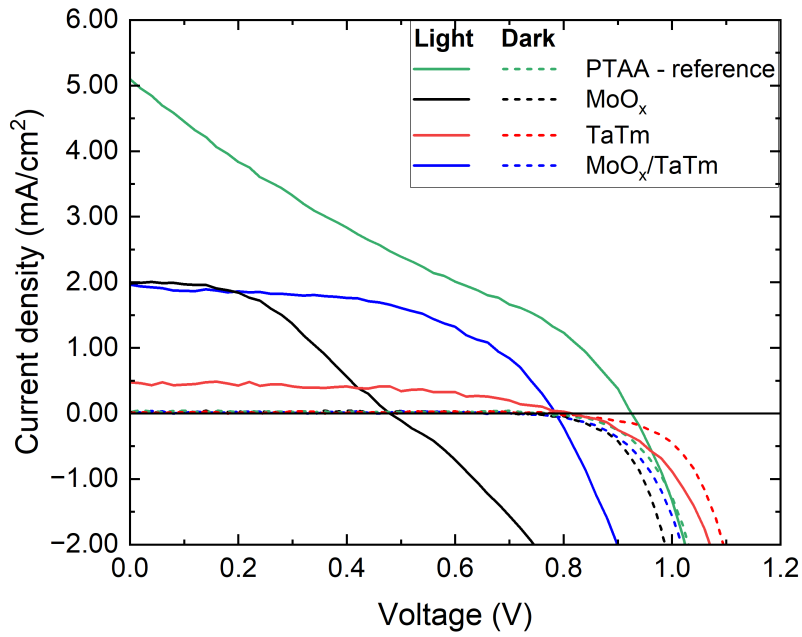
## Evaluation of charge carrier extraction at the HTL interfaces

Hole transport layers are a crucial component in PSCs. However, the interface can introduce additional recombination pathways which can negatively affect the  $V_{oc}$  of the cell. In Section 5.1, the effect of the HTM on the device parameters is discussed. The focus shifts to the HTL/PVK interface in Section 3.3.4 by measuring the photoluminescence yield of the HTL/PVK heterojunction and assess the non-radiative interfacial recombination.

### 5.1. Effect of hole transport material on device performance

The J-V curves for devices with  $\text{MoO}_x$ , TaTm,  $\text{MoO}_x/\text{TaTm}$  as HTL are compared to each other. First, we look into the use of  $\text{MoO}_x$  and TaTm as single HTL to seek understanding on their assets and limitations. Then, we explore the benefits of using  $\text{MoO}_x$  and TaTm together and the function of each HTL when used as double HTL. The devices are also compared to the established reference cell that uses PTAA as HTL, in order to identify the potential of  $\text{MoO}_x$  and/or TaTm replacing PTAA.

Devices with different hole transport materials were fabricated according to the flowchart in Section 3.2. Figure 5.1 shows the illuminate and dark J-V curve for these devices. The rectangular shape of the dark J-V curves indicates diode curves proper of solar cells and is observed for all four devices.



**Figure 5.1:** Dark and illuminate J-V curves of solar cells with PTAA, MoO<sub>x</sub>, TaTm, and MoO<sub>x</sub>/TaTm as HTL.

### PTAA

The illuminate J-V curve for PTAA is characterized by a strong S-shape. The S-shaped J-V curve is indicative of charge transport bottleneck. The reduced charge transport is most likely also responsible for low  $J_{sc}$  of 5.0 mA/cm<sup>2</sup>, since devices with PTAA from previous experiments have shown a current density above 20 mA/cm<sup>2</sup>.

### MoO<sub>x</sub>

The J-V curve for MoO<sub>x</sub> solar cell in Figure 5.1 demonstrates a poor  $V_{oc}$  of 0.496 V. As the poor  $V_{oc}$  is only detected in this device, we can infer that the MoO<sub>x</sub>/PVK interface is responsible for high interfacial recombination. It has been reported by multiple studies that the MoO<sub>3</sub> reduces to MoO<sub>2</sub> when the MoO<sub>3</sub> is direct contact with the perovskite MAPbI<sub>3</sub> [159][112][5]. MoO<sub>2</sub> is a metal and has a lower work function than MoO<sub>3</sub> [54]. The reduction of MoO<sub>3</sub> also affects the PVK. The Mo<sup>6+</sup> → Mo<sup>4+</sup> reduction takes place when the MoO<sub>3</sub> reduces to MoO<sub>2</sub> and oxygen is released. At the same time, the Pb<sup>2+</sup> → Pb<sup>4+</sup> oxidation and 2I<sup>-</sup> → I<sub>2</sub> oxidation occur, where iodine is released. Liu et al. found that the chemical reaction happening at the interface resulted in unfavourable energy level alignment unsuitable for hole extraction [112]. A potential barrier for hole extraction from the PVK to the MoO<sub>x</sub> due to the offset of the VB was too large for the holes to overcome. Further, a small potential barrier for electron extraction due to CB offset was too small to suppress electron extraction from the PVK to the MoO<sub>x</sub>. Similarly, Olthof and Meerholz reported an electron transfer from the PVK to the MoO<sub>x</sub> and a high hole extraction barrier, resulting in the limited  $V_{oc}$  [136].

### TaTm

The J-V curve for TaTm shows a  $V_{oc}$  almost twice the magnitude of MoO<sub>x</sub>. However, the  $J_{sc}$  is significantly lower. The reduced slope of the J-V curve around the  $V_{oc}$  is representative of a high series resistance. As the low  $J_{sc}$  and high series resistance are only detected in this device, it is predicted that the FTO/TaTm interface is responsible. Avila et al. conducted a study

in which a comparison was made between a PSC with and without the insertion of F<sub>6</sub>-TCNNQ between the ITO and TaTm [11]. The low FF and S-shaped J-V curve for the device without F<sub>6</sub>-TCNNQ indicate issues with charge extraction at the ITO/TaTm interface. They found an increased FF and rectangular shape of the J-V curve for the device with the F<sub>6</sub>-TCNNQ interlayer indicates an alleviation of the charge extraction barrier. Similarly, Du et al. found that an insertion of PEDOT:PSS or P3HT between the electrode and TaTm reduces the series resistance and increases the FF [41]. The hole extraction barrier at the FTO/TaTm is therefore suspected to be caused by a mismatch of energy levels. For the MoO<sub>x</sub>, the interfacial recombination at the MoO<sub>x</sub>/PVK interface resulted in a reduced V<sub>oc</sub>. For the TaTm, smaller V<sub>oc</sub> losses are observed since the majority carriers (holes) are transported from PVK to TaTm and can only recombine with minority carriers (electrons). However, since the the FTO/TaTm still hinders efficient collection at the front contact, a large series resistance is observed [13].

### MoO<sub>x</sub>/TaTm

The J-V curve for MoO<sub>x</sub>/TaTm shows a V<sub>oc</sub> similar to that of TaTm and a J<sub>sc</sub> similar to that of MoO<sub>x</sub>. This shows that combining the two HTLs results in the advantageous properties when compared to the solar cells with a single HTL.

As mentioned in the previous section, the MoO<sub>x</sub>/PVK interface is problematic mainly due to two reasons. First, a chemical reaction occurs at the interface that affects both the MoO<sub>x</sub> and PVK. Second, an electron transfer from the PVK to the MoO<sub>x</sub> takes place as a result of a low electron extraction barrier. The presence of TaTm in between the MoO<sub>x</sub> and PVK alleviates these two issues. TaTm prevents the chemical reaction by inhibiting contact between the MoO<sub>x</sub> and PVK. TaTm also acts as an electron blocking layer and hinders electrons from transferring from the PVK to the MoO<sub>x</sub>, as is reported in literature [142].

The other way around, the FTO/TaTm suffers from a hole extraction barrier that prevents the collection of holes at the front contact. The insertion of MoO<sub>x</sub> between the FTO and TaTm alleviates the hole injection barrier by improving the band energy alignment.

It must be noted that the slight decrease in V<sub>oc</sub> of MoO<sub>x</sub>/TaTm compared to TaTm could hint at a hole extraction barrier at the MoO<sub>x</sub>/TaTm. This would explain the series resistance in the J-V curve.

It must be noted that all the devices exhibit a PCE below 1% and a J<sub>sc</sub> below 5.00 mA/cm<sup>2</sup>. The reference cell using PTAA has previously shown to consistently achieve a PCE above 10% and a J<sub>sc</sub> above 20 mA/cm<sup>2</sup>. Since all the cells suffer from low PCE and J<sub>sc</sub>, an issue with either the PVK or ETL is assumed, considering all devices were in the same batch for the deposition of these layers. From other experiments ran simultaneously in the lab, it is suspected that the issue is with the ETL.

### Summary

- The PSC with MoO<sub>x</sub> as HTL demonstrated a low V<sub>oc</sub>. A chemical reaction occurs at the MoO<sub>x</sub>/PVK interface which results in unfavourable energy level alignment that allows electron extraction.
- The PSC with TaTm as HTL demonstrates a large series resistance as a result of a hole barrier at the FTO/TaTm interface. The hole injection barrier is caused by a mismatch of energy levels.
- For the double HTL, TaTm acts as an electron blocking layer and passivation layer for the MoO<sub>x</sub> interface, whereas MoO<sub>x</sub> improves the energy band alignment between the FTO and TaTm.

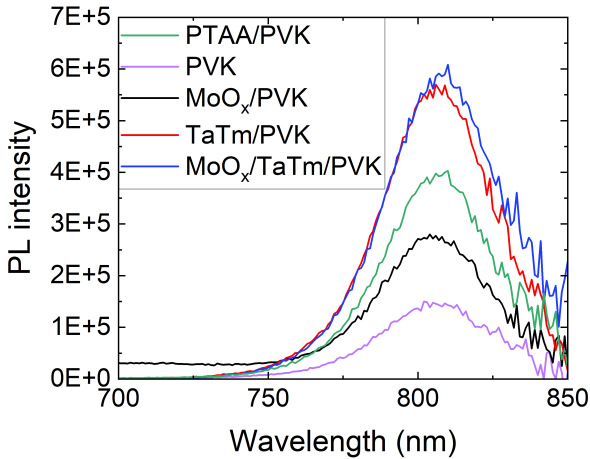


- The PSC with PTAA demonstrates higher  $V_{oc}$  and  $J_{sc}$  than the PSCs with  $MoO_x$  and/or TaTm.

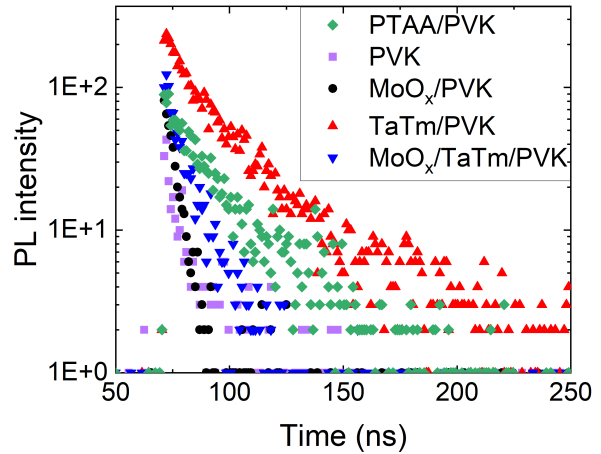
## 5.2. Hole extraction at the HTL/PVK interface for different hole transport materials

Based on the findings in Section 5.1, we focus our investigation on the HTL/PVK interface. The photoluminescence yield of each HTL/PVK heterojunction is measured to assess the non-radiative interfacial recombination at this interface. The results are also used to confirm some of the characteristics of the HTLs discussed in Section 5.1 and to seek a connection between the interfacial recombination and the device parameters.

The samples for PL measurement are HTL/PVK stacks deposited on quartz substrates. Quartz substrates were chosen instead of FTO-covered glass substrates to only create charge carrier transfer between the HTL and PVK. Additional charge carrier transport between the FTO and HTL would influence the result and make it harder to interpret. A schematic of the samples is shown in Figure 3.14 in Section 3.3.4. The thickness of the hole transport layers for these samples is the same as for the devices discussed in Section 5.1.



**Figure 5.2:** Steady state PL of PVK deposited on top of quartz, PTAA,  $MoO_x$ , TaTm, and  $MoO_x$ /TaTm.



**Figure 5.3:** Time-resolved PL of PVK deposited on top of quartz, PTAA,  $MoO_x$ , TaTm, and  $MoO_x$ /TaTm.

The photoluminescence (PL) originates from the radiative recombination process when the electron relaxes and goes from the CB to the VB, resulting in the emission of light/luminescence. Figure 5.2 represents the steady-state PL, and shows the intensity of the emitted luminescence as a function of the different wavelengths of the emitted luminescence. The peak intensity for all stacks is at a wavelength of 807 nm. A low peak intensity indicates low hole extraction. The lowest peak intensity is found for pristine PVK, followed by  $MoO_x$ /PVK and PTAA/PVK. The highest peak intensities is detected for TaTm/PVK and  $MoO_x$ /TaTm/PVK stacks.

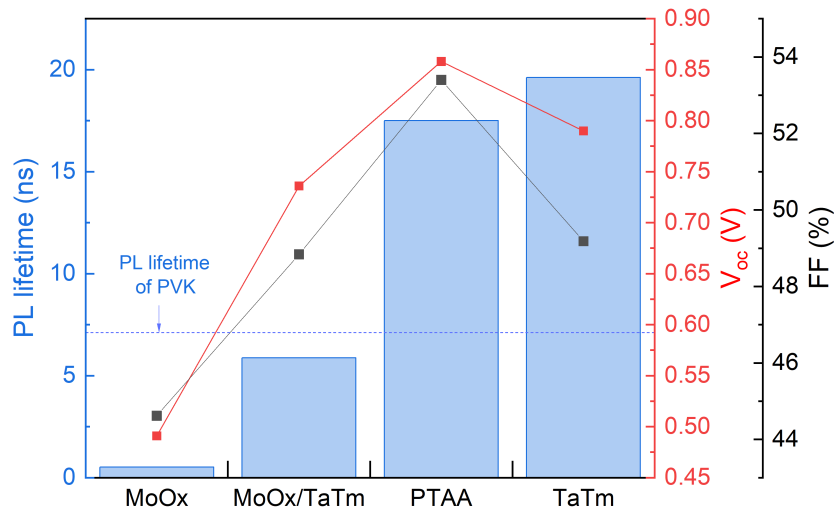
Figure 5.3 depicts the time-resolved PL, which represents the intensity of the emitted luminescence over time. The intensity decreases over time and is also referred to as the PL decay. The decay is caused by the excitation of many electrons to the CB at once, which over time fall back to the VB and recombine. When all excited electrons have returned to the VB, no PL intensity can be detected. A fast decay indicates low hole extraction. The fastest decay is

found for the pristine PVK and  $\text{MoO}_x$ , followed by the  $\text{MoO}_x/\text{TaTm}/\text{PVK}$  and  $\text{PTAA}/\text{PVK}$ . The slowest decay is detected for the  $\text{TaTm}/\text{PVK}$ .

When comparing the different HTLs, it can be seen that TaTm has a high PL peak intensity and the slowest PL decay. This means that a small amount of non-radiative recombination takes place at the TaTm/PVK interface compared to other HTL/PVK interfaces. Based on the findings in Section 5.1, the PL results confirm that the TaTm is effectively blocking the electrons due to favourable energy band alignment, as was discussed in Section 5.1. It could also suggest that there is a low number of defects at the interface due to TaTm functioning as a passivation layer.

Contrary to TaTm, a low PL intensity peak and a fast PL decay is found for  $\text{MoO}_x$ . In Section 5.1, it was discussed that  $\text{MoO}_x/\text{PVK}$  interface has a low electron extraction barrier. The low PL intensity peak could confirm the electron transfer from the PVK to the HTL due to poor energy band alignment. Additionally, a large number of defects at the  $\text{MoO}_x/\text{PVK}$  interface will further enhance the non-radiative recombination rate.

By inserting the TaTm between the  $\text{MoO}_x$  and PVK, it can be seen that the PL decay slows down and the PL intensity increases. This can be an indication that the TaTm effectively prevents electron extraction, which did not occur at the  $\text{MoO}_x/\text{PVK}$  interface. It is also suspected that there are less defects at the TaTm/PVK interface than at the  $\text{MoO}_x/\text{PVK}$ , which reduces the non-radiative recombination.



**Figure 5.4:** The PL lifetime derived from the TRPL measurement of the HTL/PVK stack and the  $V_{oc}$  and FF measured from the full device.

The PL lifetime of the samples is determined from the TRPL measurement. The calculations for the PL lifetime are depicted in Appendix D. Figure 5.4 displays the PL lifetime of the HTL/PVK samples, as well as the  $V_{oc}$  and FF of the full devices.

The PL lifetime of  $\text{MoO}_x/\text{PVK}$  and  $\text{MoO}_x/\text{TaTm}/\text{PVK}$  is shorter than for pristine PVK, while the PL lifetime of PTAA and TaTm is larger. For the most part, it can be seen that the  $V_{oc}$  and FF

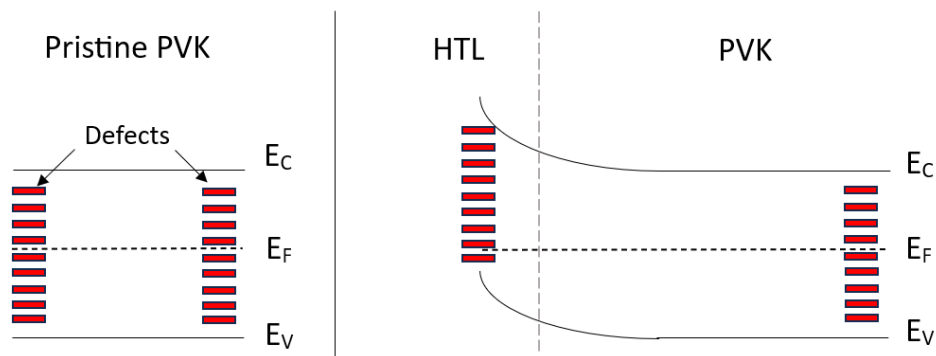
follow the same trend as the PL lifetime, which is in agreement with literature [10]. However, the exception for this trend is the TaTm/PVK stack. This stack shows the highest PL lifetime, but not the highest  $V_{oc}$  and FF. This deviation is a result of the hole extraction barrier at the FTO/TaTm interface as was discussed in Section 5.1. The FTO/TaTm interface is responsible for high series resistance, which negatively affects the FF. However, the TaTm/PVK stack for the TRPL measurement does not have an FTO/TaTm interface and the negative effects of its hole extraction barrier are therefore not reflected in the PL lifetime. PTAA has the second highest PL lifetime. Compared to TaTm, it is possible that PTAA has more defects at its interface with the PVK or does not block the electrons as well as TaTm does, resulting in more non-radiative recombination. However, the  $V_{oc}$  and FF are higher for PTAA, suggesting that the hole extraction at the FTO/PTAA interface is better than the hole extraction at the FTO/TaTm. This could be the reason why PTAA outperforms TaTm as HTL on a device level.

It must be noted that there is a certain contradiction in the PL and TRPL results for  $\text{MoO}_x/\text{TaTm}$ . The PL measurement implies that there is less non-radiative recombination with  $\text{MoO}_x/\text{TaTm}$  compared to the other HTLs. However, the decay in the TRPL suggests that there is more non-radiative recombination with  $\text{MoO}_x/\text{TaTm}$  than for the stacks with PTAA or TaTm. This difference could be caused due to nonuniform thickness of the TaTm layer, as is discussed in Section 4.1. The spot on the sample that was used for the PL measurement could have less or more TaTm than the spot on the sample for the TRPL measurement. Since both measurements show an improvement in hole extraction of  $\text{MoO}_x/\text{TaTm}$  compared to  $\text{MoO}_x$ , it can be presumed that this is valid. However, the PL and TRPL results of the hole extraction of  $\text{MoO}_x/\text{TaTm}$  compared to that of PTAA and TaTm are contradictory. Therefore it is not possible to reflect on the hole extraction of  $\text{MoO}_x/\text{TaTm}$  in comparison with PTAA and TaTm.

In many papers, the PL intensity peak of pristine PVK is higher compared to the PL intensity peak of an HTL/PVK stack [210][10][75][145][159]. It is reasoned that for samples with the addition of HTL, the holes are extracted from the PVK, which reduces the radiative recombination in the PVK and results in lower PL intensity peak. The holes and electrons will either be depleted due to non-radiative interfacial recombination, or the holes will accumulate in the HTL (due to absence of the electrode) which can eventually also lead to interface recombination [41]. In the time-resolved PL (TRPL), it is reasoned that the extraction of holes from the PVK by the HTL accelerates the PL decay. The stronger the decay, the higher either the hole extraction rate and interfacial recombination rate.

However, the opposite is observed in this study, where the PL intensity peak in the PL measurement is lower and the PL decay in the TRPL measurement is faster for pristine PVK compared to the HTL/PVK stack. The following explanation on the PL behavior is considered.

Figure 5.5 shows a schematic of the band diagram for pristine PVK, where defects are present at the surface. There is a 50% chance of an electron and a 50% chance of a hole to be found at the defect. The same chances are for one of the charge carriers to reach the filled defect and recombine. This is non-radiative recombination and is thus not detected by the PL spectrometer. When the PVK is deposited on top of an HTL, a heterojunction is formed and band bending occurs at the interface. A defect in this position is most likely filled with a hole, since a sufficient HTL only extracts holes and blocks electrons. Therefore, the chance of an electron being near the defect is slim, and thus the non-radiative recombination rate decreases. The decrease in non-radiative recombination (and thus an increase in radiative recombination) results in a higher PL intensity peak and slower PL decay for HTL/PVK stacks.



**Figure 5.5:** A sketch of the band diagram of pristine PVK and a HTL/PVK junction. Defects are found at the surface of pristine PVK, as well as near the HTL/PVK interface.

### Summary

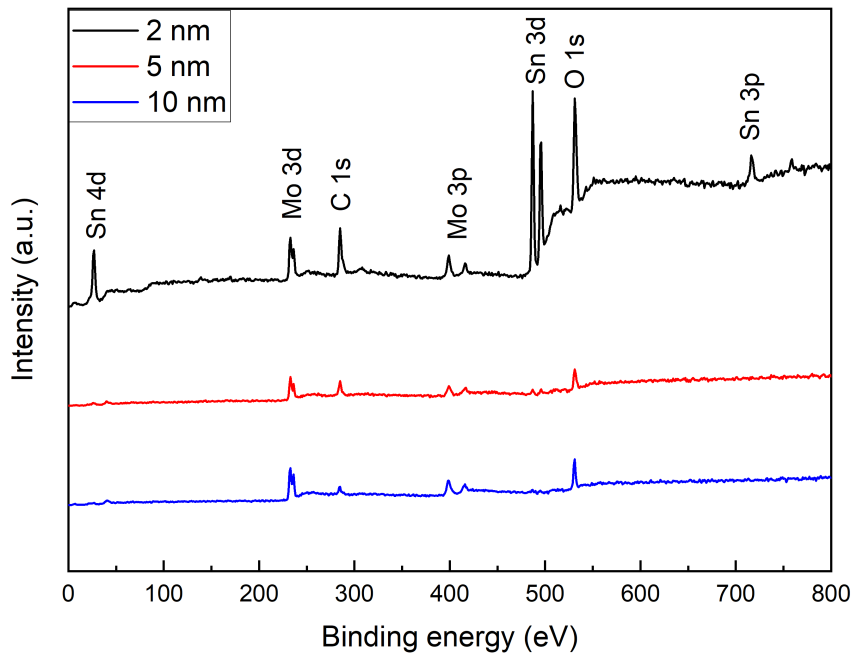
- The low non-radiative recombination at the TaTm/PVK interface confirms the presence of a high electron injection barrier.
- The non-radiative recombination at the MoO<sub>x</sub>/PVK interface confirms the presence of the low electron barrier at the interface and/or indicates a high number of interface defects.
- The addition of TaTm between MoO<sub>x</sub> and PVK decreases the non-radiative recombination by blocking the electrons and/or reducing the defects at the PVK interface.
- The TaTm/PVK interface demonstrates less non-radiative recombination than the PTAA/PVK interface. However, the  $V_{oc}$  and FF is highest for PTAA, which indicates that the FTO-TaTm interface compromises the device performance.

# Impact of Film Thickness of $\text{MoO}_x$ and TaTm on Device Parameters

The previous chapter compared the extraction properties and device performance of  $\text{MoO}_x$  and TaTm as single and double HTLs. The aim of this chapter is to examine how the thickness of these hole transport layers affects the device parameters. Section 6.1 discusses the influence of the thickness on the stoichiometry of  $\text{MoO}_x$ . The effect of layer thickness for  $\text{MoO}_x$  and TaTm is investigated as single HTL and double HTL in Section 6.2 and Section 6.3, respectively.

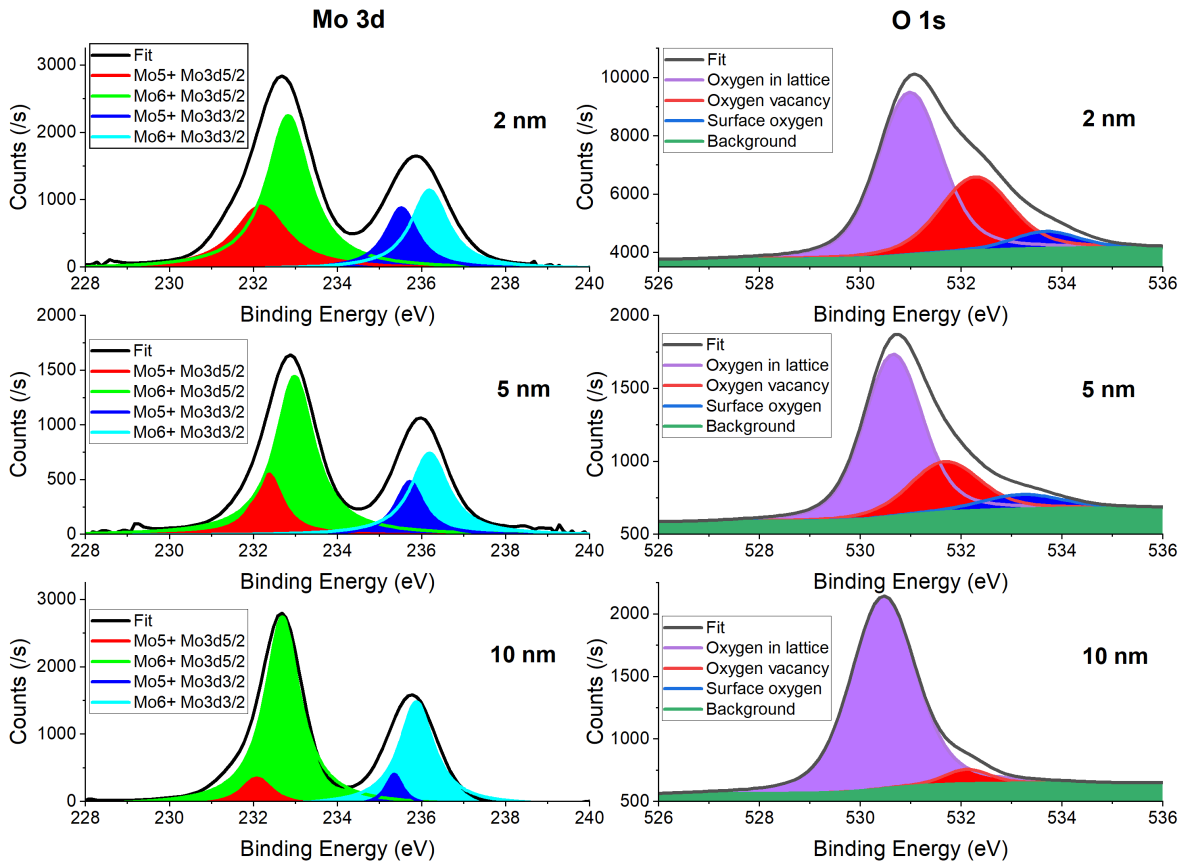
## 6.1. Effect of layer thickness on the atomic composition of $\text{MoO}_x$

The stoichiometry ( $x$ ) of  $\text{MoO}_x$  reportedly influences semiconductor material parameters such as the work function [54]. The impact of the film thickness on the stoichiometry is investigated by performing x-ray spectroscopy (XPS). XPS gives information on the atomic composition and chemical state of the elements in  $\text{MoO}_x$ . The samples used for this measurement have a  $\text{MoO}_x$  layer with the thickness 2 nm, 5 nm and 10 nm and are displayed in Section 3.3.3. Figure 6.1 shows the XPS survey that is obtained from the measurements. Each peak represents the presence of a certain element. The spectrum for the 2-nm thick  $\text{MoO}_x$  has peaks at binding energies that do not show up in the spectra for the 5-nm and 10-nm thick  $\text{MoO}_x$  layer. The peak at 27 eV and the peak at 720 eV can be related to tin (Sn), which is one of the compounds found in FTO. The FTO is probably detected because the thin  $\text{MoO}_x$  film does not uniformly cover the entire substrate. Thicker  $\text{MoO}_x$  provides better coverage and the FTO is therefore not detected in the 5-nm and 10-nm thick  $\text{MoO}_x$ .



**Figure 6.1:** XPS survey of  $\text{MoO}_x$  for different thicknesses.

Figure 6.2 shows the Mo 3d and O 1s peaks and Table 6.1 summarizes their binding energies. A peak deconvolution is performed to distinguish the overlapping peaks. Figure 6.2 shows the Mo 3d doublets of  $\text{MoO}_x$ , where the peak in the range of 232.5–233.0 eV represents  $\text{Mo } 3d_{5/2}$  and the peak in the range of 235.5–236 eV represents  $\text{Mo } 3d_{3/2}$ . By comparing the spectra for  $\text{MoO}_x$  with thicknesses from 2 to 10 nm, we observe slight asymmetry in the peak, indicating the presence of mixed oxidation states of Mo. The peak deconvolution shows that  $\text{Mo}^{5+}$  and  $\text{Mo}^{6+}$  are the oxidation states of Mo present in all three films. Both peaks become narrower with increasing film thickness, indicating the reduction of  $\text{Mo}^{5+}$  compared to  $\text{Mo}^{6+}$ . The increased presence of the  $\text{Mo}^{6+}$  compared to  $\text{Mo}^{5+}$  can be related to the O 1s peaks shown in Figure 6.2. The measured spectrum at film thickness of 2 nm is characterized by a clear asymmetric peak, where the right side of the peak is very wide. As the film thickness increases, the asymmetry and the width of the peak decrease. The peaks also shift to lower binding energy with increasing film thickness. The peak convolution shows the presence of three peaks, where the peak in the range of 530.4–531.0 eV is attributed to the  $\text{O}^{2-}$  ions present in the  $\text{MoO}_3$  lattice, while the peak in the range of 531.6–532.3 eV is attributed to the oxygen vacancies. The peak in the range of 533.2–533.7 eV represents the loosely bound oxygen on the surface. As the film thickness increases, the peak area of the oxygen vacancies consistently reduces and the peak area of the oxygen in the lattice increases. The peak for loosely bound oxygen on the surface is present in the 2-nm and 5-nm thick film but could not be detected in the 10-nm thick film.



**Figure 6.2:** XPS Mo and O scan for  $\text{MoO}_x$  with thicknesses of 2 nm, 5 nm, and 10 nm.

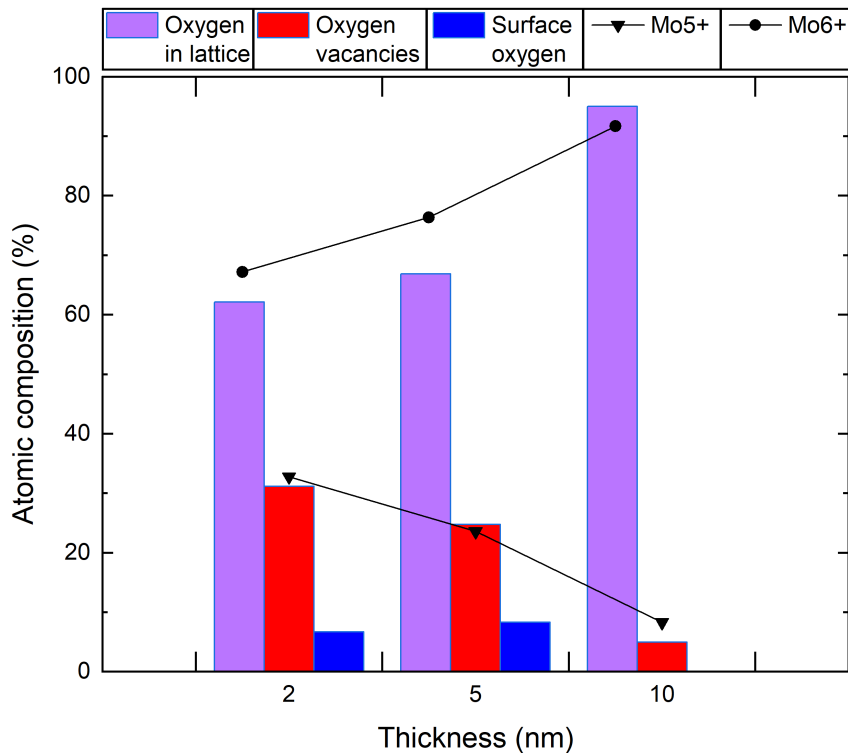
**Table 6.1:** XPS results for 2, 5 and 10-nm thick  $\text{MoO}_x$ .

Thick-ness	Binding energies (eV)					
	Mo		$\text{Mo}^{6+}$		$\text{Mo}^{5+}$	
	$3d_{5/2}$	$3d_{3/2}$	$3d_{5/2}$	$3d_{3/2}$	$3d_{5/2}$	$3d_{3/2}$
2 nm	232.68	235.88	232.84	236.19	232.18	235.52
5 nm	232.88	235.98	232.98	236.19	232.38	236.19
10 nm	232.68	235.78	232.69	235.88	232.08	235.36

Thick-ness	Binding energies (eV)				Ratios		
	O 1s	LO	OV	SO	O/Mo	$\text{Mo}^{6+}/\text{Mo}^{5+}$	LO/OV
2 nm	531.08	530.98	532.28	533.68	8.60	2.05	1.99
5 nm	530.78	530.68	531.68	533.28	2.89	3.24	2.70
10 nm	530.48	530.48	532.18	-	2.12	11.05	19.20

The atomic O/Mo ratio is the ratio of the lattice oxygen peak area and the Mo 3d peak area. The O/Mo ratio is equal to the stoichiometry ( $x$ ) of  $\text{MoO}_x$ , which should have a value between 2 and 3. However, an unrealistic value of 8.60 was calculated for the 2-nm thick film. When discussing Figure 6.1 at the beginning of this section, it was determined that the XPS also detected the FTO on which the  $\text{MoO}_x$  is deposited. FTO is rich in oxygen and therefore most of the detected oxygen does not belong to the  $\text{MoO}_x$ . The O/Mo ratios for the 5-nm and

10-nm thick films result in more consistent values of 2.89 and 2.12, respectively. However, the decrease of ratio does not follow the trends reported in literature, where the O/Mo ratio increases with high peaks of  $\text{Mo}^{6+}$  and lattice oxygen [62][58][208]. Another indication of the O/Mo ratio is the ratio between lattice oxygen and oxygen vacancies, as well as the  $\text{Mo}^{6+}/\text{Mo}^{5+}$  ratio. For stoichiometric  $\text{MoO}_x$ , where the O/Mo ratio is close to 3, we can conclude that there is a proper amount of oxygen in the lattice and therefore a low number of oxygen vacancies. The relative area of the three peaks in the O 1s spectra are extracted from Figure 6.2 and plotted in Figure 6.3 for all film thicknesses. As observed earlier, the oxygen in the lattice increases and the oxygen vacancies decreases, which indicates a higher O/Mo ratio. Figure 6.3 also illustrates the relative area of the  $\text{Mo}^{5+}$  and  $\text{Mo}^{6+}$  in the Mo 3d spectra. It can be observed that the relative area of  $\text{Mo}^{6+}$  in Mo 3d is almost equal to relative area of lattice oxygen in O 1s. For example, the relative area of  $\text{Mo}^{6+}$  in Mo 3d is 91.70% and the oxygen vacancies in O 1s is 95.05% for a thickness of 10 nm. The same trend is seen for the relative area of  $\text{Mo}^{5+}$  in Mo 3d (32.08% in 2-nm thick film) with the relative area of oxygen vacancies in O 1s (31.17% in 2-nm thick film). These trends are in agreement with literature, that has shown that stoichiometric  $\text{MoO}_x$  mostly contains  $\text{Mo}^{6+}$  and that the increase of oxygen vacancies increases the presence of lower oxidation state Mo [62][58][148][208][21].

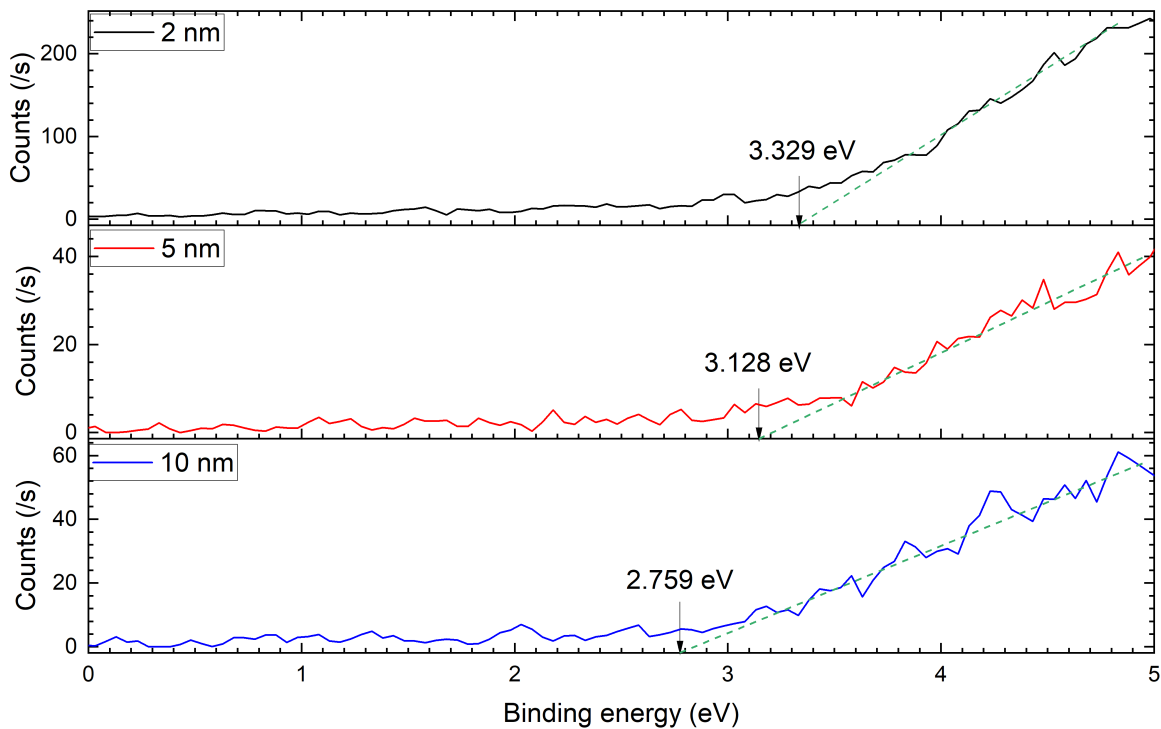


**Figure 6.3:** Atomic composition in % for Mo and O in different layer thicknesses of  $\text{MoO}_x$ . Those values are extracted from the spectra reported in Figure 6.2.

The valence band can be estimated at the lower binding energies of the XPS spectrum. The Fermi level is positioned at a binding energy of 0 eV. The leading edge of the spectra has a linear part in the slope. By extrapolating the linear part to the baseline, the valence band with respect to the Fermi level is obtained [209]. The extrapolation is depicted in Figure 6.4 for all samples. It can be seen that the valence band with respect to the Fermi level decreases



from 3.329 eV at 2 nm, to 3.128 eV at 5 nm, to 2.759 eV at 10 nm. A study by Mandani et al. shows similar results, where the valence band of e-beam evaporated  $\text{MoO}_x$  films decreases with film thickness [118]. In the above mentioned work, the authors also looked at larger film thicknesses of 50 nm and 100 nm, and found that these valence bands are the same as the valence band of the 10-nm thickness. It could be reasoned that there is no further increase in lattice oxygen, as has been shown to occur for thickness increase from 2 to 10 nm. This tells us that the film is stable from 10 nm onwards.



**Figure 6.4:** XPS for valence band calculation of  $\text{MoO}_x$  and TaTm with thicknesses of 2 nm, 5 nm, and 10 nm.

### Summary

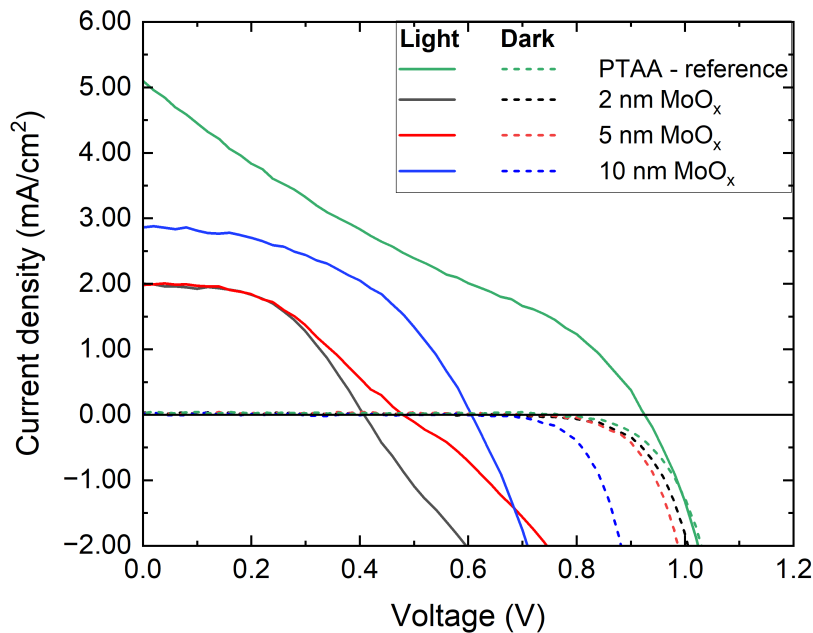
- The XPS measurement also detects the FTO for the 2-nm thick  $\text{MoO}_x$ . The XPS therefore determined an unrealistic stoichiometry of 8.60.
- The  $\text{Mo}^{6+}/\text{Mo}^{5+}$  ratio increases with  $\text{MoO}_x$  thickness and correlates with to the Lattice Oxygen / Oxygen Vacancies ratio. So the most  $\text{Mo}^{5+}$  and oxygen vacancies is found in 2-nm  $\text{MoO}_x$  and decreases with thickness.
- The valence band with respect to the Fermi level decreases with  $\text{MoO}_x$  thickness.
- The  $\text{MoO}_x$  is stable from 10-nm onwards.

## 6.2. Effect of single hole transport layer thickness on the device performance

In this section, the device parameters of solar cells with  $\text{MoO}_x$  or TaTm as single HTL are discussed. By examining  $\text{MoO}_x$  and TaTm as single HTL, it can give more insight on the thickness-dependency of each material.

### Solar cells demonstration with $\text{MoO}_x$ as HTL

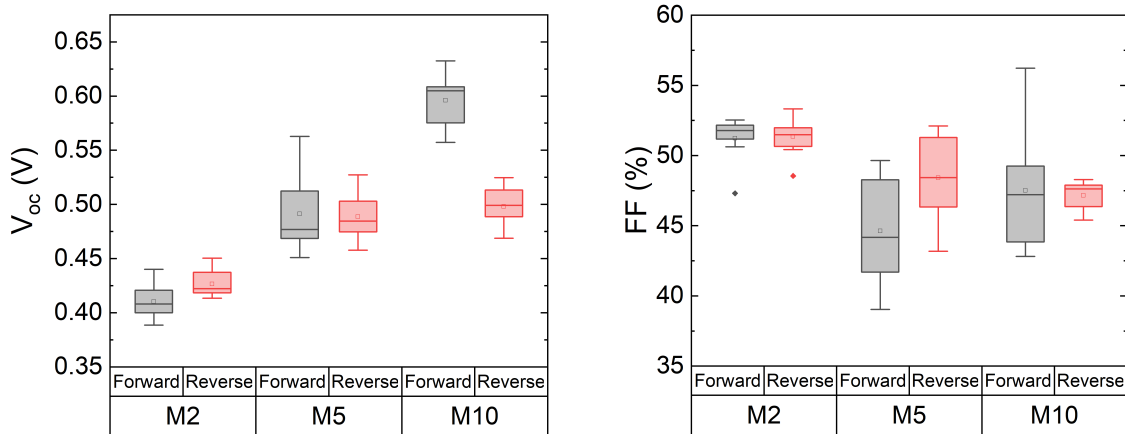
Devices with varying thickness of  $\text{MoO}_x$  as hole transport layer were fabricated according to the flowchart in Section 3.2. Figure 6.5 shows the illuminate and dark J-V curve of these devices. The rectangular shape of the dark J-V curves indicates diode curves proper of solar cells and is observed for all four devices. The illuminate J-V curve for PTAA is characterized by a strong S-shape, which indicates an issue with charge carrier extraction. In Section 5.1, it has been explained that this issue is the result of the faulty ETL and affects all the devices. The S-shape is weaker when replacing the PTAA with the  $\text{MoO}_x$ . However, using  $\text{MoO}_x$  as HTL also results in lower  $V_{oc}$  and  $J_{sc}$ . When comparing the curves for 2, 5 and 10-nm thick  $\text{MoO}_x$ , it is shown that the  $V_{oc}$  increases with thickness. The  $J_{sc}$  seems the same for the 2 and 5-nm thick  $\text{MoO}_x$ , but is higher for 10-nm thick  $\text{MoO}_x$ . Lastly, it is observed that the curve for the 5-nm thick  $\text{MoO}_x$  has a slope at higher voltage that is less steep compared to the 2 and 10-nm thick layer, indicating that there is a higher series resistance.



**Figure 6.5:** Dark and illuminate J-V curves of solar cells with PTAA as reference HTL and 2, 5 and 10-nm thick  $\text{MoO}_x$ .

Figure 6.6 depicts the  $V_{oc}$  and FF for the 2, 5, and 10-nm thick  $\text{MoO}_x$ . The boxplots contain data from 18 cells for each thickness. Boxplots for other device parameters can be found in Appendix E. The average values of the device parameters are extracted from the boxplots and summarized in Table 6.2. A clear trend can be seen where the average  $V_{oc}$  increases from 0.410 V at 2-nm thickness to 0.596 V at 10-nm thickness. A potential explanation for this behavior is related to the atomic composition of  $\text{MoO}_x$  for the layer thickness. As discussed in the Section 6.1, the  $\text{MoO}_x$  is more stoichiometric with increasing thickness. The  $\text{Mo}^{6+}$  and oxygen in the lattice increase with thickness, while the  $\text{Mo}^{5+}$  and oxygen vacancies decrease. It is reported that the decrease in  $\text{Mo}^{5+}$  and oxygen vacancies in thicker  $\text{MoO}_x$  increases the work function, resulting in an increased interfacial dipole between the  $\text{MoO}_x$  and PVK [118]. Numerical simulations by Yang et al. have shown that the dipole enhances the built-in electric field, resulting in less charge accumulation at the interface [187]. This leads to reduced non-

radiative interfacial recombination and an improved  $V_{oc}$ .



**Figure 6.6:** Box plots for  $V_{oc}$  and FF of solar cells with 2, 5 and 10-nm thick  $\text{MoO}_x$ . The data is retrieved from 18 cells for each thickness.

From Table 6.2, it can be observed that the same trend for  $V_{oc}$  exists for the PCE. The increase of PCE with film thickness is also in agreement with findings from Mandani et al. [118]. The authors also found that the PCE remains unchanged with further increase of the  $\text{MoO}_x$  above 10 nm. Although thicknesses above 10 nm are not tested in this work, the stabilization of the PCE found by Mandani et al. could suggest that the increasing trend seen for  $V_{oc}$  and PCE in this work does not continue for thickness of  $\text{MoO}_x$  above 10 nm.

As discussed, the device with 2-nm thick  $\text{MoO}_x$  has the lowest  $V_{oc}$ . However, it also demonstrates the highest FF. This is in contradiction with the results from Mandani et al., which sees an increase of FF with the  $\text{MoO}_x$  thickness [118].

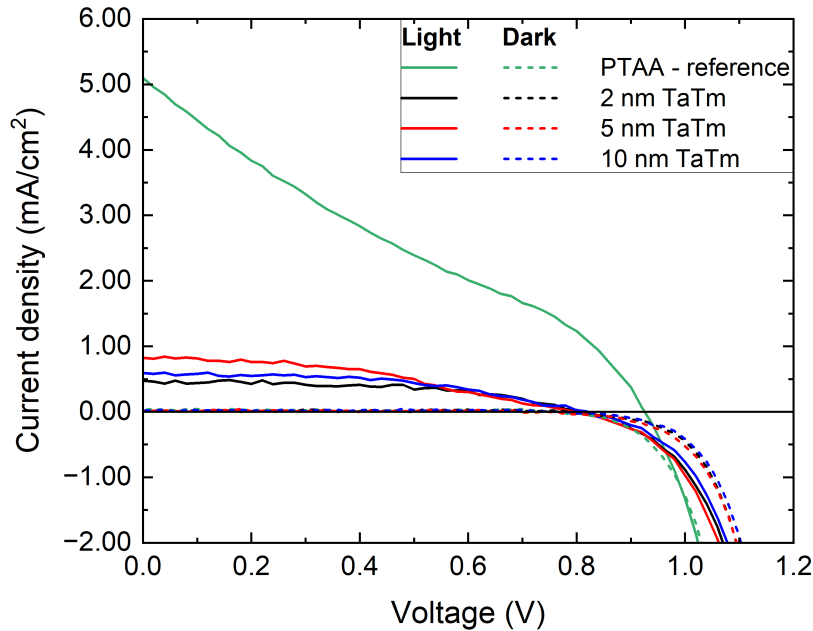
**Table 6.2:** Device parameters of solar cells with 2, 5 and 10-nm thick  $\text{MoO}_x$  for forward and reverse scan. The data is the average value retrieved from 18 cells for each thickness.

Device Parameters	Thickness					
	2 nm		5 nm		10 nm	
	Forward	Reverse	Forward	Reverse	Forward	Reverse
$V_{oc}$ (V)	0.410	0.426	0.491	0.489	0.596	0.498
$J_{sc}$ ( $\text{mA}/\text{cm}^2$ )	1.970	1.960	1.998	1.995	2.465	2.362
FF (%)	51.23	51.35	44.62	48.42	47.51	47.16
PCE (%)	0.415	0.429	0.435	0.470	0.704	0.554
$R_s$ ( $\Omega$ )	75.69	72.61	144.32	116.69	79.46	73.16
HI (-)	0.037		0.074		0.268	

### Solar cells demonstration with TaTm as HTL

Devices with varying thickness of TaTm as hole transport layer were fabricated according to the flowchart in Section 3.2. Figure 6.7 shows the illuminate and dark J-V curve of these devices. The rectangular shape of the dark J-V curves indicates diode curves proper of solar cells and is observed for all four devices. The illuminate J-V curve for PTAA is characterized by a strong S-shape, which indicates an issue with charge carrier extraction. In Section 5.1, it has been explained that this issue is the result of the faulty ETL and affects all the devices.

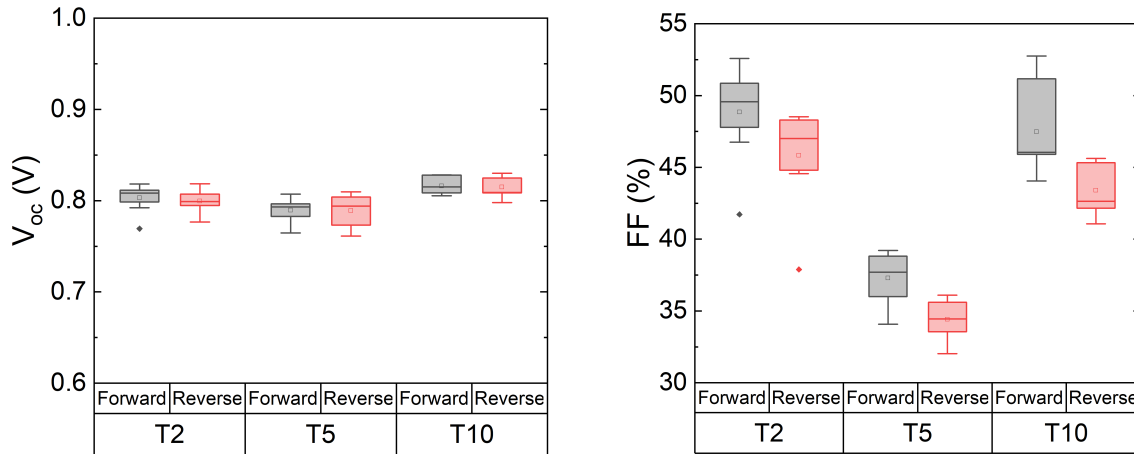
The S-shape for the PTAA is no longer present when replaced with the  $\text{MoO}_x$ . However, using TaTm as HTL reduces the  $V_{oc}$  and significantly diminishes the  $J_{sc}$ . When comparing the curves for 2, 5 and 10-nm thick TaTm, the  $V_{oc}$  and  $J_{sc}$  are constant. The reduced slope of the J-V curve around the  $V_{oc}$  indicates a high series resistance, and is observed for all three thickness.



**Figure 6.7:** Dark and illuminate J-V curves of solar cells with PTAA as reference HTL and 2, 5 and 10-nm thick TaTm.

Figure 6.8 depicts the  $V_{oc}$  and FF for the 2, 5, and 10-nm thick TaTm. The boxplots contain data from 18 cells for each thickness. Boxplots for other device parameters can be found in Appendix E. The average values of the device parameters are extracted from the boxplots and summarized in Table 6.3. It was initially hypothesized that the increased TaTm thickness would reduce the islanding and therefore improve the coverage of TaTm on the FTO. Then there would be less contact points between the FTO and the PVK, resulting in less recombination and an improved  $V_{oc}$ . However, it is observed from Figure 6.8 that the thickness has no effect on the average  $V_{oc}$ . In Section 5.1, it was discussed that there is poor energy level alignment at the FTO/TaTm. The  $J_{sc}$  is very low, which means that charge carriers are not collected at all. Therefore, it could be possible that there is so much recombination at the FTO/TaTm interface that the thickness does not play a role.

Susic et al. also conducted a thickness optimization study using TaTm as the HTL [176]. Other than a different perovskite, the same device structure and the same variation of thicknesses for TaTm were used. Similarities between the results can be found. They also observed no change in  $V_{oc}$ . However, some other results of their study contradict with our results. The results by Susic et al. show a reduced performance with the 10-nm film, where a slight S-shape of the J-V curve, a reduced FF and increased series resistance were observed compared to the smaller thicknesses. In our devices, a large series resistance is observed for all thicknesses of TaTm.



**Figure 6.8:** Box plots for  $V_{oc}$  and FF of solar cells with 2, 5 and 10-nm thick TaTm. The data is retrieved from 18 cells for each thickness.

**Table 6.3:** Device parameters of solar cells with 2, 5 and 10-nm thick TaTm for forward and reverse scan. The data is the average value retrieved from 18 cells for each thickness.

Device Parameters	Thickness					
	2 nm		5 nm		10 nm	
	Forward	Reverse	Forward	Reverse	Forward	Reverse
$V_{oc}$ (V)	0.803	0.800	0.790	0.789	0.816	0.815
$J_{sc}$ (mA/cm <sup>2</sup> )	0.502	0.511	0.916	0.936	0.575	0.518
FF (%)	48.84	45.83	37.29	34.42	47.48	43.40
PCE (%)	0.196	0.185	0.269	0.254	0.223	0.205
$R_s$ ( $\Omega$ )	481.27	489.94	559.29	565.99	489.30	537.77
HI (-)	0.059		0.062		0.089	

Although the unvaried  $V_{oc}$  suggest that the thickness does not influence the device performance, the device with 5-nm thick TaTm shows deviant results. The FF of the 5-nm thick TaTm is considerably lower than for the 2-nm and the 10-nm film. The study by Susic et al. also showed deviance in the results for the 5-nm layer, with low FF and  $V_{oc}$  compared to the 2-nm layer [176]. However, the value of these parameters stabilized and were comparable with those of the 2-nm layer after 3-4 repetitions of the J-V measurement. The same dynamic behaviour was observed under simulated solar illumination, a LED solar simulator with UV-component and a halogen lamp with no UV-component. Susic therefore suggested that the light spectrum plays no important role in the device activation.

For our study, the J-V measurement were not repeated. It is possible that similar stabilization is needed to retrieve accurate values for the device parameters. The device performance with the 5-nm layer is therefore expected to be the same as the 2-nm and 10-nm layer, and it is carefully concluded that the thickness of the TaTm layer has no influence on the device performance. This would be in line with the study by Du et al, where no change in FF or series resistance with increasing film thickness of TaTm as HTL was observed [41].

### Summary

- $\text{MoO}_x$  has a clear trend where the  $V_{oc}$  increases with thickness. The decrease of  $\text{Mo}^{5+}$  and oxygen vacancies in thicker  $\text{MoO}_x$  increases the WF and interface dipole, resulting in less interfacial recombination.

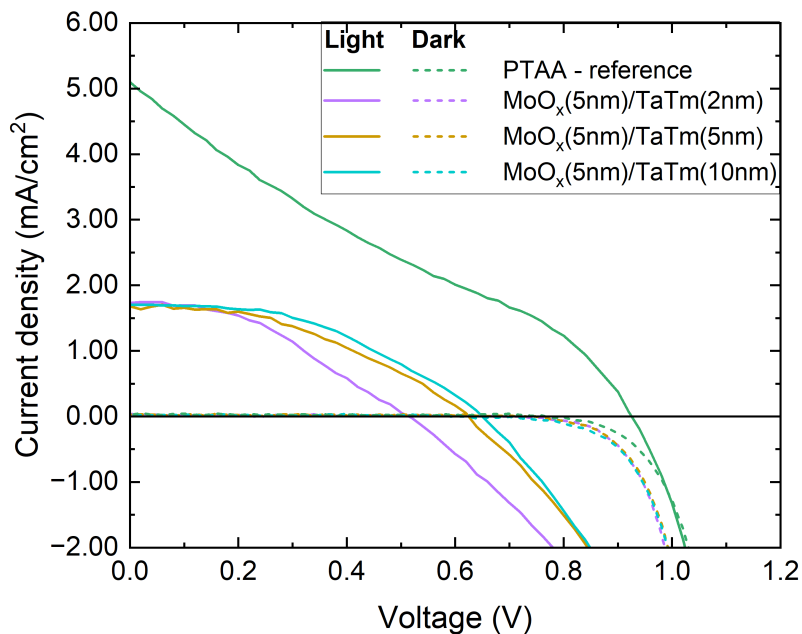
- The thickness of TaTm has no influence on the  $V_{oc}$ .
- The PSC with 5-nm thick TaTm showed a lower FF than the 2-nm and 10-nm thick TaTm. Due to device activation, the FF of the 5-nm thick TaTm is expected to stabilize and reach a similar FF as the others after multiple repetitions of the J-V measurement.

### 6.3. Effect of double hole transport layer thickness on the device performance

After examining  $\text{MoO}_x$  and TaTm as single HTLs, the device parameters of solar cells with  $\text{MoO}_x$  and TaTm as double HTL are discussed in this section. The thickness of one HTL is kept constant while the thickness of the other HTL is varied. This gives insight on the thickness dependency of each material when used as a double HTL as opposed to being used as a single HTL.

#### Solar cells demonstration with TaTm on top of 5-nm $\text{MoO}_x$

The same devices with varying TaTm thickness as in Section 6.2 have been fabricated with the insertion of a 5-nm thick  $\text{MoO}_x$  between the FTO and TaTm. This is done to see how the high-WF interlayer influences the effect of TaTm thickness on the device parameters. The dark and illuminate J-V curve of the devices are displayed in Figure 6.9. The rectangular shape of the dark J-V curves indicates diode curves proper of solar cells and is observed for all four devices. The illuminate J-V curve for PTAA is characterized by a strong S-shape, which indicates an issue with charge carrier extraction. In Section 5.1, it has been explained that this issue is the result of the faulty ETL and affects all the devices. The S-shape for the PTAA is no longer present when replaced with the double HTL of  $\text{MoO}_x$  and TaTm. However, using  $\text{MoO}_x$  and TaTm as HTLs reduces the  $V_{oc}$  and the  $J_{sc}$ . When comparing the curves for 2, 5 and 10-nm thick TaTm, the  $V_{oc}$  increases with thickness while the  $J_{sc}$  stays constant.

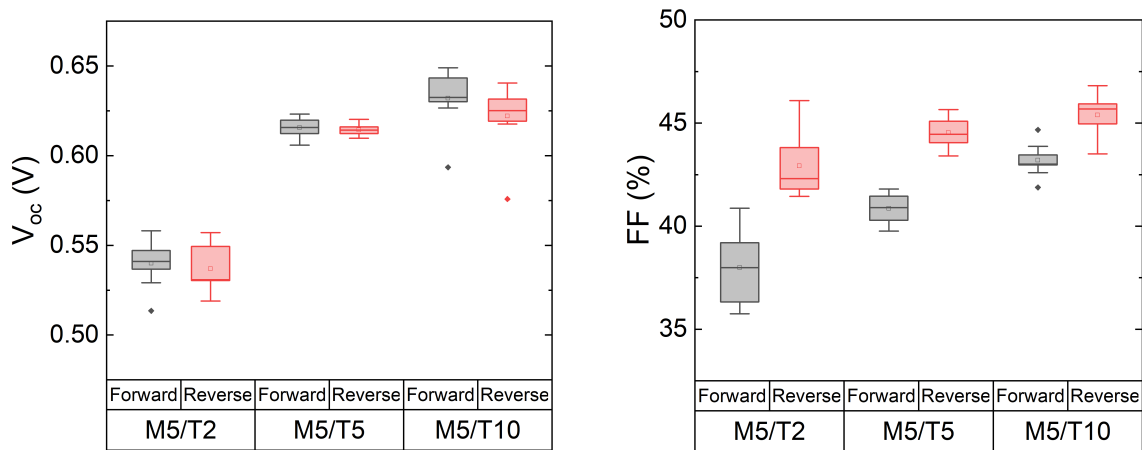


**Figure 6.9:** Dark and illuminate J-V curves of solar cells with PTAA as reference HTL and 2, 5 and 10-nm thick TaTm on top of 5-nm thick  $\text{MoO}_x$ .

In Section 6.2, it was hypothesized that the thickness-increase of TaTm would lead to better coverage and improved  $V_{oc}$ . This explanation was not confirmed by our experimental findings for TaTm as single hole transport in Section 6.2. However, based on the results in Figure 6.10, the hypothesis seems to be valid when the TaTm is combined with  $\text{MoO}_x$ . In Figure 6.10, the average  $V_{oc}$  shows a larger improvement when increasing the TaTm thickness from 2 to 5 nm than from 5 to 10 nm. This can be explained by the island growth that has been shown for TaTm in Section 4.1. At the lower thickness, there are many islands. As the deposition of the TaTm increases, the size of the islands will expand and connect. The coalescence or merging of the islands result in elongated structures that will ultimately form into a flat film [196]. The  $V_{oc}$  increases the most for the initial increase of film thickness, as this is when the growth of the islands improves the coverage the most. When the islands start to merge, the coverage slows down and hence the increase in  $V_{oc}$  becomes smaller. The  $V_{oc}$  will be constant once the substrate is reaches full coverage at a certain thickness.

An additional explanation for the increase of  $V_{oc}$  with thickness of TaTm is that the electron blocking is improved. For a thin layer of TaTm, it is possible for electrons to tunnel through the TaTm and reach the  $\text{MoO}_x$ . These electrons will recombine with the holes, which results in a low  $V_{oc}$ . However, the probability of a charge carrier to tunnel through a layer decreases when the layer thickness increases. So, a thicker layer of TaTm reduces the recombination and result in a higher  $V_{oc}$ .

In Figure 6.10, an increase of FF with increasing thickness of TaTm is also found, which indicates that the  $V_{oc}$  has the most influence on the device performance. It is observed from Table 6.4 that the  $J_{sc}$  stays constant and thus seems to be independent of the TaTm thickness. The series resistance also does not increase, meaning that the thickness of TaTm is not considered too thick yet where it limits the hole mobility and negatively affects the FF and PCE. The thickness of TaTm could thus be increased further than 10 nm to improve the device performance.



**Figure 6.10:** Box plots for  $V_{oc}$  and FF of solar cells with 2, 5 and 10-nm thick TaTm on top of 5-nm thick  $\text{MoO}_x$ . The data is retrieved from 18 cells for each thickness.

**Table 6.4:** Device parameters of solar cells with 2, 5 and 10-nm thick TaTm on 5-nm thick MoO<sub>x</sub> for forward and reverse scan. The data is the average value retrieved from 18 cells for each thickness.

Device Parameters	Thickness					
	2 nm		5 nm		10 nm	
	Forward	Reverse	Forward	Reverse	Forward	Reverse
$V_{oc}$ (V)	0.540	0.537	0.616	0.614	0.632	0.622
$J_{sc}$ (mA/cm <sup>2</sup> )	1.665	1.687	1.652	1.592	1.663	1.667
FF (%)	37.99	42.92	40.86	44.53	43.20	45.38
PCE (%)	0.342	0.386	0.416	0.436	0.454	0.471
$R_s$ ( $\Omega$ )	206.96	183.99	158.69	157.44	136.28	134.14
HI (-)	0.122		0.047		0.052	

#### Solar cells demonstration with MoO<sub>x</sub> in between FTO and 5-nm TaTm

The same devices with varying MoO<sub>x</sub> thickness as in Section 6.2 have been fabricated with the insertion of a 5-nm thick TaTm between the MoO<sub>x</sub> and PVK. The dark and illuminate J-V curve of the devices are displayed in Figure 6.11. The rectangular shape of the dark J-V curves indicates diode curves proper of solar cells and is observed for all four devices. The illuminate J-V curve for PTAA is characterized by a strong S-shape, which indicates an issue with charge carrier extraction. In Section 5.1, it has been explained that this issue is the result of the faulty ETL and affects all the devices. The S-shape for the PTAA is no longer present when replaced with the double HTL of MoO<sub>x</sub> and TaTm. However, using MoO<sub>x</sub> and TaTm as HTLs reduces the  $V_{oc}$  and the  $J_{sc}$ . When comparing the curves for 2, 5 and 10-nm thick MoO<sub>x</sub>, the  $V_{oc}$  decreases with increasing thickness of MoO<sub>x</sub> while the  $J_{sc}$  remains constant. The steep slope of the J-V curve around the  $V_{oc}$  for the 2-nm thick MoO<sub>x</sub> indicates low series resistance compared to the devices with thicker MoO<sub>x</sub>.

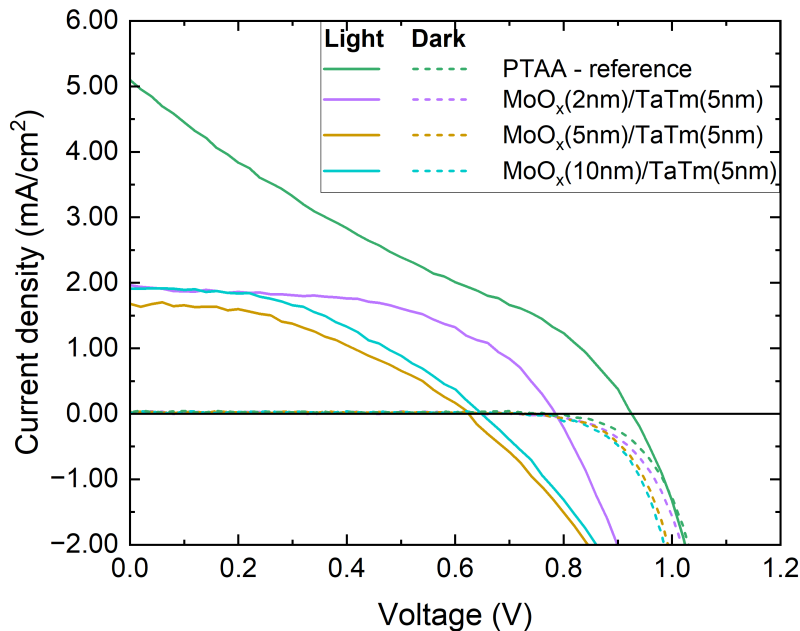
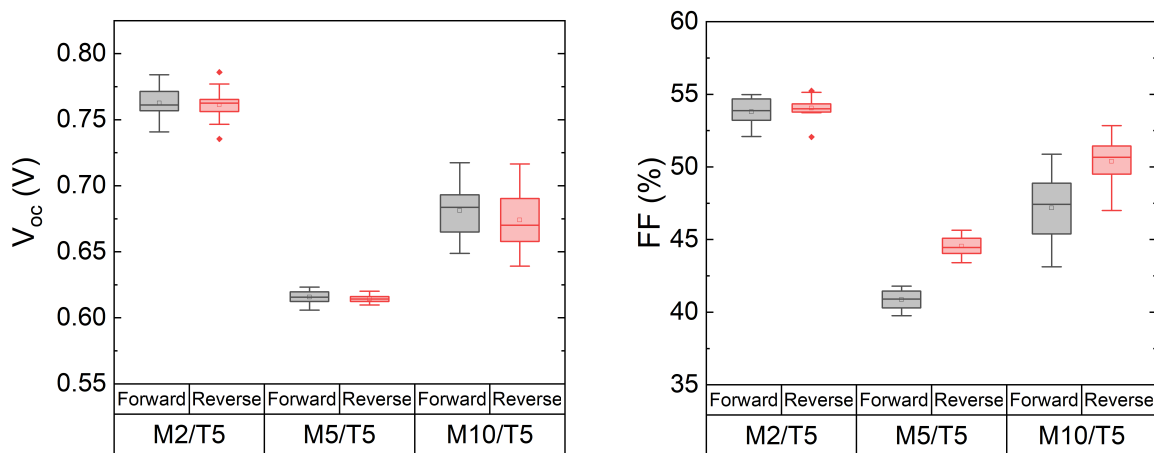
**Figure 6.11:** Dark and illuminate J-V curves of solar cells with PTAA as reference HTL and 2, 5 and 10-nm thick MoO<sub>x</sub> in between FTO and 5-nm thick TaTm.



Table 6.5 summarizes the average values of the device parameters for 2, 5 and 10-nm thick  $\text{MoO}_x$  interlayer. It shows that the highest FF is achieved for the 2-nm  $\text{MoO}_x$ . The high FF using a thin layer of  $\text{MoO}_x$  can be related to the results from Section 6.1, where it was observed that the thinner  $\text{MoO}_x$  layer has the most oxygen vacancies.  $\text{Mo}^{5+}$  originates from the oxygen vacancies, and is shown by several studies to be the origin of the gap state in the  $\text{MoO}_x$  layer [84][158][192]. Kanai et al. reason that this gap state is nearly aligned with the HOMO level of an organic layer on the  $\text{MoO}_x$ , which reduces the hole-extraction barrier [84]. This can be explained with the band energy diagram discussed in Section 2.3.3. The gap states of the  $\text{Mo}^{5+}$  will be filled the electrons moving from the FTO to the  $\text{MoO}_x/\text{TaTm}$  interface. The alignment with the VB of TaTm enables holes in the TaTm to reach the gap states and recombine with the electrons. The recombination at  $\text{MoO}_x/\text{TaTm}$  interface supports further influx of electrons from the FTO to the  $\text{MoO}_x/\text{TaTm}$  interface, which is equivalent to holes moving from the  $\text{MoO}_x/\text{TaTm}$  to the FTO. Compared to the thicker  $\text{MoO}_x$ , the higher FF of the 2-nm  $\text{MoO}_x$  is an indication of better hole transport resulting from the reduced barrier.

Figure 6.12 shows the device parameters for 2, 5 and 10-nm thick  $\text{MoO}_x$  interlayer. The boxplots contain data from 18 cells for each thickness. A clear trend can be observed where the 2-nm thick  $\text{MoO}_x$  has the highest  $V_{oc}$  and FF, but the values decrease significantly when increasing the  $\text{MoO}_x$  thickness to 5 nm. Increasing the  $\text{MoO}_x$  to 10 nm improves the  $V_{oc}$  and FF, although not back to the values observed for the 2-nm  $\text{MoO}_x$ . It is more difficult to suggest the explanation for this trend. A possible explanation is that there are no longer gap states that align with the HOMO level for interlayer thicknesses above 2 nm. Therefore, the hole extraction barrier between the  $\text{MoO}_x$  and TaTm becomes higher. Beyond a thickness of 2 nm, the device shows the same behaviour as the devices without TaTm layer, where an increase in  $\text{MoO}_x$  thickness increases the interface dipole and results in an higher  $V_{oc}$  (see Section 6.2). The TaTm solely functions as buffer layer between the  $\text{MoO}_x$  and the PVK. Similar behaviour is noticed in a study by Schulz et al. [159], where they increased the thickness of  $\text{MoO}_x$  which was sandwiched between the ITO and organic HTL Spiro-MeOTAD. They found that when the  $\text{MoO}_x$  was increased to a thickness above 2 nm, the electronic structure was the same as for the device without Spiro-MeOTAD interlayer.



**Figure 6.12:** Box plots for  $V_{oc}$  and FF of solar cells with 2, 5 and 10-nm thick  $\text{MoO}_x$  in between FTO and 5-nm thick TaTm. The data is retrieved from 18 cells for each thickness.

**Table 6.5:** Device parameters of solar cells with 2, 5 and 10-nm thick MoO<sub>x</sub> in between FTO and 5-nm thick TaTm for forward and reverse scan. The data is the average value retrieved from 18 cells for each thickness.

Device Parameters	Thickness					
	2 nm		5 nm		10 nm	
	Forward	Reverse	Forward	Reverse	Forward	Reverse
V <sub>oc</sub> (V)	0.736	0.761	0.616	0.614	0.681	0.674
J <sub>sc</sub> (mA/cm <sup>2</sup> )	1.815	1.804	1.652	1.592	1.755	1.740
FF (%)	53.80	54.05	40.86	44.53	47.17	50.38
PCE (%)	0.745	0.742	0.416	0.436	0.563	0.591
R <sub>s</sub> (Ω)	85.37	91.72	158.69	157.44	131.53	123.04
HI (-)	0.025		0.047		0.047	

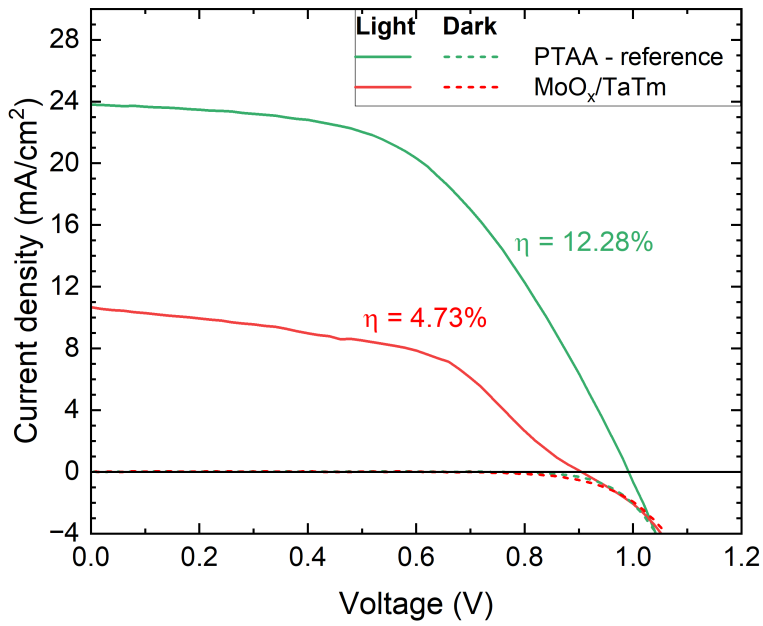
### Final results

A last batch was created to compare solar cells using PTAA with solar cells using MoO<sub>x</sub>/TaTm, without the influence of the faulty ETL. Due to time limitation, the only fabricated devices were with PTAA and with one combination of MoO<sub>x</sub> and TaTm.

Based on the results in this chapter, the device with a double HTL of 2-nm thick MoO<sub>x</sub> and 5-nm thick TaTm showed to be the most promising configuration. The most promising configuration having a MoO<sub>x</sub> interlayer with a thickness between 0.5 and 3 nm, is in agreement with findings in the review on metal oxide/organic interfaces by Greiner et Lu [54].

The dark and illuminate J-V curves of the fabricated solar cells are shown in Figure 6.13. An improvement of V<sub>oc</sub> and a significant increase in J<sub>sc</sub> is observed for the J-V curve of both PTAA and MoO<sub>x</sub>/TaTm compared to the previous batch. Also, the J-V curve for PTAA has a much weaker S-shaped while the S-shape in the J-V curve for MoO<sub>x</sub>/TaTm has slightly increased compared to the previous batch.

Table 6.6 displays the device parameters of the two PSCs. It shows that the V<sub>oc</sub>, J<sub>sc</sub> and FF are lower for MoO<sub>x</sub>/TaTm than for PTAA. The lower FF and higher series resistance for MoO<sub>x</sub>/TaTm can indicate a hole extraction barrier at the FTO/MoO<sub>x</sub>, MoO<sub>x</sub>/TaTm and/or TaTm/PVK interface. The J<sub>sc</sub> is the most limiting factor, being only 10.622 mA/cm<sup>2</sup> for MoO<sub>x</sub>/TaTm compared to 23.513 mA/cm<sup>2</sup> for PTAA. In the end, a PCE of 4.725% is achieved for MoO<sub>x</sub>/TaTm compared to a PCE of 12.284% for PTAA, showing that further research is needed to improve the device with MoO<sub>x</sub>/TaTm before it can replace the spincoated PTAA.



**Figure 6.13:** Dark and illuminate J-V curves of solar cells with PTAA and MoO<sub>x</sub>(2 nm)/TaTm(5 nm)

**Table 6.6:** Device parameters of highest performing solar cells with PTAA and MoO<sub>x</sub>(2 nm)/TaTm(5 nm).

Device Parameters	HTL	
	PTAA	MoO <sub>x</sub> /TaTm
V <sub>oc</sub> (V)	0.978	0.904
J <sub>sc</sub> (mA/cm <sup>2</sup> )	23.513	10.622
FF (%)	53.40	49.18
PCE (%)	12.284	4.725
R <sub>s</sub> (Ω)	10.564	49.994

### Summary

- The V<sub>oc</sub> and FF increase with increasing thickness of TaTm on 5-nm thick MoO<sub>x</sub>. Due to the islanding of TaTm, the increasing thickness leads to better coverage of the TaTm on the MoO<sub>x</sub>. This results in improved electron blocking between the PVK and HTL.
- The V<sub>oc</sub> and FF is highest for 2-nm thick MoO<sub>x</sub> between FTO and 5-nm thick TaTm. The gap states of Mo<sup>5+</sup> align with the VB of TaTm which improves the electron transfer from the FTO to the MoO<sub>x</sub>/TaTm interface and therefore decreases the hole extraction barrier. For larger thicknesses of MoO<sub>x</sub> between FTO and 5-nm thick TaTm, the same trend for single HTL MoO<sub>x</sub> is observed in which V<sub>oc</sub> increases with thickness.
- In the final batch, PTAA achieved a PCE of 12.28% and MoO<sub>x</sub>(2 nm)/TaTm(5 nm) achieved a PCE of 4.73%. The J<sub>sc</sub> is the limiting factor for the MoO<sub>x</sub>/TaTm compared to PTAA.

## Conclusion and Recommendations

A study has been carried out to incorporate thermally evaporated  $\text{MoO}_x$  and TaTm as hole transport layers in perovskite solar cells. The study focused on three research objectives: (i) Preparing the integration of thermally evaporated  $\text{MoO}_x$  and TaTm in the PSC by determining the tooling factor and evaluating the thermal stability of optoelectrical properties, (ii) Assess the charge carrier extraction of  $\text{MoO}_x$  and TaTm, (iii) Determine the influence of the  $\text{MoO}_x$  and TaTm thickness on the device parameters. The main findings of this study are summarized in Section 7.1. Based on the findings in this study, suggestions for further investigation are proposed in Section 7.2.

### 7.1. Conclusion

**Preparing the integration of thermally evaporated  $\text{MoO}_x$  and TaTm in the PSC**

The tooling factors of  $\text{MoO}_x$  and TaTm have been determined to be able to control the thickness of the fabricated films. The optical properties of  $\text{MoO}_x$  are too similar to the glass substrate in order for the spectral ellipsometer to be able to measure the  $\text{MoO}_x$  thickness. Therefore, the  $\text{MoO}_x$  was deposited on silicon wafer to measure its thickness. For TaTm, it was found that the film was nonuniform on glass and ITO covered glass due to the formation of islands. A thicker layer of TaTm deposited on silicon wafer created a more uniform film. The film thickness was eventually determined with SEM, by measuring the cross section of the film. With the measured film thicknesses, the tooling factors of  $\text{MoO}_x$  and TaTm were found to be 4.19 and 1.80, respectively.

Furthermore, the optoelectrical properties of  $\text{MoO}_x$  and TaTm after different annealing conditions were studied to determine if  $\text{MoO}_x$  and TaTm are able to withstand annealing temperatures necessary to fabricate high quality perovskite. For  $\text{MoO}_x$ , a slight decrease in transmittance was detected, which is attributed to an increase in oxygen vacancies. For both  $\text{MoO}_x$  and TaTm, no significant change in absorbance was found, indicating that there is no degradation at any annealing condition. However, white spots were visible in the TaTm film of other samples after annealing at  $170^\circ\text{C}$  for 30 minutes and  $200^\circ\text{C}$  for 10, 20 and 30 minutes, indicating the occurrence of degradation. Lastly, the estimated bandgap of  $\text{MoO}_x$  and TaTm were retrieved from the Tauc plot and also showed no change after annealing at various conditions.

**Assess the charge carrier extraction of  $\text{MoO}_x$  and TaTm**

The charge carrier extraction of  $\text{MoO}_x$  and TaTm are discussed by comparing J-V curves of the devices with single and double hole transport layer and supporting the finding with (TR)PL measurements.

The low  $V_{oc}$  of the PSC with  $\text{MoO}_x$  as HTL indicates an unfavourable energy level alignment, which was found to be caused by a chemical reaction occurring at the  $\text{MoO}_x$ /PVK interface. The energy level alignment of  $\text{MoO}_x$  allowed for electron extraction. This was supported by the (TR)PL measurements of the  $\text{MoO}_x$ /PVK stack that showed high interfacial recombination.

The PSC with TaTm as HTL demonstrated low  $J_{sc}$  and high series resistance, originating from a mismatch of energy levels at the FTO/TaTm interface. This is also supported by the (TR)PL measurements, that showed low interfacial recombination at the TaTm/PVK interface, and thus the hole extraction barrier must be located at the FTO/TaTm interface.

The PSC with  $\text{MoO}_x$  and TaTm as double HTL shows a  $V_{oc}$  similar to the TaTm HTL and a  $J_{sc}$  similar to the  $\text{MoO}_x$  HTL, indicating that FTO/TaTm interface and  $\text{MoO}_x$ /PVK interface were the bottleneck in the PSCs with single HTL. TaTm acts as an electron blocking layer and passivation layer for the  $\text{MoO}_x$  interface, whereas  $\text{MoO}_x$  improves the energy band alignment between the FTO and TaTm.

The PSC with  $\text{MoO}_x$  and TaTm as double HTL demonstrates lower  $V_{oc}$  and  $J_{sc}$  than the reference PSC with PTAA. The (TR)PL measurements also showed more interfacial recombination in the  $\text{MoO}_x$ /TaTm/PVK stack than in the PTAA/PVK stack, indicating more charge carrier extraction by PTAA.

Determine the influence of thickness of  $\text{MoO}_x$  and TaTm on device parameters

The influence of film thickness on atomic composition, stoichiometry and valence band energy of  $\text{MoO}_x$  was determined with XPS measurement. The  $\text{Mo}^{6+}/\text{Mo}^{5+}$  ratio increases with film thickness. The same trend was observed for Lattice Oxygen / Oxygen Vacancies ratio increasing with thickness, indicating that the  $\text{Mo}^{6+}$  correlates with lattice oxygen and  $\text{Mo}^{5+}$  correlates with oxygen vacancies. The stoichiometry determined by the XPS measurement showed an unrealistic value of 8.6 for the 2-nm thick  $\text{MoO}_x$ , which is caused due to the detection of oxygen-rich FTO. The stoichiometry values for 5-nm and 10-nm thick  $\text{MoO}_x$  were realistic, but the trend of decreasing stoichiometry with increasing thickness is in disagreement with the increase of  $\text{Mo}^{6+}/\text{Mo}^{5+}$  ratio and Lattice Oxygen / Oxygen Vacancies ratio. From the XPS measurement, it was also observed that the valence band energy with respect to the Fermi level decreases with thickness.

The influence of thickness of  $\text{MoO}_x$  and TaTm was tested on device level as single HTL. For  $\text{MoO}_x$ , a clear trend was observed where the  $V_{oc}$  increases with  $\text{MoO}_x$  thickness. The decrease of  $\text{Mo}^{5+}$  and oxygen vacancies in thicker  $\text{MoO}_x$  increases the work function and interface dipole, resulting in less interfacial recombination. For TaTm, the thickness showed no influence on the  $V_{oc}$  or FF.

The influence of thickness of  $\text{MoO}_x$  and TaTm was also tested on device level as double HTL. For thickness variation of  $\text{MoO}_x$  with 5-nm thick TaTm as double HTL, 2-nm thick  $\text{MoO}_x$  showed the highest  $V_{oc}$  and FF. The gap states of  $\text{Mo}^{5+}$  align with the VB of TaTm which improves the electron transfer from the FTO to the  $\text{MoO}_x$ /TaTm interface and therefore decreases the hole extraction barrier. For larger thicknesses of  $\text{MoO}_x$  between FTO and 5-nm thick TaTm, the same trend for single HTL  $\text{MoO}_x$  is observed in which  $V_{oc}$  increases with thickness. For thickness variation of TaTm on 5-nm thick  $\text{MoO}_x$ , it has been observed that the  $V_{oc}$  and FF increase with increasing thickness of TaTm. Due to the islanding of TaTm, the increasing thickness leads to better coverage of the TaTm on the  $\text{MoO}_x$ , resulting in improved electron blocking between the PVK and HTL.

In the end, the 2-nm thick  $\text{MoO}_x$  with 5-nm thick TaTm showed to be the most promising HTL. This PSC achieved a PCE of 4.73%, compared to a PCE of 12.28% for the reference PSC with PTAA. It has also been observed that the  $V_{oc}$  and  $J_{sc}$  are better for the PSC with PTAA than for the PSC with  $\text{MoO}_x$ /TaTm. Therefore, further investigation is needed to improve the PSC with  $\text{MoO}_x$ /TaTm before the thermally evaporated  $\text{MoO}_x$  and TaTm can replace the spincoated PTAA as HTL.

## 7.2. Recommendations

Below are several suggestions provided for further investigation of  $\text{MoO}_x$  and TaTm as double HTL in PSCs:

### Hole-only devices

Hole-only devices can tell more on the hole-injection of the electrode to the absorber layer. The hole-only devices are devices in which the ETL is replaced with another HTL. The current measurement when a voltage is applied on the device is only carrier by holes. The magnitude of the current is an indication of the hole-injection abilities. The current is highly sensitive to changes in the height of the barrier [89]. The J-V curve of hole-only devices can give more information on the hole-extraction abilities for varying thicknesses of  $\text{MoO}_x$  and TaTm.

### EIS & IMPS measurement

Resistances related to interfacial charge transport can be identified with electrical impedance spectroscopy (EIS). EIS can measure [61]:

- Charge transfer resistance: This represents a potential barrier to the flow of current at an interface, influencing the rate of charge transfer. The resistance,  $R_{ct}$ , is voltage-dependent, as voltage affects the width of the depletion region.
- Recombination resistance: This term refers to the process where electrons (or holes) are captured, transitioning from the conduction band (or valence band) to defects within the bandgap or surface states. The recombination resistance,  $R_{rec}$ , is influenced by carrier density, which varies with both the applied voltage and the intensity of illumination.
- Series resistance: This resistance accounts for the combined effects of contact resistance, wire resistance, and sheet resistance.

A method to determine the time rates of charge transfer, charge accumulation, and charge recombination is Intensity-modulated photocurrent spectroscopy (IMPS) measurements. Here, the occurrence of processes on different time scales can be separated in a relatively simple manner [152].

### Simulations

Simulations can be executed to give more insight on the changes in the band diagram when varying the film thickness of the  $\text{MoO}_x$  and TaTm to enhance transport selectivity. Such changes in the band diagram can be band bending at interfaces, shift in Fermi level, and the size of energy barriers for electrons in the CB and for holes in the VB [150]. Furthermore, the charge carrier density across the charge transport layers and absorber layer can be simulated. Meskini et Asgharizadeh used this method to determine when the bulk recombination is the dominant mechanism, and when it shifts to interfacial recombination being the dominant mechanism [123].

Using the experiments in this study, it is difficult to conclude which interface is responsible for the observed changes in the results, especially since the effects of multiple interfaces can interfere. Simulations can increase the understanding of specific interfaces, such as the  $\text{MoO}_x/\text{TaTm}$  interface. One of the many parameters that can be adjusted with the simulations related to the charge extraction is the defect density, the position of the defects, and the charge carrier cross-section area [59].

To further improve the device performance, the following suggestions can be explored:

#### Annealing of the HTLs

In this study, the only annealing during the device fabrication is done after the deposition of the perovskite. However, Babaei et al. researched the effect of annealing after  $\text{MoO}_x$  deposition compared to annealing after TaTm deposition [13]. They varied the annealing temperature ranging from  $60^\circ\text{C}$  to  $200^\circ\text{C}$  to determine its influence on the device parameters. It was found that annealing after TaTm deposition improved the FF and PCE, suggested as a result of improved ohmic contact at the  $\text{MoO}_3/\text{TaTm}$  interface. Although it was not shared how the device parameters without annealing of the HTLs compare to those with the annealing of the HTLs, it is possible that the annealing of HTLs after deposition can improve the device performance.

#### Interlayer between $\text{MoO}_x$ and TaTm

Similarly to the previous suggestion, Pérez-del-Rey et al improved the ohmic contact between the  $\text{MoO}_3$  and TaTm [142]. However, instead of annealing the HTLs, a 2-nm thin layer of wide bandgap TPBI is inserted in between  $\text{MoO}_3$  and TaTm. The performance of the devices with unannealed  $\text{MoO}_3$  and TPBI interlayer is similar to the devices with annealed  $\text{MoO}_3$ . It is hypothesized that the charge transport between the TPBI and  $\text{MoO}_3$  is facilitated due to a reaction of the TPBI with the  $\text{MoO}_3$  surface through an electron transfer. Other molecules such as TCTA and CBP were also used as interlayer and improved the device performance as well, but not to the extent of the TPBI interlayer. This is due to the smaller difference in IE of the CBP and TCTA with the HOMO level of the TaTm.

#### Using different HTMs

Another possibility is to replace one (or both) of the HTMs. For example, TaTm can possibly be replaced by other organic HTMs with similar energy levels that have reportedly been used with thermal evaporation, such as Spiro-TTB [168], Spiro-OMeTad [48], and NPB [48]. Similarly,  $\text{MoO}_x$  can be replaced by other thermally evaporated TMOs with a comparable high work function, such as  $\text{V}_2\text{O}_5$  [157] and  $\text{WO}_3$  [102]. However, TaTm has also been paired with other organic semiconductors [41], which have a work function more similar to TaTm than  $\text{MoO}_x$ . One of those organic HTMs is P3HT, which has reportedly also been used with thermal evaporation [90].

# Acknowledgements

This report contains the research I have been working on for the last months. When starting my masters two years ago, I could not have imagined that I would be working in a clean room and learn the process of fabricating solar cells. It has been great gaining new skills and broadening my knowledge.

First, I want to thank the Dr. Luana Mazzarella and Dr. Paul Procel Moya for their support and supervision during my thesis. Their feedback and suggestions for the research when encountering problems, as well as their feedback on the presentation and report were immensely valuable. I appreciate everything they have taught me.

I also want to thank Jin Yan for all her guidance and support during this project. From teaching me how to use the deposition machines in the clean room, to helping with measurements and carrying out the perovskite depositions. I really enjoyed working together.

Lastly, I want to thank Martijn Tijssen and Bernardus Zijlstra for all they do at the Perovskite Line and always being able to ask for their help. I also want to thank Bahiya Ibrahim for providing training for the measurement equipment in TNW.

*Jasmine Apawti  
Delft, September 2024*



# References

- [1] Abbas, H. A. et al. "High efficiency sequentially vapor grown n-i-p CH<sub>3</sub>NH<sub>3</sub>PbI<sub>3</sub> perovskite solar cells with undoped P3HT as p-type heterojunction layer". In: *APL Materials* 3.1 (2015), p. 16105.
- [2] Abdelmageed, G. et al. "Effect of temperature on light induced degradation in methylammonium lead iodide perovskite thin films and solar cells". In: *Solar Energy Materials and Solar Cells* 174 (2018), pp. 566–571.
- [3] Agrawal, S. *Rare-Earth-Activated Phosphors: Chemistry and Applications*. Elsevier eBooks, 2022. Chap. Spectroscopy techniques for rare-earth-activated phosphors, pp. 147–175.
- [4] Ahmed, S.F. et al. "Perovskite solar cells: Thermal and chemical stability improvement, and economic analysis". In: *Materials Today Chemistry* 27 (2023), p. 101284.
- [5] Apergi, S. et al. "Decomposition of organic perovskite precursors on MOO<sub>3</sub>: Role of halogen and surface defects". In: *ACS Applied Materials & Interfaces* 14.30 (2022), pp. 34208–34219.
- [6] Apex Instruments. *Spin Coating Technology*. 2016. URL: <https://www.apexicindia.com/technologies/spin-coating-technology>.
- [7] Ariel-Sternberg, N. *Tooling Factor Calibration Standard Operating Procedure*. 2000. URL: [https://static1.squarespace.com/static/57b26cc76b8f5b7524bf9ed2/t/592ef652d482e97b97d16866/1496249939947/ToolingFactorCalibration\\_CU\\_SOP\\_May2017.pdf](https://static1.squarespace.com/static/57b26cc76b8f5b7524bf9ed2/t/592ef652d482e97b97d16866/1496249939947/ToolingFactorCalibration_CU_SOP_May2017.pdf).
- [8] Arora, N. et al. "Perovskite solar cells with CuSCN hole extraction layers yield stabilized efficiencies greater than 20%". In: *Science* 358.6364 (2017), pp. 768–771.
- [9] Arumugam, G. M. et al. "Inorganic hole transport layers in inverted perovskite solar cells: A review". In: *Nano select* 2.6 (2021), pp. 1081–1116.
- [10] Al-Ashouri, A. et al. "Conformal monolayer contacts with lossless interfaces for perovskite single junction and monolithic tandem solar cells". In: *Energy & Environmental Science* 12.11 (2019), pp. 3356–3369.
- [11] Avila, J. et al. "Influence of doped charge transport layers on efficient perovskite solar cells". In: *Sustainable Energy & Fuels* 2.11 (2018), pp. 2429–2434.
- [12] Avila, J. et al. "Influence of doped charge transport layers on efficient perovskite solar cells". In: *Sustainable Energy & Fuels* 2.11 (2018), pp. 2429–2434.
- [13] Babaei, A. et al. "Efficient Vacuum Deposited P-I-N Perovskite Solar Cells by Front Contact Optimization". In: *Frontiers in Chemistry* 7 (2020).
- [14] Babaei, A. et al. "High voltage vacuum-processed perovskite solar cells with organic semiconducting interlayers". In: *Materials Advances* 10.11 (2020), pp. 6640–6646.
- [15] Babaei, A. et al. "Preparation and characterization of mixed halide MAPbI<sub>3</sub>-xCl<sub>x</sub> perovskite thin films by three-source vacuum deposition". In: *Energy Technology* 8.4 (2019).

- [16] Bae, S.-R., Heo, D.Y., and Kim, S.Y. "Recent progress of perovskite devices fabricated using thermal evaporation method: Perspective and outlook". In: *Materials Today Advances* 14 (2022), p. 100232.
- [17] Bae, S.R., Heo, D.Y., and Kim, S.Y. "Recent progress of perovskite devices fabricated using thermal evaporation method: Perspective and outlook". In: *Materials Today Advances* 14 (2022), p. 100232.
- [18] Ball, J. M. et al. "Low-temperature processed meso-superstructured to thin-film perovskite solar cells". In: *Energy & Environmental Science* 6.6 (2013), pp. 1739–1743.
- [19] Bashir, A. et al. *Chemistry of Nanomaterials: Fundamentals and Applications*. Elsevier eBooks, 2020. Chap. Interfaces and Surfaces, pp. 51–87.
- [20] Bhosle, V., Tiwari, A., and Narayan, J. "Epitaxial growth and properties of MoO<sub>x</sub> (2<x<2.75) films". In: *Journal of Applied Physics* 97.8 (2005).
- [21] Bhosle, V., Tiwari, A., and Narayan, J. "Epitaxial growth and properties of MoO<sub>x</sub>(2 x 2.75) films". In: *Journal of Applied Physics* 97.8 (2005).
- [22] Bhukya, R., Hampika, G., and Guduri, M. *Energy Systems, Drives and Automations - Proceedings of ESDA 2019*. 1st ed. Singapore: Springer Singapore, 2020. Chap. Resonant tunneling diodes: working and applications, pp. 187–192.
- [23] Bi, D. et al. "Effect of different hole transport materials on recombination in CH<sub>3</sub>NH<sub>3</sub>PbI<sub>3</sub> perovskite-sensitized mesoscopic solar cells". In: *The Journal of Physical Chemistry Letters* 4.9 (2013), pp. 1532–1536.
- [24] C.B.Honsberg and S.G.Bowden. *Types of Recombination*. 2019. URL: <https://www.pveducation.org/pvcdrom/pn-junctions/types-of-recombination>.
- [25] Canil, L. et al. "Tuning halide perovskite energy levels". In: *Energy & Environmental Science* 14.3 (2021), pp. 1429–1438.
- [26] Castrucci, J.S. et al. "Considerations for the physical vapor deposition of high molar mass organic compounds". In: *Vacuum* 109 (2014), pp. 26–33.
- [27] Chatterjee, S. and Pal, A. J. "Introducing Cu<sub>2</sub>O Thin Films as a Hole-Transport Layer in Efficient Planar Perovskite Solar Cell Structures". In: *The Journal of Physical Chemistry C* 120.3 (2016), pp. 1428–1437.
- [28] Chavhan, S. et al. "Organo-metal halide perovskite-based solar cells with CuSCN as the inorganic hole selective contact". In: *Journal of Materials Chemistry A* 2.32 (2014), pp. 12754–12760.
- [29] Chemistry LibreTexts. *X-ray Photoelectron Spectroscopy (XPS)*. 2019. URL: [https://chem.libretexts.org/Courses/Franklin\\_and\\_Marshall\\_College/Introduction\\_to\\_Materials\\_Characterization\\_\\_CHM\\_412\\_Collaborative\\_Text/Spectroscopy/X-ray\\_Photoelectron\\_Spectroscopy\\_\(XPS\)](https://chem.libretexts.org/Courses/Franklin_and_Marshall_College/Introduction_to_Materials_Characterization__CHM_412_Collaborative_Text/Spectroscopy/X-ray_Photoelectron_Spectroscopy_(XPS)).
- [30] Chen, L. et al. "Fabrication and Properties of High-efficiency Perovskite/PCBM Organic Solar Cells". In: *Nanoscale Research Letters* 10.312 (2015).
- [31] Cheng, H. et al. "Understanding and minimizing non-radiative recombination losses in perovskite light-emitting diodes". In: *Journal of Materials Chemistry C* 10.37 (2022), pp. 13590–13610.
- [32] Cheng, M. et al. "Charge-transport layer engineering in perovskite solar cells". In: *Science Bulletin* 65 (2020), pp. 1237–1241.

- [33] Christians, J. A., Fung, R. C. M., and Kamat, P. V. "An inorganic hole conductor for organo-lead halide perovskite solar cells. Improved hole conductivity with copper iodide". In: *Journal of the American Chemical Society* 136.2 (2014), pp. 758–764.
- [34] Correa-Baena, J. et al. "Promises and challenges of perovskite solar cells". In: *Science* 358.6364 (2017), pp. 739–744.
- [35] Cui, J. et al. "CH<sub>3</sub>NH<sub>3</sub>PbI<sub>3</sub>-based planar solar cells with magnetron-sputtered nickel oxide". In: *ACS Applied Materials & Interfaces* 6.24 (2014), pp. 22862–22870.
- [36] Dänekamp, B. et al. "Influence of hole transport material ionization energy on performance of perovskite solar cells". In: *Journal of Materials Chemistry C* 7.3 (2019), pp. 523–527.
- [37] Degani, M. et al. "23.7% Efficient inverted perovskite solar cells by dual interfacial modification". In: *Science Advances* 7.49 (2021).
- [38] Docampo, P. et al. "Efficient organometal trihalide perovskite planar-heterojunction solar cells on flexible polymer substrates". In: *Nature Communications* 4.1 (2013).
- [39] Dr. Eberl MBE-Komponenten. *Glossary Dual Filament*. 2024. URL: [https://www.mbe-komponenten.de/glossary/dual-filament-df\\_\\_111.php](https://www.mbe-komponenten.de/glossary/dual-filament-df__111.php) (visited on 2024).
- [40] Du, P. et al. "Thermal Evaporation for Halide Perovskite Optoelectronics: Fundamentals, Progress, and Outlook". In: *Advanced Optical Materials* 10.4 (2021), p. 2101770.
- [41] Du, T. et al. "Efficient, stable, and fully printed carbonelectrode perovskite solar cells enabled by hole-transporting bilayers". In: *Joule* 7.8 (2023), pp. 1920–1937.
- [42] EAG Laboratories. *Ultraviolet/Visible/Near Infrared Spectroscopy (UV/VIS/NIR)*. 2024. URL: <https://www.eag.com/techniques/spectroscopy/uv-vis-spectroscopy/>.
- [43] Edmund Optics. *Introduction to Polarization*. 2024. URL: <https://www.edmundoptics.com/knowledge-center/application-notes/optics/introduction-to-polarization/> (visited on 2024).
- [44] Eldin, A. H., Refaey, M., and Farghly, A. *A Review on Photovoltaic Solar Energy Technology and its Efficiency*. 2015. URL: [https://www.researchgate.net/publication/287792329\\_A\\_Review\\_on\\_Photovoltaic\\_Solar\\_Energy\\_Technology\\_and\\_its\\_Efficiency](https://www.researchgate.net/publication/287792329_A_Review_on_Photovoltaic_Solar_Energy_Technology_and_its_Efficiency).
- [45] Eperon, G. E. et al. "Morphological control for high performance, solution-processed planar heterojunction perovskite solar cells". In: *Advanced Functional Materials* 24.1 (2014), pp. 151–157.
- [46] Evincism. *The Quantum Tunneling Effect – How Does it Work?* 2011. URL: <https://evincism.com/how-does-quantum-tunneling-work/>.
- [47] Farag, A. et al. "Evaporated Self-Assembled Monolayer Hole Transport Layers: Lossless Interfaces in p-i-n Perovskite Solar Cells". In: *Advanced Energy Materials* 13.8 (2023).
- [48] Feleki, B.T. et al. "Thin thermally evaporated organic hole transport layers for reduced optical losses in Substrate-Configuration perovskite solar cells". In: *ACS Applied Energy Materials* 4.4 (2021), pp. 3033–3043.
- [49] Fluxim. *Characterization techniques for organic and perovskite solar cells*. 2024. URL: <https://www.fluxim.com/measurement-techniques-perovskite-solar-cells#Characterization%20techniques>.

- [50] Gharibzadeh, S. et al. "Two-step physical deposition of a compact CuI hole-transport layer and the formation of an interfacial species in perovskite solar cells". In: *ChemSusChem* 9.15 (2016).
- [51] Giacomo, F. Di et al. "High efficiency CH<sub>3</sub>NH<sub>3</sub>PbI<sub>3</sub>-xCl<sub>x</sub> perovskite solar cells with poly(3-hexylthiophene) hole transport layer". In: *Journal of Power Sources* 251.9 (2014), pp. 152–156.
- [52] Greiner, M. and Lu, Z.-H. "Thin-film metal oxides in organic semiconductor devices: their electronic structures, work functions and interfaces". In: *NPG Asia materials* 5.7 (2013), e55.
- [53] Greiner, M. et al. "Universal Energy-Level Alignment of Molecules on Metal Oxides". In: *Nature Materials* 11.1 (2011), pp. 76–81.
- [54] Greiner, M.T. and Lu, Z. "Thin-film metal oxides in organic semiconductor devices: their electronic structures, work functions and interfaces". In: *NPG Asia Materials* 5.7 (2013).
- [55] Greiner, M.T. et al. "Transition Metal Oxide Work Functions: The Influence of Cation Oxidation State and Oxygen Vacancies". In: *Advanced Functional Materials* 22.21 (2012), pp. 4557–4568.
- [56] Griffi, J. et al. "The Influence of MoO<sub>x</sub> Anode Stoichiometry on the Performance of Bulk Heterojunction Polymer Solar Cells". In: *Advanced Energy Materials* 3.7 (2013).
- [57] Gusain, A., Faria, R. M., and Miranda, P. B. "Polymer Solar Cells — Interfacial processes related to performance issues". In: *Frontiers in Chemistry* 7 (2019).
- [58] Han, B. et al. "Effect of post-annealing on the properties of thermally evaporated molybdenum oxide films: Interdependence of work function and oxygen to molybdenum ratio". In: *Materials Science in Semiconductor Processing* 75 (2018), pp. 166–172.
- [59] Haque, M. et al. "Study on the interface defects of eco-friendly perovskite solar cells". In: *Solar Energy* 247 (2022), pp. 96–108.
- [60] Harsha, K.S. Sree. *Principles of physical vapor deposition of thin films*. Elsevier, 2006.
- [61] Hauff, E. Von and Klotz, D. "Impedance spectroscopy for perovskite solar cells: characterisation, analysis, and diagnosis". In: *Journal of Materials Chemistry C* 10.2 (2022), pp. 742–761.
- [62] He, F. et al. "Characterization of sputtered MoO<sub>x</sub> thin films with different oxygen content and their application as back contact in CdTe solar cells". In: *Vacuum* 176 (2020), p. 109337.
- [63] Hellstrom, S.L. *Basic Models of Spin Coating*. 2007. URL: <http://large.stanford.edu/courses/2007/ph210/hellstrom1/>.
- [64] Heo, J. H. et al. "Efficient inorganic-organic hybrid heterojunction solar cells containing perovskite compound and polymeric hole conductors". In: *Nature Photonics* 7.6 (2013), pp. 486–491.
- [65] Horiba scientific. *Photoluminescence (PL) & Electroluminescence (EL)*. URL: <https://www.horiba.com/int/scientific/technologies/photoluminescence-pl/photoluminescence-pl-electroluminescence-el/>.
- [66] Hossain, K. et al. "Performance Analysis of Intermediate Band Solar Cell (IBSC)". In: *American Journal of Engineering Research* 4.8 (2015), pp. 145–156.
- [67] Hou, F. et al. "Efficient and stable planar heterojunction perovskite solar cells with an MoO<sub>3</sub>/PEDOT:PSS hole transporting layer". In: *Nanoscale* 7.21 (2015), pp. 9427–9432.

- [68] Hu, L. et al. "Sequential deposition of CH<sub>3</sub>NH<sub>3</sub>PbI<sub>3</sub> on planar NiO film for efficient planar perovskite solar cells". In: *ACS Photonics* 1.7 (2014), pp. 547–553.
- [69] Hu, Z. et al. "Effects of Heteroatom Substitution in Spiro-bifluorene Hole Transport Materials". In: *Chemical Science* 7.8 (2016), pp. 5007–5012.
- [70] Huang, J. et al. "Improving the efficiency and stability of inverted perovskite solar cells with dopamine-copolymerized PEDOT:PSS as a hole extraction layer". In: *Journal of Materials Chemistry A* 5.26 (2017), pp. 13817–13822.
- [71] IEA. *Renewable Energy Progress Tracker*. 2024. URL: <https://www.iea.org/data-and-statistics/data-tools/renewable-energy-progress-tracker>.
- [72] IEA. *Renewables*. 2024. URL: <https://www.iea.org/energy-system/renewables>.
- [73] IEA. *Solar PV*. 2024. URL: <https://www.iea.org/energy-system/renewables/solar-pv>.
- [74] Im, J. et al. "6.5% efficient perovskite quantum-dot-sensitized solar cell". In: *Nanoscale* 3.10 (2011), pp. 4088–4093.
- [75] Isikgor, F.H. et al. "Concurrent cationic and anionic perovskite defect passivation enables 27.4% perovskite/silicon tandems with suppression of halide segregation". In: *Joule* 5.6 (2021), pp. 1566–1586.
- [76] Ito, S. et al. "Carbon-double-bond-free printed solar cells from TiO<sub>2</sub>/CH<sub>3</sub>NH<sub>3</sub>PbI<sub>3</sub>/CuSCN/Au Structural control and photoaging effects". In: *ChemPhysChem* 15.6 (2014), pp. 1194–1200.
- [77] Jeng, J. et al. "CH<sub>3</sub>NH<sub>3</sub>PbI<sub>3</sub> Perovskite/Fullerene Planar-Heterojunction Hybrid Solar Cells". In: *Advanced Materials* 25.27 (2013), pp. 3727–3732.
- [78] Jeon, N. J. et al. "o-Methoxy Substituents in Spiro-OMeTAD for Efficient Inorganic-Organic Hybrid Perovskite Solar Cells". In: *Journal of the American Chemical Society* 136.22 (2014), pp. 7837–7840.
- [79] Ji, T. et al. "Charge transporting materials for perovskite solar cells". In: *Rare Metals* 40 (2021), pp. 2690–2711.
- [80] Jiang, Q. et al. "Surface reaction for efficient and stable inverted perovskite solar cells". In: *Nature* 611 (2022), pp. 278–283.
- [81] Jung, E. H. et al. "Efficient, stable and scalable perovskite solar cells using poly(3-hexylthiophene)". In: *Nature* 567.7749 (2019), pp. 511–515.
- [82] Jung, M. et al. "Thermal stability of CuSCN hole conductor-based perovskite solar cells". In: *ChemSusChem* 9.18 (2016), pp. 2592–2596.
- [83] Kajal, P., Ghosh, K., and Powar, S. "Manufacturing Techniques of Perovskite Solar Cells". In: *Energy, Environment, and Sustainability*. Springer, 2018, pp. 341–364.
- [84] Kanai, K. et al. "Electronic structure of anode interface with molybdenum oxide buffer layer". In: *Organic Electronics* 11.2 (2010), pp. 188–194.
- [85] Khadka, D. B. et al. "Exploring the effects of interfacial carrier transport layers on device performance and optoelectronic properties of planar perovskite solar cells". In: *Journal of Materials Chemistry C* 5.34 (2017), pp. 8819–8827.
- [86] Kim, J. et al. "Interfacial modification and defect passivation by the cross-linking interlayer for efficient and stable CuSCN-based perovskite solar cells". In: *ACS Applied Materials & Interfaces* 11.50 (2019), pp. 46818–46824.

- [87] Kimab, S.-K. et al. "Comparison of NiOx thin film deposited by spincoating or thermal evaporation for application as a hole transport layer of perovskite solar cells". In: *RSC Advances* 10.71 (2020), pp. 43847–43852.
- [88] Kojima, A. et al. "Organometal halide perovskites as visible-light sensitizers for photovoltaic cells". In: *Journal of the American Chemical Society* 131.17 (2009), pp. 6050–6051.
- [89] Kotadiya, N.B. et al. "Universal strategy for Ohmic hole injection into organic semiconductors with high ionization energies". In: *Nature Materials* 17.4 (2018), pp. 329–334.
- [90] Kovacic, P. et al. "Effect of side groups on the vacuum thermal evaporation of polythiophenes for organic electronics". In: *Organic Electronics* 13.4 (2012), pp. 687–696.
- [91] Kronik, L. and Shapira, Y. "Surface photovoltage phenomena: theory, experiment, and applications". In: *Surface Science Reports* 37.1-5 (1999), pp. 1–206.
- [92] Krüger, J. et al. "High efficiency solid-state photovoltaic device due to inhibition of interface charge recombination". In: *Energy & Environmental Science* 79.13 (2001), pp. 2085–2087.
- [93] Kumar, M. H. et al. "Flexible, low-temperature, solution processed ZnO-based perovskite solid state solar cells". In: *Chemical Communications* 49.94 (2013), pp. 11089–11091.
- [94] Kumari, N., Singh, S. K., and Kumar, S. "A comparative study in different materials used for solar photovoltaics technology". In: *Materials Today: Proceedings* 66.8 (2022), pp. 3522–3528.
- [95] Kumari, S. et al. "Structural and optical properties of thermally induced nanostructures in amorphous molybdenum oxide thin films". In: *Journal of Materials Science Materials in Electronics* 32.20 (2021), pp. 24990–24996.
- [96] Kurt J. Lesker company. *Material Parameters*. 2024. URL: <https://www.seas.upenn.edu/~nanosop/documents/Z-factoranddensity.pdf>.
- [97] Lee, M. M. et al. "Efficient Hybrid Solar Cells Based on Meso-Superstructured Organometal Halide Perovskites". In: *Science* 338.6107 (2012), pp. 643–647.
- [98] Li, D. et al. "Recent progress of inverted organic-inorganic halide perovskite solar cells". In: *Journal of Energy Chemistry* 79 (2023), pp. 168–191.
- [99] Li, D. et al. "Recent progress of inverted organic-inorganic halide perovskite solar cells". In: *Journal of Energy Chemistry* 79 (2023), pp. 168–191.
- [100] Li, L. et al. *Handbook of Modern Coating Technologies*. Elsevier, 2021, pp. 45–83.
- [101] Li, L. et al. "Recent advances of flexible perovskite solar cells". In: *Journal of energy chemistry* 27.3 (2018), pp. 673–689.
- [102] Li, S. et al. "Fabrication and characterization of WO<sub>3</sub> thin films on silicon surface by thermal evaporation". In: *Materials Letters* 195 (2017), pp. 213–216.
- [103] Li, X. et al. "Synergistic effect of high-performance perovskite solar cells with reduced hysteresis and improved stability by the introduction of NA-treated TiOs and spraying-deposited Cul as transport layers". In: *ACS Applied Materials & Interfaces* 9.47 (2017), pp. 41354–41362.
- [104] Li, Y. et al. "A simple synthesis method to prepare a molybdenum oxide hole-transporting layer for efficient polymer solar cells". In: *RSC Advances* 7.13 (2017), pp. 7890–7900.

- [105] Li, Z. et al. "Organometallic-functionalized interfaces for highly efficient inverted perovskite solar cells". In: *Science* 376.6591 (2022), pp. 416–420.
- [106] Li, Z. et al. "Scaling fabrication of perovskite solar cells". In: *Nature Reviews Materials* 3.4 (2018).
- [107] Liang, L. et al. "Efficient Perovskite Solar Cells by Reducing Interface-Mediated Recombination: a Bulky Amine Approach". In: *Advanced Energy Materials* 10.14 (2020).
- [108] Liu, D. and Kelly, T. L. "Perovskite solar cells with a planar heterojunction structure prepared using room-temperature solution processing techniques". In: *Nature Photonics* 8 (2014), pp. 133–138.
- [109] Liu, D. et al. "Improved Performance of Inverted Planar Perovskite Solar Cells with F4-TCNQ Doped PEDOT:PSS Hole Transport Layers". In: *Journal of Materials Chemistry A* 5.12 (2017), pp. 5701–5708.
- [110] Liu, H. et al. "pi-Conjugated small molecules enable efficient perovskite growth and charge-extraction for high-performance photovoltaic devices". In: *Journal of Power Sources* 448 (2020), p. 227420.
- [111] Liu, K. et al. "Upscaling perovskite solar cells via the ambient deposition of perovskite thin films". In: *Trends in Chemistry* 3.9 (2021), pp. 747–764.
- [112] Liu, P. et al. "Interfacial electronic structure at the CH<sub>3</sub>NH<sub>3</sub>PbI<sub>3</sub>/MoO<sub>x</sub> interface". In: *Applied Physics Letters* 106.19 (2015).
- [113] Liu, X. et al. "Organic–inorganic halide perovskite based solar cells – revolutionary progress in photovoltaics". In: *Inorganic Chemistry Frontiers* 2.4 (2015), pp. 315–335.
- [114] Liu, Y., Liu, Z., and Lee, E. "High-Performance Inverted Perovskite Solar Cells Using Polu(triarylamine) as Hole Transport Layer". In: *ACS Applied Energy Materials* 2.3 (2019), pp. 1932–1942.
- [115] Lopes, J. M. S., Neto, N. M. B., and Araujo, P. T. *Springer Handbook of Inorganic Photochemistry*. Springer, Cham, 2022. Chap. An Introduction to Steady-State and Time-Resolved Photoluminescence, pp. 131–144.
- [116] Ma, F. et al. "Developments of Highly Efficient Perovskite Solar Cells". In: *Accounts of Materials Research* 4.8 (2023), pp. 716–725.
- [117] Ma, Y. et al. "Recent progress in interfacial dipole engineering for perovskite solar cells". In: *Nano-Micro Letters* 15.1 (2023).
- [118] Madani, S. et al. "Simulation of Perovskite Solar Cells Using Molybdenum Oxide Thin Films as Interfacial Layer for Enhancing Device Performance". In: *Sustainable materials and technologies* 32 (2022).
- [119] Madhavan, V. E. et al. "Copper thiocyanate inorganic hole-transporting material for high-efficiency perovskite solar cells". In: *ACS Energy Letters* 1.6 (2016), pp. 1112–1117.
- [120] Madhavan, V. E. et al. "CuSCN as hole transport material with 3D/2D perovskite solar cells". In: *ACS Applied Energy Materials* 3.1 (2019), pp. 114–121.
- [121] Martín, V.C. et al. "Chromogenic MoO<sub>3</sub> thin films: thermo-, photo-, and electrochromic response to working pressure variation in rf reactive magnetron sputtering". In: *Journal of Materials Science Materials in Electronics* 29.18 (2018), pp. 15486–15495.
- [122] Mazzarella, L. et al. "Strategy to mitigate the dipole interfacial states in (i)a-Si:H/MoO<sub>x</sub> passivating contacts solar cells". In: *Progress in Photovoltaics: Research and Applications* 29.3 (2021), pp. 391–400.

- [123] Meskini, M. and Asgharizadeh, S. "Performance simulation of the perovskite solar cells with Ti3C2 MXene in the SnO2 electron transport layer". In: *Scientific Reports* 14.5723 (2024).
- [124] Met Office. *How is climate linked to extreme weather?* 2018. URL: <https://www.metoffice.gov.uk/weather/climate/climate-and-extreme-weather>.
- [125] Mogk, D. *X-Ray Photoelectron Spectroscopy*. 2021. URL: [https://serc.carleton.edu/msu\\_nanotech/methods/xps.html](https://serc.carleton.edu/msu_nanotech/methods/xps.html).
- [126] Mönch, W. *Semiconductor Surfaces and Interfaces*. 1st ed. Springer, 2001.
- [127] Morales-Luna, M. et al. "The evolution of the Mo5+ oxidation state in the thermochromic effect of MoO3 thin films deposited by rf magnetron sputtering". In: *Journal of Alloys and Compounds* 722 (2017), pp. 938–945.
- [128] Al-Muntaser, A. A., Nasher, M. A., and Makhlof, M. M. "Structural, electrical, and linear/nonlinear optical characteristics of thermally evaporated molybdenum oxide thin films". In: *Ceramics International* 48.6 (2022), pp. 8069–8080.
- [129] NASA Global Climate Change. *What is Climate Change?* 2023. URL: <https://climate.nasa.gov/what-is-climate-change/>.
- [130] Nejang, B. A. et al. "An inorganic hole conductor for organo-lead halide perovskite solar cells. Improved hole conductivity with copper iodide". In: *Scientific Reports* 6.1 (2016).
- [131] Nevin, A. et al. "Time-Resolved Photoluminescence Spectroscopy and Imaging: New approaches to the analysis of cultural heritage and its degradation". In: *Sensors* 14.4 (2014), pp. 6338–6355.
- [132] Nia, N. Yaghoobi et al. "A crystal engineering approach for scalable perovskite solar cells and module fabrication: a full out of glove box procedure". In: *Journal of Materials Chemistry A* 6.2 (2018), pp. 659–671.
- [133] NREL. *Best Research-Cell Efficiency Chart*. 2024. URL: <https://www.nrel.gov/pv/cell-efficiency.html>.
- [134] O'Sullivan, C.K. and Guilbault, G.G. "Commercial quartz crystal microbalances – theory and applications". In: *Biosensors and Bioelectronics* 14.8 (199), pp. 663–670.
- [135] Ogieglo, W. et al. "Spectroscopic Ellipsometry Analysis of a Thin Film Composite Membrane Consisting of Polysulfone on a Porous  $\alpha$ -Alumina Support". In: *ACS Applied Materials & Interfaces* 4.2 (2012), pp. 935–943.
- [136] Olthof, S. and Meerholz, K. "Substrate-dependent electronic structure and film formation of MAPbI3 perovskites". In: *Scientific Reports* 7.1 (2017), pp. 34208–34219.
- [137] Our World in Data. *Energy Mix*. 2020. URL: <https://ourworldindata.org/energy-mix> (visited on 2024).
- [138] Park, J. H. et al. "Efficient CH3NH3PbI3 perovskite solar cells employing nanstructured p-type NiO electrode formed by a pulsed laser deposition". In: *Advanced Materials* 27.27 (2015), pp. 4013–4019.
- [139] Park, N. and Zhu, K. "Scalable fabrication and coating methods for perovskite solar cells and solar modules". In: *Nature Reviews Materials* 5 (2020), pp. 333–350.
- [140] Pathipati, S. R., Shah, M. N., and Pan, X. "Interfacial engineering and down-conversion of ultraviolet light for efficient perovskite solar cells". In: *Solar Energy* 197 (2020), pp. 363–370.



- [141] Perez-del-Rey, D. et al. "Interfacial Modification for High-Efficiency Vapor-Phase-Deposited Perovskite Solar Cells Based on a Metal Oxide Buffer Layer". In: *The Journal of Physical Chemistry Letters* 9.5 (2018), pp. 1041–1046.
- [142] Pérez-del-Rey, D. et al. "Molecular Passivation of MoO<sub>3</sub>: Band Alignment and Protection of Charge Transport Layers in Vacuum-Deposited Perovskite Solar Cells". In: *Chemistry of Materials* 31.17 (2019), pp. 6945–6949.
- [143] Pham, H. D. et al. "Boosting inverted perovskite solar cell performance by using 9,9-bis(4-diphenylamineophenyl)fluorene functionalized with triphenylamine as a dopant-free hole transporting material". In: *Journal of Materials Chemistry A* 7.20 (2019), pp. 12517–12517.
- [144] Pham, H. D. et al. "Organic Interfacial Materials for Perovskite-based Optoelectronic Devices". In: *Energy & Environmental Science* 12.4 (2019), pp. 1177–1209.
- [145] Pham, H.D. et al. "All-Rounder Low-Cost Dopant-Free D<sub>A</sub>D Hole-Transporting materials for efficient indoor and outdoor performance of perovskite solar cells". In: *Advanced Electronic Materials* 6.4 (2020).
- [146] Physics and Radio Electronics. *Tunnel Diode*. 2015. URL: <https://www.physics-and-radio-electronics.com/electronic-devices-and-circuits/semiconductor-diodes/tunnel-diode-how-it-works.html>.
- [147] Plasmaterials. *Thermal Evaporation*. 2022. URL: <https://plasmaterials.com/thermal-evaporation/> (visited on 06/21/2022).
- [148] Ponce-Mosso, M. et al. "Enhanced photocatalytic activity of amorphous MoO<sub>3</sub> thin films deposited by rf reactive magnetron sputtering". In: *Catalysis Today* 349 (2020), pp. 150–158.
- [149] Prasad, R. *Analog and Digital Electronic Circuits - Fundamentals, Analysis, and Applications*. 1st ed. Switzerland: Springer Cham, 2021. Chap. p-n Junction Diode: A Basic Non-linear Device, pp. 355–456.
- [150] Procel, P. et al. "Theoretical evaluation of contact stack for high efficiency IBC-SHJ solar cells". In: *Solar Energy Materials & Solar Cells* 186 (2018), pp. 66–77.
- [151] Rao, H. et al. "A 19.0% efficiency achieved in CuOx-based inverted CH<sub>3</sub>NH<sub>3</sub>PbI<sub>3</sub>-xClx solar cells by an effective Cl doping method". In: *Nano Energy* 27 (2016), pp. 51–57.
- [152] Ravishankar, S. et al. "Intensity-Modulated Photocurrent Spectroscopy and Its Application to Perovskite Solar Cells". In: *The Journal of Physical Chemistry C* 123.41 (2019), pp. 24995–25014.
- [153] Rhode, R. *Global Temperature Report for 2020*. 2021. URL: <https://berkeleyearth.org/global-temperature-report-for-2020/>.
- [154] Roy, P. et al. "A review on perovskite solar cells: Evolution of architecture, fabrication techniques, commercialization issues and status". In: *Solar Energy* 198 (2020), pp. 665–688.
- [155] Ryu, S. et al. "Fabrication of metal-oxide-free CH<sub>3</sub>NH<sub>3</sub>PbI<sub>3</sub> perovskite solar cells processed at low temperature". In: *Journal of Materials Chemistry A* 3.7 (2015), pp. 3271–3275.
- [156] Saikia, D. et al. "Progress and challenges of halide perovskite-based solar cell- a brief review". In: *Materials Science in Semiconductor Processing* 150 (2022), p. 106953.
- [157] Santos, R. et al. "Thermoelectric properties of V<sub>2</sub>O<sub>5</sub> thin films deposited by thermal evaporation". In: *Applied Surface Science* 282 (2013), pp. 590–594.

- [158] Scanlon, D.O. et al. "Theoretical and Experimental Study of the Electronic Structures of MoO<sub>3</sub> and MoO<sub>2</sub>". In: *The Journal of Physical Chemistry C* 114.10 (2010), pp. 4636–4645.
- [159] Schulz, P. et al. "High-Work-Function Molybdenum Oxide Hole Extraction Contacts in Hybrid Organic–Inorganic Perovskite Solar Cells". In: *ACS Applied Materials & Interfaces* 8.46 (2016), 31491–31499.
- [160] Scirè, D. et al. "Characterization of the defect density states in MoO<sub>x</sub> for c-Si solar cell applications". In: *Solid-State Electronics* 185 (2021), p. 108135.
- [161] Seo, J. et al. "Benefits of Very Thin PCBM and LiF Layer for Solution-Processed P-I-N Perovskite Solar Cells". In: *Energy & Environmental Science* 7.8 (2014), pp. 2642–2646.
- [162] Seo, S. et al. "An ultra-thin, un-doped NiO hole transporting layer of highly efficient (16.4%) organic-inorganic hybrid perovskite solar cells". In: *Nanoscale* 8.22 (2016), pp. 11403–11412.
- [163] Seo, S. et al. "Atomic layer deposition for efficient and stable perovskite solar cells". In: *Chemical Communications* 55.17 (2019), pp. 2403–2416.
- [164] Sharaf, O.Z. and Orhan, M.F. "Concentrated photovoltaic thermal (CPVT) solar collector systems: Part I – Fundamentals, design considerations and current technologies". In: *Renewable and Sustainable Energy Reviews* 50 (2015), pp. 1500–1565.
- [165] Sharma, K. *X-ray Photoelectron Spectroscopy (XPS): Principle, Instrumentation, Applications, Advantages, Limitations*. 2023. URL: <https://scienceinfo.com/x-ray-photoelectron-spectroscopy/>.
- [166] Shi, Z. and Jayatissa, A. H. "Perovskites-Based Solar Cells: A Review of Recent Progress, Materials and Processing Methods". In: *Materials* 11.5 (2018), p. 729.
- [167] Shrestha, P. *UV-VIS Spectroscopy: Principle, parts, uses, limitations*. 2023. URL: <https://microbenotes.com/uv-vis-spectroscopy/>.
- [168] Sittinger, V. et al. "Complex refractive indices of Spiro-TTB and C60 for optical analysis of perovskite silicon tandem solar cells". In: *Optics Express* 30.21 (2022), pp. 37957–37970.
- [169] Smets, A. et al. *Solar energy: The physics and engineering of photovoltaic conversion, technologies and systems*. 1st ed. Delft, The Netherlands: UIT Cambridge, 2016.
- [170] Smirnov, Y. et al. "Wafer-scale pulsed laser deposition of ITO for solar cells: reduced damage vs. interfacial resistance". In: *Materials Advances* 3.8 (2022), pp. 3469–3478.
- [171] Soltanpoor, W. et al. "Hybrid vapor-solution sequentially deposited mixed-halide perovskite solar cells". In: *ACS Applied Energy Materials* 3.9 (2020), pp. 8257–8265.
- [172] Srivastava, A. *Nanoscience and Nanotechnology II*. eBooks, 2018. Chap. Photoluminescence (PL) Spectra.
- [173] Stevie, F.A. and Donley, C.L. "Introduction to X-ray Photoelectron spectroscopy". In: *Journal of Vacuum Science & Technology A Vacuum Surfaces and Films* 38.6 (2020).
- [174] Subbak, M. "Advances in solar photovoltaics: technology review and patent trends". In: *Renewable and Sustainable Energy Reviews* 115 (2019), p. 109383.
- [175] Sun, W. et al. "High-performance inverted planar heterojunction perovskite solar cells based on solution-processed CuO<sub>x</sub> hole transport layer". In: *Nanoscale* 8.20 (2016), pp. 10806–10813.

- [176] Susic, I. et al. "Intrinsic Organic Semiconductors as Hole Transport Layers in p-i-n Perovskite Solar Cells". In: *Solar RRL* 6.4 (2021).
- [177] Susic, I. et al. "Intrinsic Organic Semiconductors as Hole Transport Layers in p-i-n Perovskite Solar Cells". In: *Solar RRL* 6.4 (2022).
- [178] Swartwout, R., Hoerantner, M. T., and Bulovic, V. "Scalable deposition methods for large-area production of perovskite thin film". In: *Energy & Environmental Materials* 2.2 (2019), pp. 119–145.
- [179] Teixeira, C. O. et al. "Selection of the ultimate perovskite solar cell materials and fabrication processes towards its industrialization: A review". In: *Energy Science & Engineering* 10.4 (2022), pp. 1478–1525.
- [180] *The Basics of UV-Vis Spectrophotometry*. United States of America: Agilent Technologies, 2021.
- [181] The United Nations Framework Convention on Climate Change (UNFCCC). *The Paris Agreement*. URL: <https://unfccc.int/process-and-meetings/the-paris-agreement>.
- [182] Tom, J. *UV-VIS Spectroscopy: principle, strengths and limitations and applications*. 2021. URL: <https://www.technologynetworks.com/analysis/articles/uv-vis-spectroscopy-principle-strengths-and-limitations-and-applications-349865>.
- [183] Tompkins, H. G. and Irene, E. A. *Handbook of Ellipsometry*. 1st ed. Norwich, New York: William Andrew, 2005.
- [184] Tong, X. et al. "High performance perovskite based solar cells". In: *Advanced Science* 3.5 (2016).
- [185] Vaynzof, Y. "The Future of Perovskite Photovoltaics—Thermal Evaporation or Solution Processing?" In: *Advanced Energy Materials* 10.48 (2020), pp. 1478–1525.
- [186] Wang, B. et al. "Solution-processable cathode buffer layer for high-performance ITO/CuSCN-based planar heterojunction perovskite solar cell". In: *Electrochimica Acta* 218 (2016), pp. 263–270.
- [187] Wang, F. et al. "Interface dipole induced Field Effect passivation for achieving 21.7% efficiency and stable perovskite solar cells". In: *Advanced Functional Materials* 31.5 (2020).
- [188] Wang, H. et al. "Efficient and stable inverted planar perovskite solar cells employing CuI as hole-transporting layer prepared by solid-gas transformation". In: *Energy Technology* 5.10 (2017), pp. 1836–1843.
- [189] Wang, H. et al. "One plus one greater than two: high-performance inverted planar perovskite solar cells based on composite CuI/CuSCN hole transporting layer". In: *Journal of Materials Chemistry A* 6.43 (2018), pp. 21435–21444.
- [190] Wen, Y., Tang, Y., and Yan, G. "Large grain size CH<sub>3</sub>NH<sub>3</sub>PbI<sub>3</sub> film for perovskite solar cells with hydroic acid additive". In: *AIP Advances* 8.9 (2018).
- [191] Wijeyasinghe, N. et al. "Copper (i) thiocyanate (CuSCN) hole-transporting layers processed from aqueous precursor solutions and their application in thin-film transistors and highly efficient organic and organometal halide perovskite solar cells". In: *Advanced Functional Materials* 27.35 (2017).

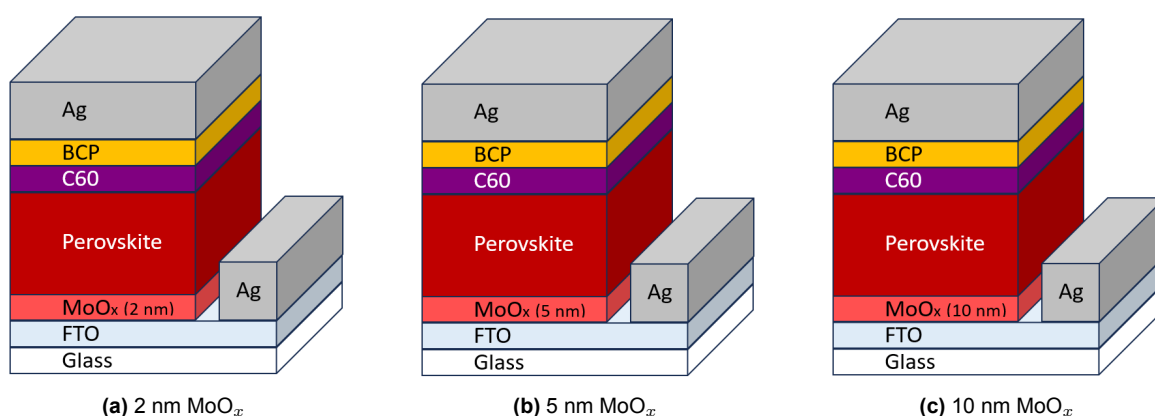
- [192] Wu, C. et al. "Electronic and chemical properties of molybdenum oxide doped hole injection layers in organic light emitting diodes". In: *Journal of Applied Physics* 105.3 (2009).
- [193] Xia, X. et al. "Lithium and silver co-doped nickel oxide hole-transporting layer boosting the efficiency and stability of inverted planar perovskite solar cells". In: *ACS Applied Materials & Interfaces* 10.51 (2018), pp. 44501–44510.
- [194] Xu, C. Y. et al. "Coordinated optical matching of a texture interface made from demixing blended polymers for high-performance inverted perovskite solar cells". In: *ACS Nano* 14.1 (2020), pp. 196–203.
- [195] Yan, J. et al. "Crystallization Process for High-Quality Cs<sub>0.15</sub>FA<sub>0.85</sub>PbI<sub>2.85</sub>Br<sub>0.15</sub> Film Deposited via Simplified Sequential Vacuum Evaporation". In: *ACS Applied Energy Materials* 6.20 (2023), pp. 10265–10273.
- [196] Yang, F. et al. "Periodic island-layer-island growth during deposition of ultrastable metallic glasses". In: *Communications Materials* 2.1 (2021).
- [197] Yang, I. et al. "Formation of pristine CuSCN layer by spray deposition method for efficient perovskite solar cell with extended stability". In: *Nano Energy* 32 (2017), pp. 414–421.
- [198] Ye, S. et al. "CuSCN-based inverted planar perovskite solar cell with an average PCE of 15.6%". In: *Nano Letters* 15.6 (2015), pp. 3723–3728.
- [199] Yi, Z. et al. "Will organic–inorganic hybrid halide lead perovskites be eliminated from optoelectronic applications?" In: *Nanoscale Advances* 1.4 (2019), pp. 1276–1289.
- [200] Yilbas, B.S., Al-Sharafi, A., and Ali, H. *Self-Cleaning of Surfaces and Water Droplet Mobility*. Elsevier eBooks, 2019. Chap. Surfaces for Self-Cleaning, pp. 45–98.
- [201] You, J. et al. "Low-Temperature Solution-Processed Perovskite Solar Cells with High Efficiency and Flexibility". In: *ACS Nano* 8.2 (2014), pp. 1674–1680.
- [202] Yu, W. et al. "Ultrathin Cu<sub>2</sub>O as an efficient inorganic hole transporting material for perovskite solar cells". In: *Nanoscale* 8.11 (2016), pp. 6173–6179.
- [203] Yurgens, A. *Lab Demo: Physical Evaporation of Metals*. 2004. URL: [https://fy.chalmers.se/~yurgens/FKA196/lab%5C%20exercises/PM\\_PVD.pdf](https://fy.chalmers.se/~yurgens/FKA196/lab%5C%20exercises/PM_PVD.pdf).
- [204] Zanoni, K. P. S. et al. "ITO top-electrodes via industrial-scale PLD for efficient buffer-layer-free semitransparent perovskite solar cells". In: *Advanced Materials Technologies* 7.10 (2022).
- [205] Zanoni, K.P.S. et al. "Tin(IV) Oxide Electron Transport Layer via Industrial-Scale Pulsed Laser Deposition for Planar Perovskite Solar Cells". In: *ACS Applied Materials & Interfaces* 15.27 (2023), pp. 32621–32628.
- [206] Zhang, S. et al. "Interface engineering of solution-processed hybrid organohalide perovskite solar cells". In: *ACS Applied Materials & Interfaces* 10.25 (2018), pp. 21681–21687.
- [207] Zhang, Z. et al. "Impact of Oxygen Vacancy on Energy-Level Alignment at MoO<sub>x</sub>/Organic Interfaces". In: *Applied physics express* 6.9 (2013), p. 095701.
- [208] Zhang, Z. et al. "Impact of oxygen vacancy on Energy-Level alignment at MOOX/Organic interfaces". In: *Applied Physics Express* 6.9 (2013).
- [209] Zhang, Z. et al. "Revealing the nitridation effects on GAN surface by First-Principles calculation and X-Ray/Ultraviolet photoemission spectroscopy". In: *IEEE Transactions on Electron Devices* 64.10 (2017), pp. 4036–4043.

- 
- [210] Zhang, Z. et al. "Understanding Hole Extraction of Inverted Perovskite Solar Cells". In: *ACS Applied Materials & Interfaces* 12.50 (2020), pp. 56068–56075.
- [211] Zhanga, B. et al. "Electrical properties of conductive Ge nanocrystal thin films fabricated by low temperature in situ growth". In: *Nanotechnology* 22.12 (2011), p. 125204.
- [212] Zhao, K. et al. "Solution-processed inorganic copper (i) thiocyanate (CuSCN) hole transporting layers for efficient p-i-n perovskite solar cells". In: *Journal of Materials Chemistry A* 3.41 (2015), pp. 20554–20559.
- [213] Zuo, C. and Ding, L. "Solution-Processed Cu<sub>2</sub>O and CuO as Hole Transport Materials for Efficient Perovskite Solar Cells". In: *Small* 11.41 (2015), pp. 5528–5532.
- [214] Zuo, C. et al. "Advances in Perovskite Solar Cells". In: *Advanced Science* 3.7 (2016).

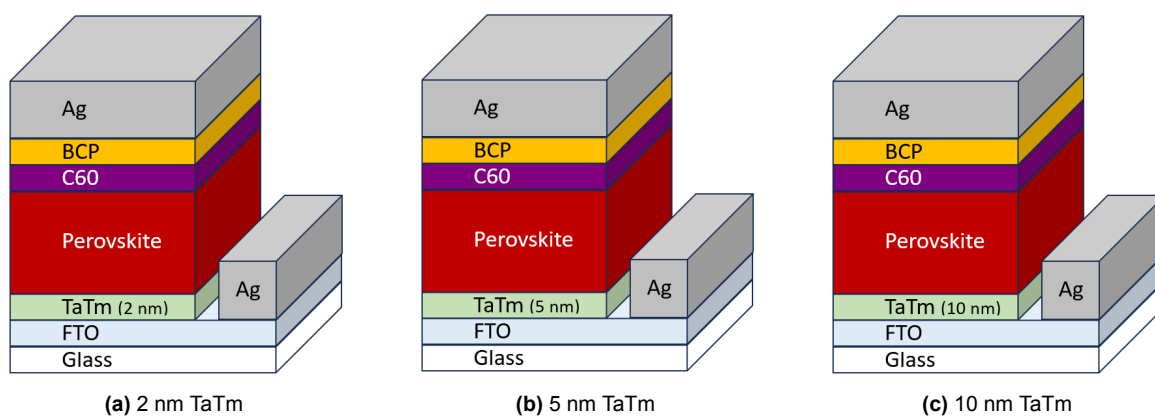
# A

## Fabricated devices for thickness optimization

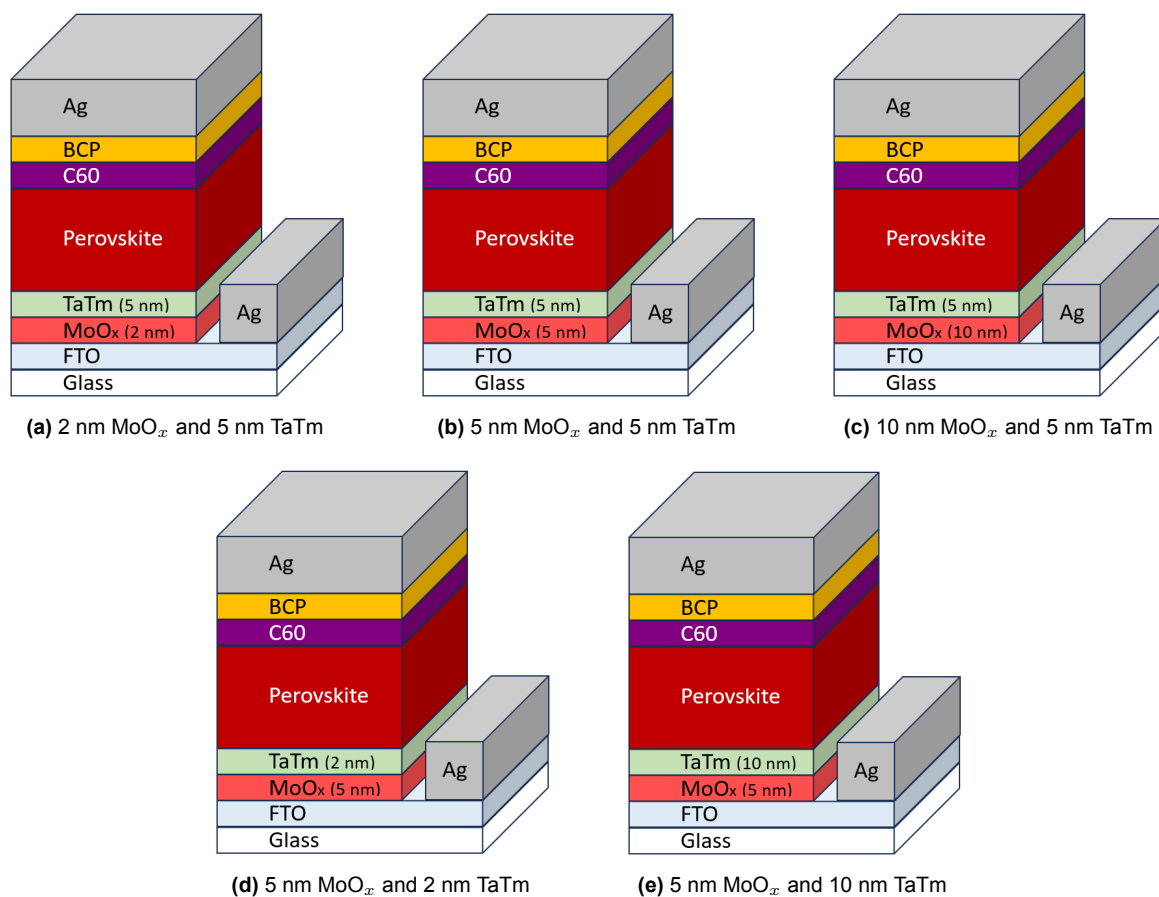
A schematic of the devices fabricated for the thickness optimization are shown below.



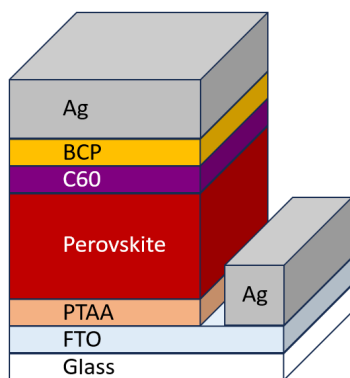
**Figure A.1:** Devices with MoO<sub>x</sub> as single HTL



**Figure A.2:** Devices with TaTm as single HTL



**Figure A.3:** Devices with MoO<sub>x</sub> and TaTm as double HTL



**Figure A.4:** Reference cell with PTAA

# B

## Device fabrication

### B.1. Z-ratio calculation

Z-ratio calculation manual [96]:

1. Deposit the material until the crystal life is either near 50% or end of life.
2. Place a unused substrate next to the used QCM.
3. Deposit 100 to 500 nm of material on the substrate.
4. Measure the actual film thickness on the substrate by forx example using a profilometer or iterferometer.
5. Correct the thickness reading that is shown by adjusting the Z-factor of the instrument.

### B.2. Data sheet information of ITO and FTO

\*\* To be added \*\*

### B.3. Recipes of thermal evaporated films

**Table B.1:** Recipe parameters for the thermally evaporated films.

Parameters	HTL		PVK				ETL		electrode
	MoO <sub>x</sub>	TaTm	PbCl <sub>2</sub>	CsBr	PbI <sub>2</sub>	FAI	C60	BCP	Ag
Idle setpoint (°C)	450	230	230	265	190	130	380	70	16%
Idle soak (MM:SS)	00:30	00:30	00:30	00:30	01:00	01:00	00:30	00:10	01:00
Ramp setpoint (°C)	450	240	250	295	220	160	400	75	24%
Ramp rate (K/min)	20	10	10	20	10	3	10	5	4 %/min
Ramp soak (MM:SS)	00:30	00:00	01:00	00:30	01:00	10:00	01:00	00:10	01:00
Capture (%)	25	20	25	35	25	35	20	30	30
Capture time (MM:SS)	00:30	00:00	03:00	01:00	01:00	00:00	00:30	00:40	00:20
Density (gram/cm <sup>3</sup> )	4.69	1.26	5.85	4.44	6.66	2.31	1.60	1.20	10.50
P rate	20.0	20.0	20.0	10.0	15.0	10.0	20.0	20.0	20.0
I rate (s)	0.9	0.9	0.9	0.9	0.9	0.9	2.0	0.9	2.0
D rate (s)	0.0	0.0	0.0	0.0	0.0	0.0	0.0	0.0	0.0



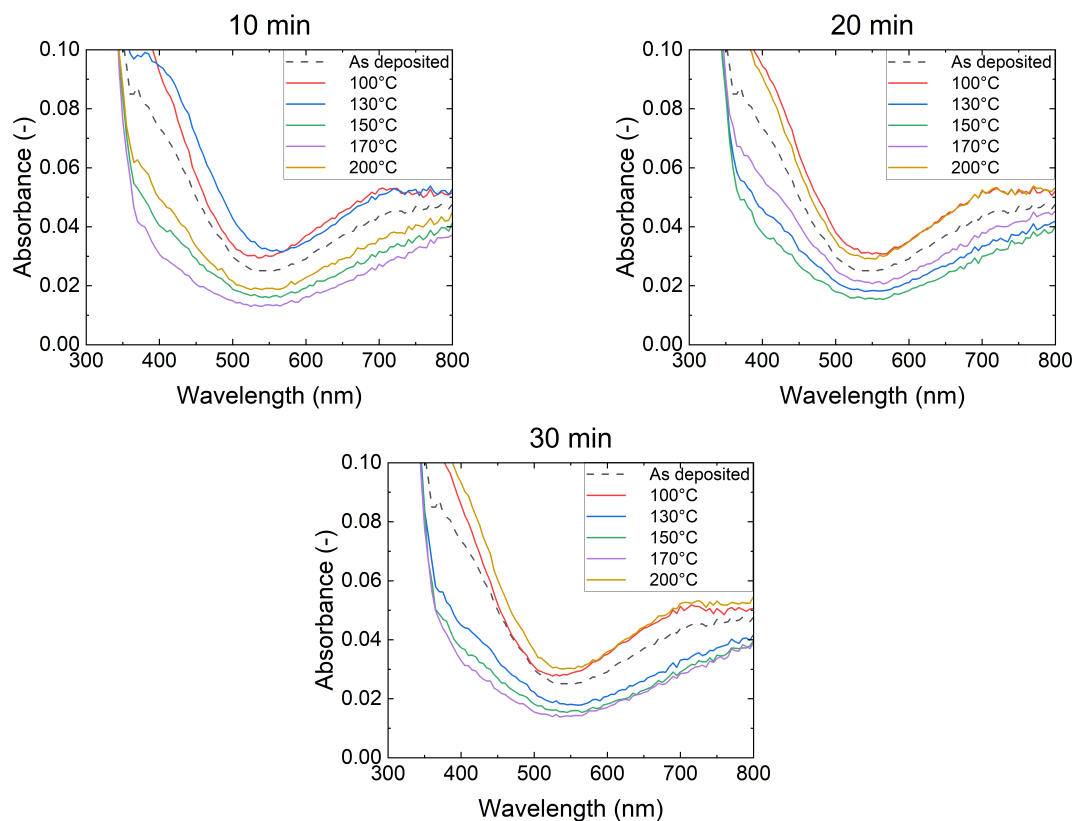
**Table B.2:** QCM-detected thickness and deposition rate for each source material of the three round single-layer deposition of PVK.

First round		
Source material	Thickness (Å)	Rate (Å/s)
PbI <sub>2</sub>	268.8	2.0
PbCl <sub>2</sub>	5.0	0.4
FAI	539.0	2.0
CsBr	6.0	0.1
Second round		
Source material	Thickness (Å)	Rate (Å/s)
PbI <sub>2</sub>	361.5	2.0
PbCl <sub>2</sub>	5.0	0.1
FAI	515.0	2.0
CsBr	9.0	0.1
Third round		
Source material	Thickness (Å)	Rate (Å/s)
PbI <sub>2</sub>	361.5	2.0
PbCl <sub>2</sub>	5.0	0.1
FAI	539.0	2.0
CsBr	9.0	0.1

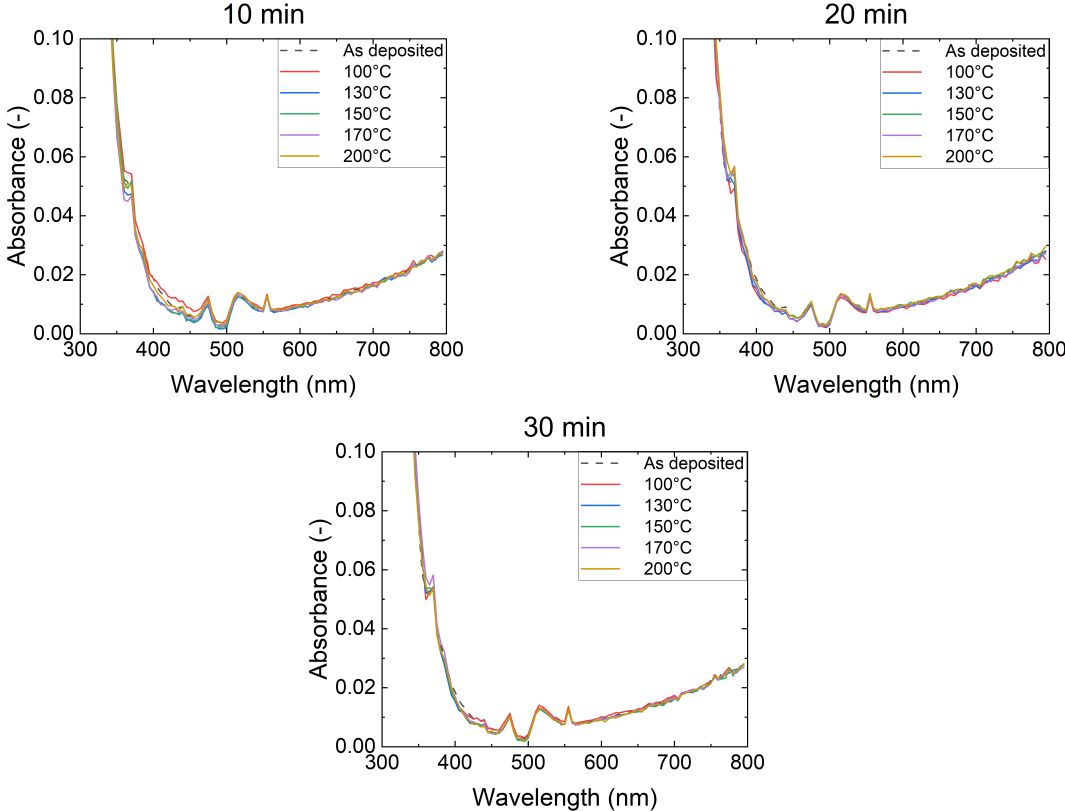
# Results of thermal stability for optical properties

All the absorbance and transmittance spectra for the tested annealing conditions are presented below.

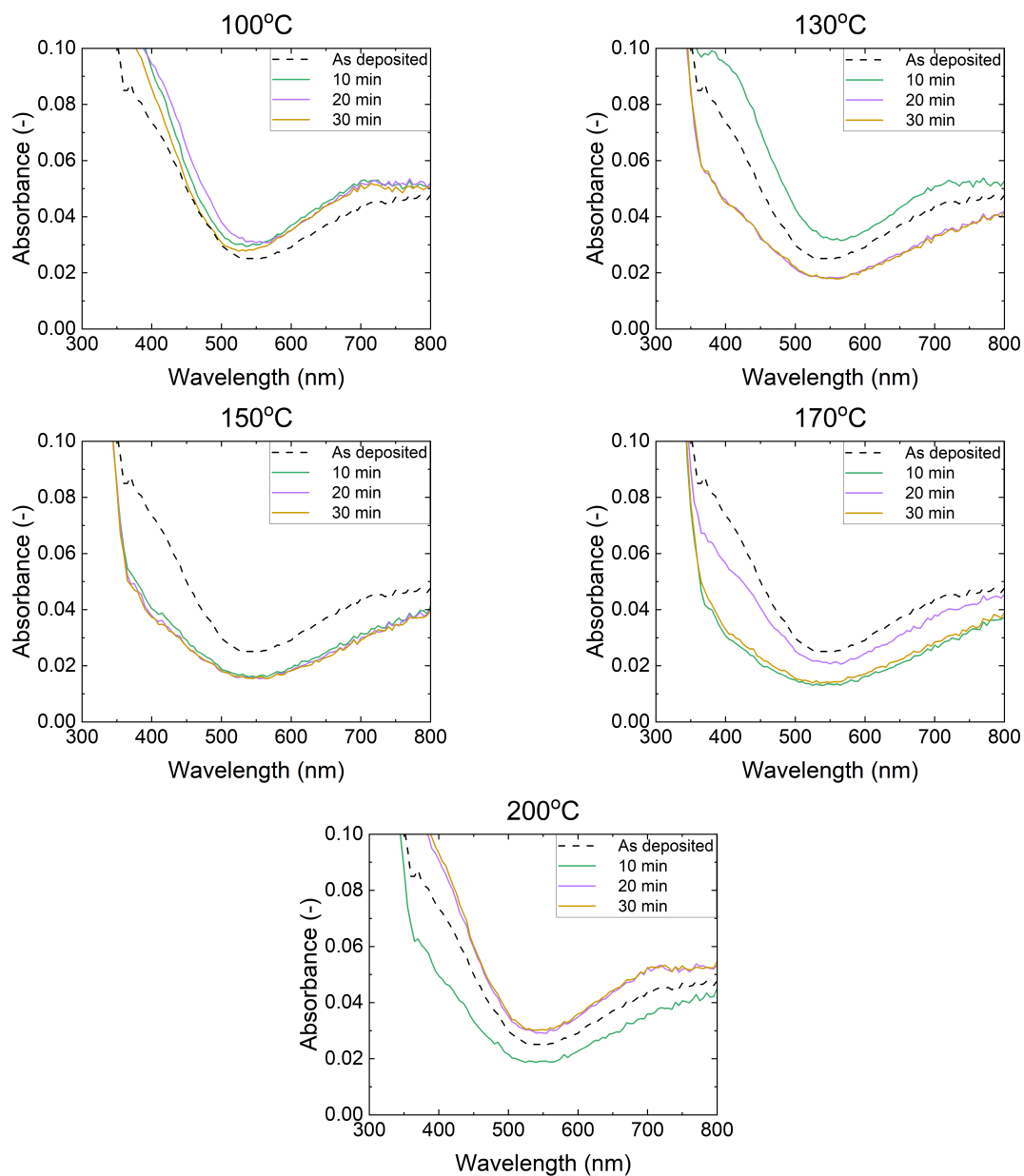
## C.1. Absorbance



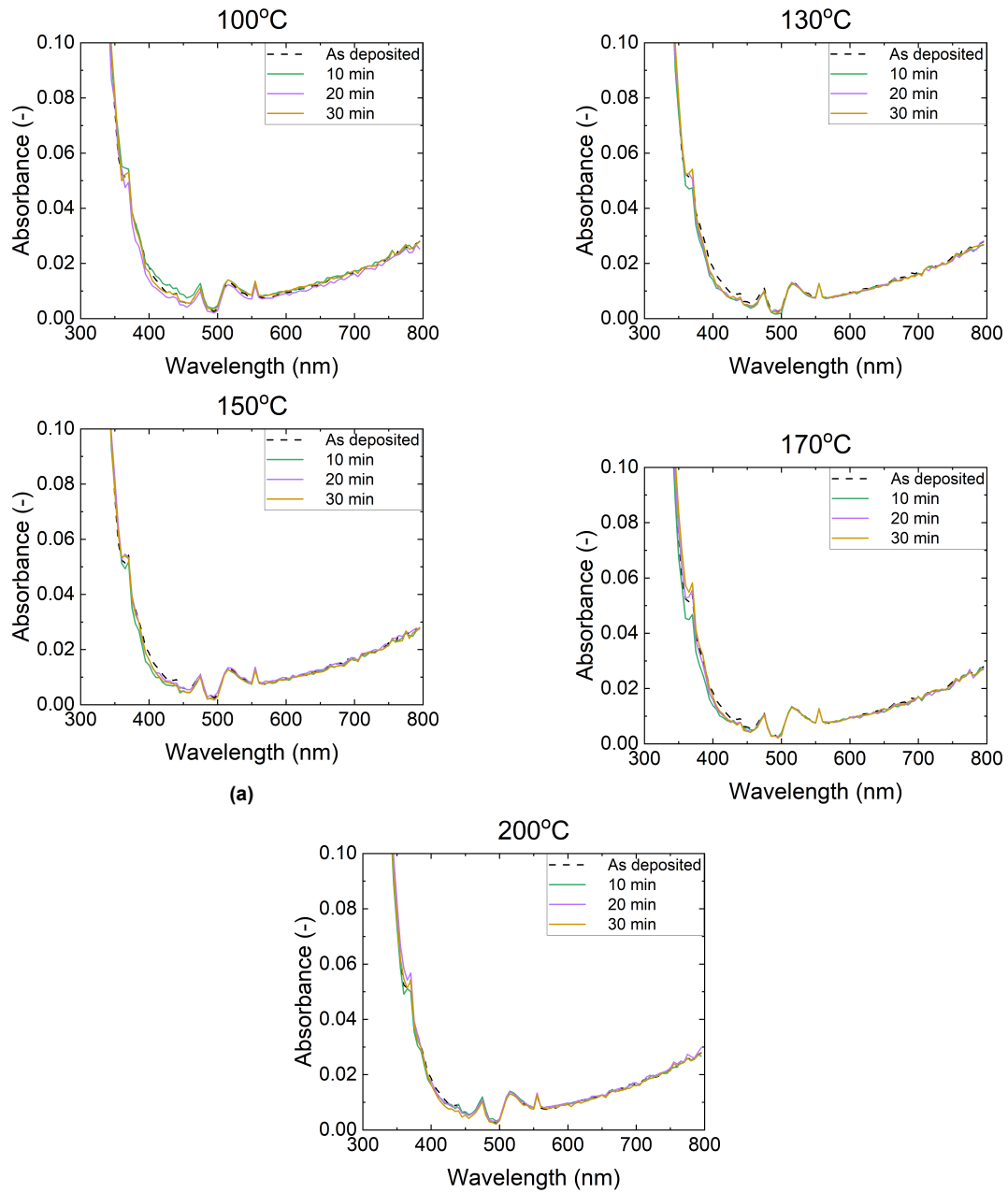
**Figure C.1:** Absorbance spectra for  $\text{MoO}_x$  after annealing at temperatures from 100°C to 200°C for 10, 20, and 30 minutes



**Figure C.2:** Absorbance spectra for TaTm after annealing at temperatures from 100°C to 200°C for 10, 20, and 30 minutes

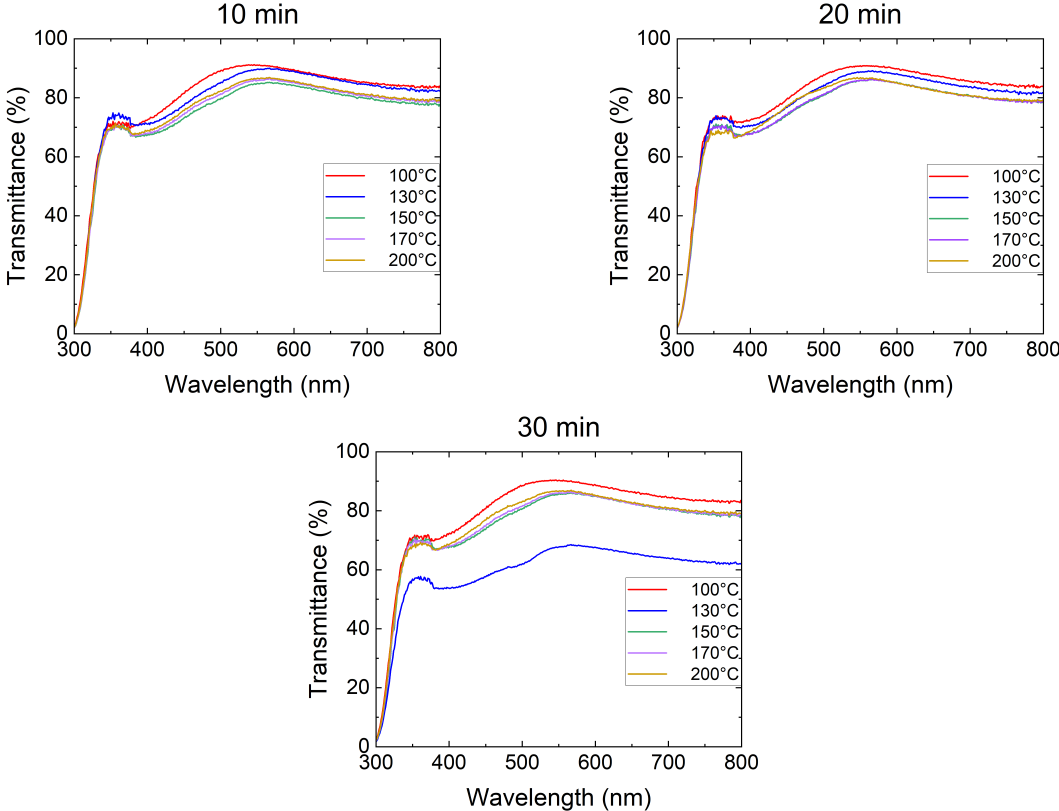


**Figure C.3:** Absorbance spectra for  $\text{MoO}_x$  after annealing for 10 to 30 minutes at temperatures 100°C, 130°C, 150°C, 170°C, and 200°C.

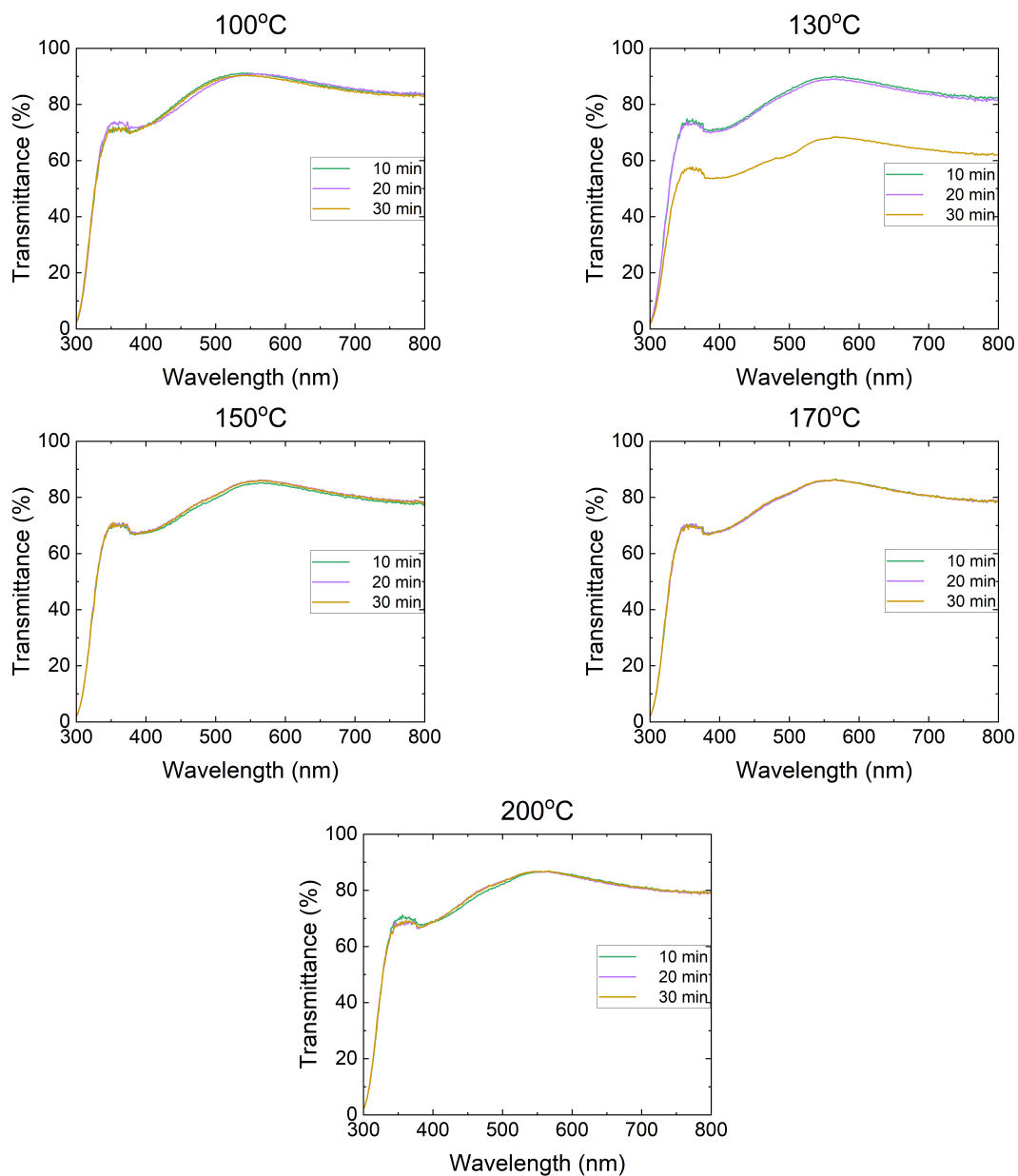


**Figure C.4:** Absorbance spectra for TaTm after annealing for 10 to 30 minutes at temperatures 100°C, 130°C, 150°C, 170°C, and 200°C.

### C.2. Transmittance



**Figure C.5:** Transmittance spectra for MoO<sub>x</sub> after annealing at temperatures from 100°C to 200°C for 10, 20, and 30 minutes



**Figure C.6:** Transmittance spectra for  $\text{MoO}_x$  after annealing for 10 to 30 minutes at temperatures 100°C, 130°C, 150°C, 170°C, and 200°C.

# D

## TRPL

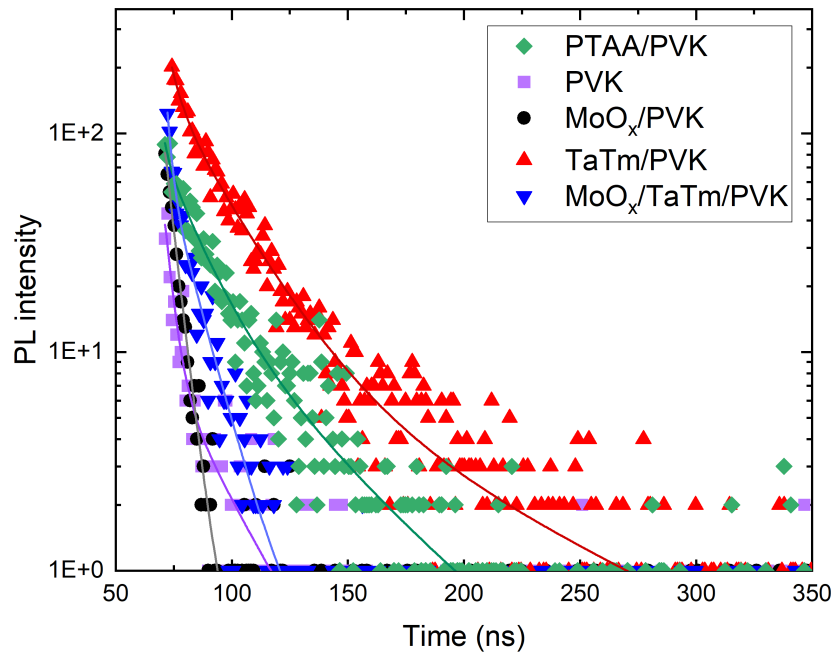


Figure D.1: Exponential fit of the TRPL graphs.

Table D.1: Exponential fitting parameters retrieved from Figure D.1.

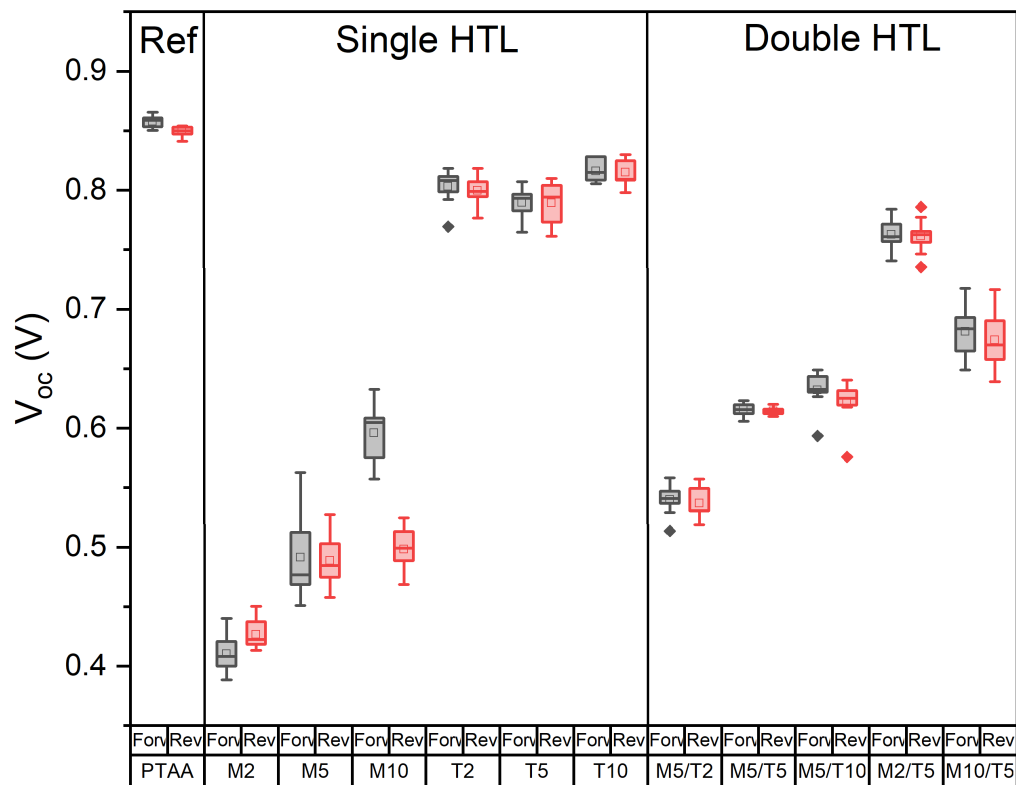
Lifetime = $(t1 \cdot A1 + t2 \cdot A2 + t3 \cdot A3)/(A1 + A2 + A3)$					
	PVK	MoO <sub>x</sub> /PVK	MoO <sub>x</sub> /TaTm/PVK	PTAA/PVK	TaTm/PVK
A1	23.140	111.621	67.053	15.249	60.738
A2	6.898	1824.893	135.719	56.216	126.048
A3	8.067	12.414	0.481	19.193	11.253
t1	3.485	4.265	10.872	2.167	4.289
t2	3.487	0.240	2.050	13.754	21.679
t3	20.581	7.441	386.400	40.655	79.305
<b>Lifetime (ns)</b>	<b>7.105</b>	<b>0.516</b>	<b>5.869</b>	<b>17.500</b>	<b>19.620</b>



# E

## Device parameters for thickness optimization

Boxplots of device parameters for all devices from the thickness optimization are shown below.



**Figure E.1:**  $V_{oc}$  of all devices from the thickness optimization.

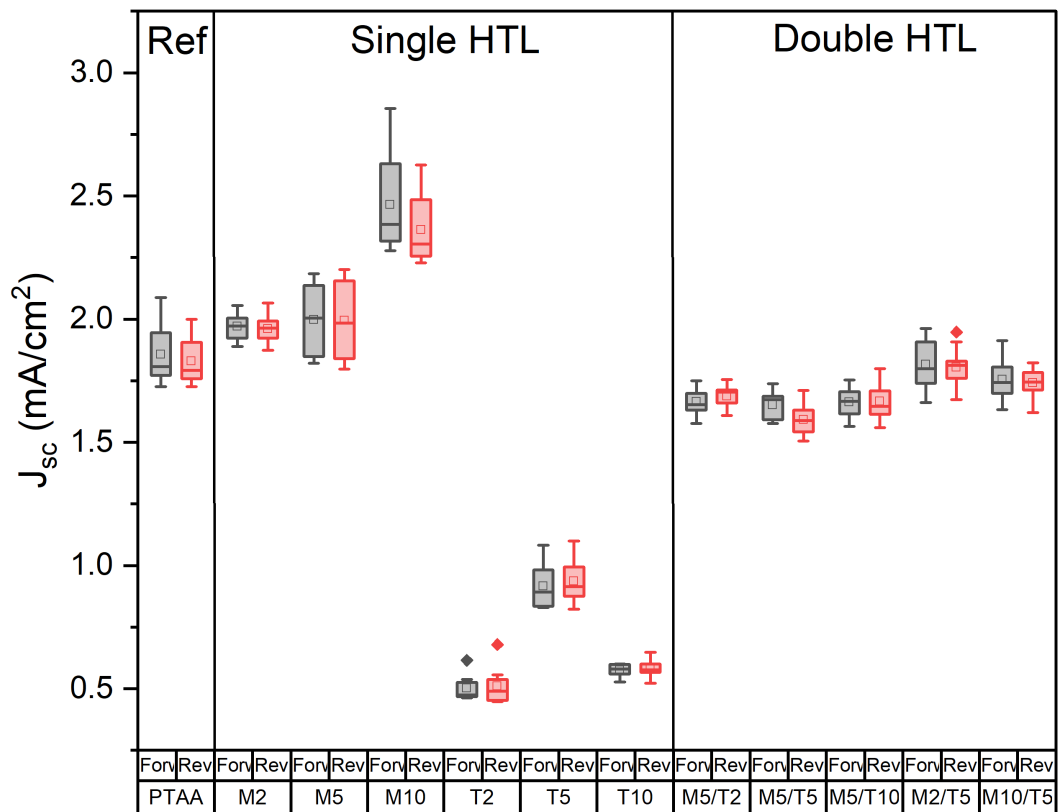


Figure E.2:  $J_{sc}$  of all devices from the thickness optimization.

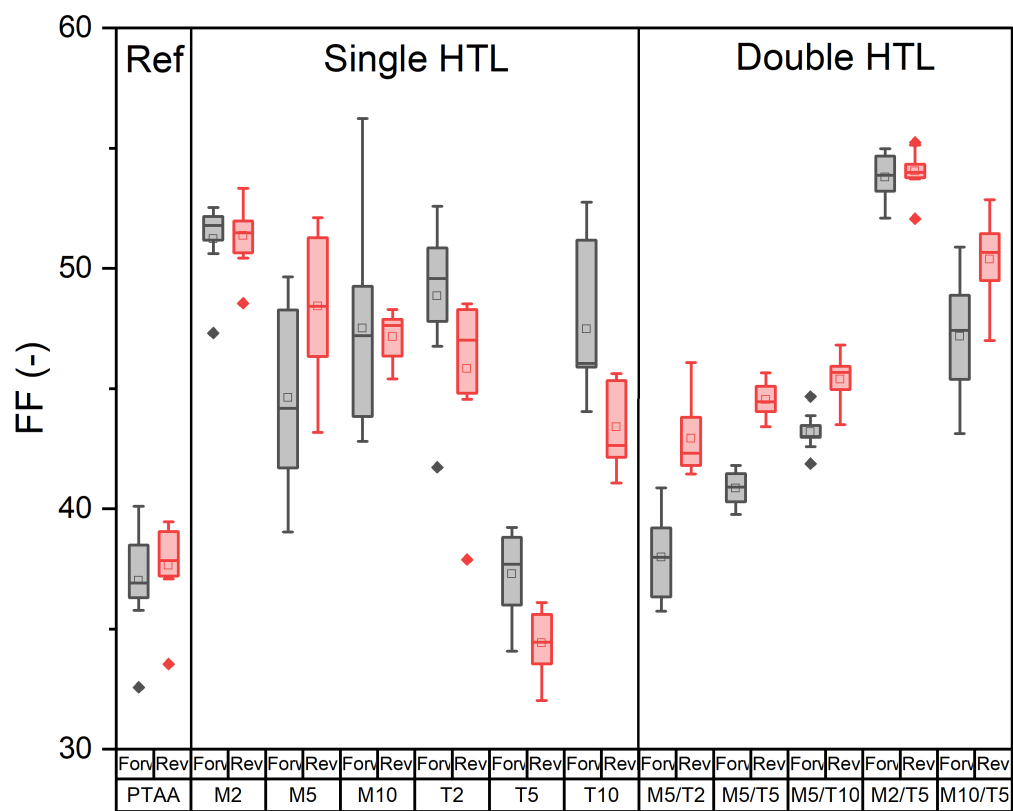


Figure E.3: Fill factor of all devices from the thickness optimization.

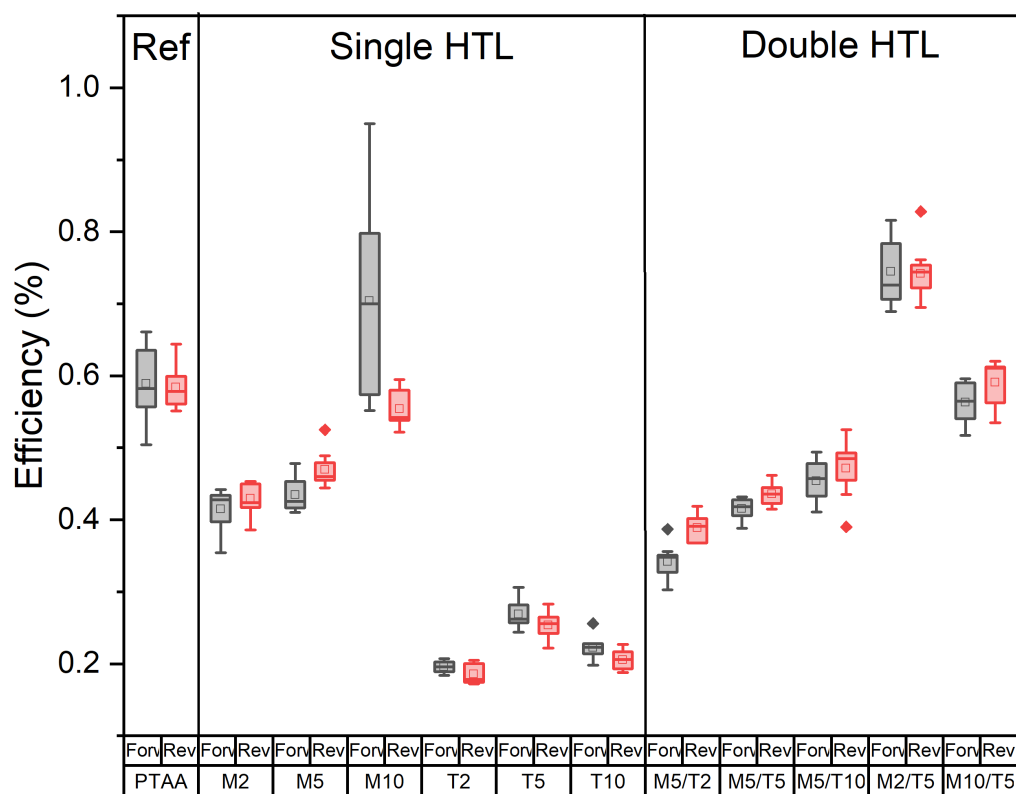


Figure E.4: Efficiency of all devices from the thickness optimization.

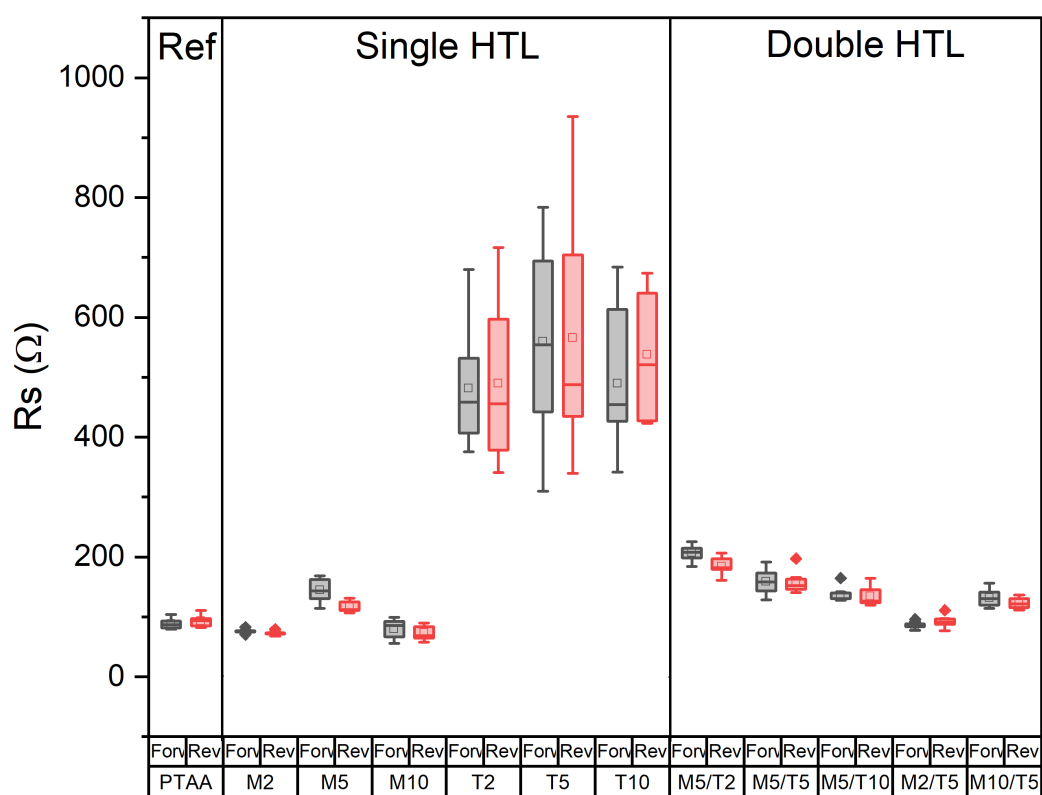
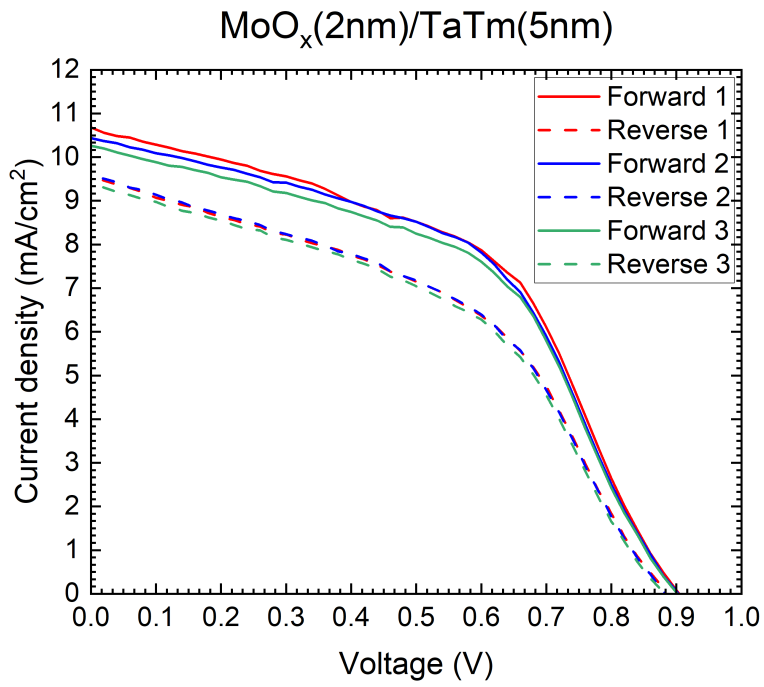


Figure E.5: Series resistance of all devices from the thickness optimization.

# F

## Final device



**Figure F.1:** J-V curves of forward and reverse scans of the optimized device with 2-nm thick MoO<sub>x</sub> and 5-nm thick TaTm.

**Table F.1:** Device parameters for forward and reverse scans of the optimized device with 2-nm thick MoO<sub>x</sub> and 5-nm thick TaTm.

Parameters	Scan 1		Scan 2		Scan 3	
	Forward	Reverse	Forward	Reverse	Forward	Reverse
$V_{oc}$	0.9043	0.8877	0.9023	0.885	0.9011	0.882
$J_{sc}$	10.622	9.655	10.436	9.684	10.233	9.473
FF	49.18	44.61	49.86	44.71	49.4	44.91
PCE	4.725	3.823	4.695	3.832	4.555	3.753